Methodological developement for retrieving land surface temperature from hyperspectral thermal infrared data

Xinke Zhong

UNIVERSITÉ DE STRASBOURG

ÉCOLE DOCTORALE MATHMATIQUES SCIENCES DE L'INFORMATION ET DE L'INGENIEUR

[Uds – INSA - ENGEES]

THÈSE

présentée par :

XinKe ZHONG

soutenue le : 22 Juin 2017

pour obtenir le grade de : **Docteur de l'Université de Strasbourg**

Discipline/ Spécialité : Electronique / Télédétection

Methodological developement for retrieving land surface temperature from hyperspectral thermal infrared data

THÈSE dirigée par :

M. Z-L. LI	Directeur de Recherche de CNRS, France

RAPPORTEURS :

M. J. SOBRINO	Professeur, Université de Valencia, Espagne
M. B-H. TANG	Directeur de Recherche de IGSNRR, Chine

AUTRES MEMBRES DU JURY :

Mme F. NERRY	Directeur de Recherche de CNRS, France

Acknowledgements

My deep appreciation goes to my supervisor Dr. Zhaoliang Li. I thank him for teaching me how to do research in the field of remote sensing and discussing problems about this dissertation study with me. Without his constructive criticism and praise, it is impossible to ensure the academic quality of this dissertation.

My sincere gratitude goes to the teachers Dr. Bohui Tang, Dr. Hua Wu and Dr. Ronglin Tang. Their altitude on research shows me how to do research work.

I thank the reviewers of this dissertation, Professor José A. Sobrino, Dr. Françoise Nerry, Dr. Jélila Labed, for their helpful advice to polish the dissertation.

I am grateful to current and past memebers of Télédétection Radiométrie et Imagerie Optique, for their helpful discussion with me. I thank Dr. Jérôme Colin, Dr Laure Roupioz, Dr. Chao Ren, Dr. Yidong Wang, Dr. Xiwei Fan, Dr. Pei Leng, Dr. Yuan Liu, Dr. Hongyuan Huo, Dr. Zhuoya Ni for their help to me in this dissertation study.

I appreciate everyone who helped me in this dissertation study.

This dissertation is dedicated to my family.

Résumé

La température de surface terrestre (LST, Land Surface Temperature) est un paramètre important dans les systèmes climatiques. La LST est appliquée à divers domaines thématiques tels que l'étude du bilan énergétique de la surface terrestre, l'estimation d'humidité du sol/évaporation, la surveillance de la végétation, la modélisation de la circulation atmosphérique du globe. La LST est également utilisée comme paramètre d'entrée pour estimer d'autres paramètres atmosphériques. Il est important d'obtenir une distribution temporelle et spatiale de LST à l'échelle locale et globale.

L'obtention de la LST à partir de mesure terrain est une tâche ardue et chronophage et cette technique n'est donc pas un moyen efficace pour des zones étendues. La télédétection dans l'infrarouge thermique (TIR, Thermal InfraRed) est par contre est un moyen rapide et économique d'obtenir la LST aux grandes échelles spatiales. Les méthodes basées sur la télédétection d'obtention de la LST dans l'TIR ne fournissent qu'une valeur de température par pixel. Ces produits LST sont inévitablement des combinaisons de zones mixtes même si la résolution est de l'ordre de quelques mètres. Il est donc nécessaire de développer des méthodes pour déterminer les températures sous-pixel.

La thèse consiste en huit chapitres décrits ci-dessous.

Le chapitre 1 introduit les notions nécessaires pour développer les méthodes de restitution de la LST et de démixage de la température (TUM : Temperature Un Mixing) et les objectifs du travail de thèse.

Différentes méthodes d'obtention de la LST sont développées pour les données TIR multispectrales : par exemple, la méthode monocanal, la méthode multicanaux, la méthode multi-angle, la méthode de separation de Température and émissivité (TES), la méthode jour/nuit basée sur la physique, la méthode de restitution de LST en deux étapes. Ces méthodes ont leurs avantages et inconvénients. Mais encore, le choix d'une méthode d'estimation de la LST est dependant des caractéristiques du capteur. Ces méthodes d'estimation de la LST multi-spectales ne peuvent pas être directment appliquées aux données TIR hyperspectrales avec des milliers de canaux. Pour estimer la LST à partir des données TIR hyperspectrales, la méthode de restituton des LST et émissivité des surface terrestre (LSE, Land Surface Emissivity) par étape et la méthode de restitution des LST et LSE simultanée

nécessitent la exacte connaissance du profil atmospherique. La méthode Empirical Orthogonal Function (EOF) basé sur une regression linéaire et la méthode Artificiel Neural Net (ANN) ne nécessitent pas de profil atmospherique, mais elles nécessitent des millers de canaux. La méthode de restitution des profils atmospheriques, LST et LSE simultanée ne pas nécessite aucune autre information atmospherique, mais elle est complexe à appliquer. Ces méthodes ne peuvent pas être utilisées pour l'obtention en temps quasi réel de LST à partir de données TIR hyperspectrales contenant des données endommagées. Il donc est nécessaire de développer une méthode pour ce type de données.

Diverses méthodes TUM pour du image de moyenne ou basse resolution spatiale sont développées : par exemple, la méthode multi-spectrale, la méthode multi-angle, la méthode multi-pixel et multi-résolution, la méthode multi-temporelle. Ces méthode TUM necessitent que les émissivités des composantes sont connues, et ne peut pas être appliquée aux données TIR de haute résolution spatiale. Pour estimer les temperatures des composantes, la méthode de démixage spectrale et mixage thermique estime la LST à partir des données Landsat ETM+ visible et TIR. Avec une haute résolution spatiale, cette méthode récupère les températures des sous-pixels et n'est pas applicable pour estimer températures des sous-pixels à partir des données TIR hyperspectral aéroportés haute résolution spatiale. La méthode TRUST est developpée sur la base de la physique, mais elle nécessite que la varation des températures des sous-pixels soit petite. Nous visons à développer une méthode de récupération des LST des sous-pixels pour ce type de surface en utilisant une résolution spatiale élevée et des données TIR hyperspectrales qui contiennent de larges informations de la composition des pixels mixtes.

Le chapitre 2 décrit les bases fondamentales de la radiation thermique. De façon plus spécifique, les théories de la radiation thermique, de l'émission et de la diffusion sont exposées. De plus les équations de transfert radiatif sont posées et le modèle linéaire/non-linéaire de mixage est décrit.

Les équations de transfert radiatif dans la intervalle spectrale de TIR est:

$$R_s(\theta_v, \varphi_v, \lambda) = R_g(\theta_v, \varphi_v, \lambda)\tau(\theta_v, \lambda) + R_{at\uparrow}(\theta_v, \lambda) + R_{s\uparrow}(\theta_v, \lambda)$$

La radiance spectrale measurée sur la surface de la terre, s'écrite:

$$R_g(\theta_v, \lambda) = \varepsilon(\theta_v, \lambda)B(T_s, \lambda) + [1 - \varepsilon(\theta_v, \lambda)](R_{at\downarrow}(\lambda) + R_{s\downarrow}(\lambda))\rho_b(\theta_s, \theta_v, \varphi_s, \varphi_v, \lambda)E_{sun}(\theta_s, \lambda)$$

où $\varepsilon(\theta_v, \lambda)$ est l'émissivité spectrale de la surface, $\rho_b(\theta_s,\theta_v,\varphi_s,\varphi_v,\lambda)$ est la réflectivité spectrale

bi-directionnelle, Ts est la LST, $\tau(\theta_v,\lambda)$ est la transmission totale de la atmosphere, $R_{at\downarrow}(\lambda)$ est la radiance atmosphérique descendante, $R_{at\uparrow}(\theta_v,\lambda)$ est la radiance atmosphérique directe, $R_s\uparrow(\theta_v,\lambda)$ est la radiance provenent de la diffusion atmosphérique de la contribution solaire, $R_s\downarrow$ est la radiance descendant provenent de la diffusion atmosphrique de la contribution solaire, $E_{sun}(\theta_s,\lambda)$ est la radiance solaire directe au niveau du sol, θ_v est l'angle zénithal, φ_s est l'angle d'azimutal solaire.

Le modèle linéaire de mélange utilisé dans ce travail de thèse s'ecrit :

$$R_g(\theta_v,\lambda,x,y)=\sum_{j=1}^{N}(\varepsilon_{\lambda,j}(\theta_v)B(T_{s,j},\lambda,x,y)+(1-\varepsilon_{\lambda,j}(\theta_v))R_{at\downarrow}(\lambda))S_j(x,y)$$

où $R_g(\theta_v,\lambda,x,y)$ est la radiance spectral de pixel mixte mesurée au dessous de l'atmosphére, $\varepsilon_{\lambda,j}(\theta_v)$ est l'émissivité spectrale de la composante pure j dans le pixel mixte, $T_{s,j}$ est la température de la composante j dans le pixel mixte, $S_j(x,y)$ est l'abondance de la composante j dans le pixel mixte, N est le nombre de composante dans le pixel mixte.

Le chapitre 3 détaille les méthodes d'estimation de la LST et de démixage de la température (TUM) à partir des donnés TIR. Les méthodes d'estimation de la LST à partir des données TIR multi-spectrales, les méthodes d'estimation de la LST à partir des données TIR hyperspectrales, les méthodes TUM pour des données TIR basse/moyenne résolution spatiale, et les méthodes TUM pour les données TIR haute résolution spatiale sont présentées.

Les inconvénients principaux des méthodes d'estimation de la LST à partir des données TIR hyperspectrales:

(1) La difficulté de correction atmospherique. La majeure partie des méthodes de correction atmospherique est dévelopée pour les données TIR hyperspectrales aéroportés. Les méthodes de correction atmospherique pour les données satellitaires TIR necessitent les autres données atmospheriques qui sont difficiles à obtenir.

(2) La difficulté de restitution des LST, LSE et profil atmospherique simultanément. Les methods associées sont complexes et necessitent le recours à les modèles atmospheriques rapides, donc ces méthodes sont difficiles à appliquer. C'est nécessaire que on développe le modèle atmospherique rapide . Par ailleurs, la performance de ces méthodes n'est pas stable à cause de leur nature complexe.

Les inconvenients principaux des méthodes d'estimation des LSTs des sous-pixels à partir des données TIR hyperspectrales avec haute résolution spatiale incluent:

(1) La difficulté de démixage de la LST pour les surfaces hétérogènes avec une grande variation des températures. Le méthode TUM basée sur la physique pour estimer la LSTs des sous-pixels à partir des données TIR haute résolution spatiale necessitent que la variation des LSTs soit petite, ce qui n'est pas toujours vrai pour les surfaces hétérogènes.

(2) La difficulté de démixage de la LST pour les surfaces regueuse. Les majorité des méthodes TUM de restitution de la LST à partir des données TIR haute résolution spatiale ne considérent pas les factors non-linéaires: la conductance et l'advection horizontale. La rugosité des surfaces urbaines n'est pas négligeable dans l'image TIR avec haute résolution spatiale.

Le chapitre 4 décrit les données, les zones d'intérêt, et le modèle atmospherique.

Les données de sondage atmosphérique utilisées dans cette thèse sont les données de profil atmosphérique NOAA / ESRL. Les bases de données utilisées comprennent la base de données TIGR, les bases de données d'émissivité ASTER et MODIS USCB et les données d'émissivité urbaine de la littérature (Cubero-Castan, 2015). Les données satellitaires utilisées dans ce travail incluent les données METOP-A IASI, le produit LST de Metop-A IASI, le produit LST de Metop-A AVHRR et le produit MOD11B LSE.

La zone d'intérêt de la Mer Mediterranée couvrant la longitude de 12° E a 32° E et la latitude de 30° N à 43° N est utilisée pour cartographier la LST des surfaces à haute émissivité en utilisant des méthodes pour les données TIR hyperspectrales contenant des données endommagées. La zone d'interet de l'Australie couvrant la longtitude de 112° E a 152° E et la latitude de 43° S a 0° N est utilisée pour cartographier la LST des surfaces naturelles en utilisant la méthode d'estimation de la LST développée.

Enfin, le modèle de transfert radatif atmospherique 4A / OP est présenté dans ce chapitre.

Le chapitre 5 présente le développement d'une méthode multicanaux pour les surfaces présentant une haute émissivité. En se basant sur la méthode SW (Split Window), nous avons proposé une méthode multicanaux pour extraire la LST utilisant une équation de régression linéaire qui relie la LST à plus de deux températures de brillance TIR TOA (Top Of Atmosphere). Pour déterminer les nombres d'onde centraux des canaux i et les coefficients, nous simulons d'abord une grande quantité de données IASI en utilisant le modèle de transfert radiatif atmosphérique 4A / OP et l'équation de transfert radiatif dans un intervalle spectral de 645-2760 cm-1 et une résolution spectrale de 0,25 cm-1. Diverses conditions atmosphériques

et conditions de surface peuvent être utilisées par 4A / OP pour la simulation. Les sorties atmosphériques de 4A / OP et le spectre LSE du corps noir sont introduits dans l'équation de transfert radiatif pour calculer la température de brillance spectrale. Après la simulation des données, nous avons analysé la relation entre les coefficients w_i et la teneur en vapeur d'eau à l'aide des données de simulation et avons déterminé les nombres d'ondes centraux pour chaque canal i ainsi que les coefficients en utilisant la technique de régression par étapes avec des données de simulation. La précision de la méthode multicanaux est évaluée en utilisant des données de simulation et des données de satellite au nadir. De plus, la sensitivité de la méthode multicanaux développée à la résolution spectrale et au bruit instrumental est étudiée avec les données de simulation.

Les conclusions que nous en tirons dans ce chapitre sont:

(1) LST de surfaces presentant une haute émissivité peut être obtenue exactement à partir des données de simulation avec un RMSE de 0,2 K par la méthode multicanaux développée en utilisant seulement 10 canaux.

(2) Les coefficients w_i de la méthode développée dépendent de la résolution spectrale. Mais LST des surfaces présentant une haute émissivité peut toujours être obtenue précisément quand les coefficients sont déterminés pour chaque résolution spectrale.

(3) L'influence du bruit instrumental n'est pas significatif : L'influence du bruit instrumental est l'ordre du bruit.

(4) La comparaison de la LST extraite des données Metop-A IASI avec le produit LST de Metop-A AVHRR montre que le RMSE de la LST extraite est de 0,4 K. La LST de surfaces presentant une haute émissivité peut etre obtenue précisément à partir des données satellite par la méthode développée.

Le chapitre 6 décrit l'extension de la méthode multicanaux conçue pour les surfaces à haute émissivité pour les surfaces naturelles. La méthode multicanaux, mentionnée au chapitre 5, suppose l'hypothèse que l'émissivité est égale à l'unité, ce qui rend la méthode non directement applicable pour les surfaces naturelles. En s'inspirant de la méthode SW et en supposant que le spectre LSE dans le domaine spectral de 815 cm^{-1} - 960 cm^{-1} peut être exprimé comme une fonction linéaire de LSEs de deux canaux, nous avons extrait la LST pour les surfaces terrestres naturelles en utilisant une fonction linéaire de plus de 2 températures de brillance et en reliant les coefficients ω_i de cette équation de régression linéaire à la combinaison des deux LSEs et la teneur en vapeur de eau. La base de données de

simulation est créée à l'aide de 4A / OP avec des données typiques de profil atmosphérique provenant de la base de données TIGR et des données LSE typiques de la base d'émissivité ASTER. Pour déterminer les canaux et les coefficients dans cette méthode multicanaux étendue, nous sélectionnons tout d'abord des paires de canaux initiaux qui représentent les caractéristiques principales du spectre de la température de brillance à l'aide de données de simulation. Après cela, nous avons déterminé n paires de canaux les plus importants et les coefficients ω_i à partir des couples de canaux initiaux sélectionnés par la méthode de régression par étapes. Le critère de détermination de nombre des canaux est ce que la erreur de LST obtenue par les données de simulation est inférieure à 0,5 K. La relation entre les coefficients ω_i et la teneur en vapeur d'eau et LSE a été analysée à l'aide de données de simulation. La précision de la méthode multi-canale étendue est évaluée en utilisant des données de simulation et des données de satellite. La sensitivité de cette méthode multicanaux étendue à le bruit instrumental et à la erreur de la teneur en vapeur d'eau est étudiée avec les données de simulation.

Nous en tirons les conclusions suivantes:

(1) Les coefficients ω_i sont liés à la teneur en vapeur d'eau et au contraste spectral du spectre LSE et de la LSE moyenne. Quand la condition de LSE est connue et la erreur de la teneur en vapeur d'eau est 10%, LST peut être obtenue exactement à partir des données de simulation avec un RMSE de 0,6 K en utilisant des measures TIR hyperspectales à 10 canaux.

(2) Si la valeur moyenne de deux LSEs est < 0,95, l'erreur de la LST obtenue par la méthode multi-canaux étendue à partir des données de simulation passe de 0,5 K à 0,8 K.

(3) L'influence du bruit intrumental sur la méthode multicanaux étendue est le double de la grandeur du bruit.

(4) Avec le produit LSE de MODIS en tant qu'entrée et une erreur de 10% sur la teneur en vapeur d'eau, la différence entre la LST obtenue par Metop-A IASI et le produit LST de Metop-A / IASI est d'environ 2 K.

Le chapitre 7 montre le développement d'une méthode TUM améliorée basée sur la physique. La méthode d'obtention de la LST extrait une seule LST à partir de données TIR sur un pixel. Nous avons développé une méthode basée sur la physique pour obtenir des températures des sous-pixels sur des surfaces hétérogènes présentant de grandes variations de température. Supposant que chaque type de surface a des pixels purs dans l'image TIR, la méthode TUM proposée a été développée pour récupérer simultanément les températures des sous-pixels,

l'abondances des composantes à partir d'images TIR à résolution spatiale élevée par résolution non linéaire des équations de transfert radiatif pour améliorer la précision des résultats et en utilisant une nouvelle fonction de coût et de nouvelles valeurs de première estimation pour stabiliser la solution des équations de transfert radiatif avec des termes atmosphériques connus. Plus précisément, les températures de sous-pixels peuvent être obtenues en trois étapes: les LSE et les LST des pixels purs sont extraits en utilisant la méthode TES et en utilisant des images visibles pour localiser les pixels purs. Deuxièmement, les premières valeurs initiales sont obtenues par la méthode TRUST. Troisièmement, avec la LSE des pixels purs et les paramètres initiaux des composantes et les termes radiatifs atmosphériques connus, les températures des sous-pixels et les abondances de composantes sur des pixels mélangés sont obtenus par la méthode TUM proposée. La fonction de coût dans la méthode TUM proposée est une combinaison de la fonction de coût utilisée dans la méthode TRUST et d'une fonction de coût basée sur une solution non linéaire. La précision de la méthode proposée est evaluée à l'aide de données de simulation. La sensitivité de cette méthode à la différence entre les émissivités des composantes, à la différence entre les températures de sous-pixels, et à la variation des températures des sous-pixels est étudiée avec les données urbaines de simulation.

Les conclusions dans ce chapitre sont:

(1) Si la variation de la température de chaque composante est 6 K, les températures des composantes peuvent être obtenues par la méthode TUM proposée à partir des données TIR hyperspectrales de simulation avec un RMSE de 3 K. Les temperatures des composantes obtenues sont plus précises que elles obtenues par la méthode TRUST.

(2) Si la variation de chaque température de composante change de 3 K à 9 K, le RMSE des températures des composantes obtenue par la méthode proposée passe de 1,7 K à 3,5 K. La méthode proposée n'est pas très sensible à la varation de température de composante.

(3) Si la différence entre les températures des composantes descend de 15 K à 5 K et la variation de température de composante est 3 K, le RMSE des températures des composantes obtenues par la méthode proposée augment de 1,9 K à 2.1 K. La méthode proposée n'est pas sensible à la différence entre les températures des composantes.

(4) Si la différence entre les émissivités des composantes change de 0,07 à 0,035 , le RMSE des températures des composantes obtenues par la méthode proposée passe de 3,5 K à 5,7 K. La méthode proposée est aussie sensible à la différence entre les émissivités des composants.

Le chapitre 8 expose les conclusions et les perspectives.

Dans cette thèse, nous avons tout d'abord développé une méthode multicanaux pour obtenir les LST à partir de données hyperspectrales, étudié sa sensibilité et évalué sa précision en utilisant des données simulées et des données de télédétection. Ensuite nous avons développé une méthode TUM améliorée fondée sur la physique pour la haute résolution spatiale et les données hyperspectrales et avons réalisé l'analyse de sensibilité et d'erreur en utilisant des données de simulation.

Finalement, les perspectives de ce travail sont :

(1) La méthode multicanaux proposée pour les surfaces naturelles nécessite la connaisse de la LSE et la teneur en vapeur d'eau qui sont difficiles à obtenir. Il nécessaire de développer une nouvelle methode pour correction atmospherique des données TIR hyperspectrales.

(2) La méthode multicanaux proposée est conçue pour les données TIR hyperspectrales au nadir dans cette étude. Nous étendions la méthode multicanaux pour les mesures hors-nadir dans le futur.

(3) La méthode TUM proposée n'est pas évaluée en utilisant des données de satellite. Nous évaluerons la méthode TUM proposée avec les données de satellite et développerons une nouvelle méthode TUM pour stabiliser la résolution du modèle linéaire/non-linéaire de mélange.

(4) La méthode TUM proposée n'est pas évaluée sur les pixels mixtes contenant plus que deux composantes. Nous évaluerons la performance de cette méthode sur les pixels mixtes composés de trois composantes dans le futur.

Contents

List of Figures

List of Tables

List of acronyms

AIRS	the Atmospheric InfraRed Sounder
ANN	Artificial Neural Network
AVHRR	the Advanced Very High Resolution Radiometer
BOA	Bottom Of Atmosphere
CrIS	the Cross-Track Infrared Sounder
D/N	Day/Night
DA	Diurnal Amplitude
DUCAS	the Detection in Urban scenario using Combined Airborne imaging Sensors
EFOV	Effective Field Of View
EOF	Empirical Orthogonal Function
EOS	the Earth Observing System
ESRL	the Earth System Research Laboratory
FWHM	Full Width at Half Maximum
GEOS	the Geostationary Operational Environmental Satellite
HyspIRI	the Hyperspectral Infrared Imager
IASI	the Infrared Atmospheric Sounding Interferometer
IFOV	Instantaneous Field Of View
IRS	the Infrared Sounder
ISRF	Instrumental Spectral Response Function
ISSTES	Iterative Spectrally Smooth Temperature and Emissivity Separation
JHU	the Johns Hopkins University
JPL	the Jet Propulsion Laboratory
LECTES	Linear Emissivity Constraint Temperature and Emissivity Separation
LSE	Land Surface Emissivity
LST	Land Surface Temperature
MIR	Mid-InfraRed
MND	the Maximum miNimum apparent emissivity Difference
MODIS	the Moderate Resolution Imaging Spectroradiometer
NEM	Normalization Emissivity Method
NEΔT	Noise Equivalent Differential Temperature
PCA	Principal Component Analysis
PVC	Percentage of Vegetation Cover
RMSE	Root Mean Square Error
SAF	the Satellite Application Facilities
SEBASS	the Spatially Enhanced Broadband Array Spectrograph System

SEVIRI	the Spinning Enhanced Visible and InfraRed Imager
SR	the Spectral Ratio
SST	Sea Surface Temperature
SUTM	Spectral Unmixing and Thermal Mixing
SW	Split-Window
TES	Temperature and Emissivity Separation
TIGR	the Thermodynamic Initial Guess Retrieval
TIR	Thermal InfraRed
TOA	Top Of Atmosphere
TRSM	the Two Step Retrieval Method
TRUST	the Thermal Infrared Unmixing method for retrieving Subpixel Temperatures
TTM	the Two Temperature Method
TUM	Temperature UnMixing
UCSB	the University of California, Santa Barbara
USGS	the United States Geological Survey
VZA	Viewing Zenith Angle
WV	Water Vapor content column

List of physic parameters

$\Delta\Omega_i$	the solid angle on which the facet i is seen by sensor
$\Delta\Omega_{j\rightarrow i}$	the solid angle on which facet j is seen by facet i
Ω	solid angle
Ω_s	instantaneous field of view of the sensor
α	absorptivity
ε	emissivity
ε_{815}	the LSE value at the channel centered at 815 cm^{-1};
ε_{950}	the LSE value at the channel centered at 950 cm^{-1}
ε_a	the mean value of two channel LSEs centered at 815 cm^{-1} and 950 cm^{-1}
ε_{i1}	the LSE measured in the MIR channel
$\varepsilon_{\lambda,j}$	the emissivity of the pure component j in the mixed pixel
θ_i	incident zenith angle
θ_s	solar zenith angle
θ_v	viewing zenith angle
λ	wavelength
ν	wavenumber
ρ	reflectivity
ρ_b	directional hemispherical reflectance
ρ_m	density of the medium
τ	transmissivity
τ	atmospheric transmittance
τ'	monochromatic optical thickness of the medium
φ_i	incident azimuth angle
φ_s	downwelling atmospheric spectral radiance
φ_v	viewing azimuth angle
B(x)	the Planck's function
c	the speed of light
E	irradiance
E_{sun}	the direct solar spectral irradiance at the ground
f_i	spectral response function of the channel
h	the Planck constant
H	relative humidity
I	radiant intensity
I_λ	spectral radiant intensity
j_λ	the source function coefficient
J_λ	source function
k	the Bolzmann constant
k_λ	mass extinction coefficient
M	radiant exitance

m_{air}	average molecular weight of the air
N	the number of components composing the mixed pixel (x,y)
n_0	the Loschmidt coefficient
N_A	the Avogadro coefficient
p_s	the pressure measured at the land surface
R	radiance
r	the mixing ratio of atmospheric water vapor
$R_{at\uparrow}$	upwelling atmospheric radiance
R_{emis}	the radiance emitted by components in the pixel
R_g	the at-ground spectral radiance
R_i	the at-sensor channel-averaged radiance
R_s	the radiance reaching the sensor
$R_{s\uparrow}$	upwelling atmospheric spectral diffusion radiance
$R_{s\downarrow}$	the downwelling hemispheric atmospheric spectral diffusion radiance resulting from the scattering of solar radiance divided by Π
R_λ	spectral radiance
R_{emis}^{neig}	the radiance of component j reflected by component i
$R_{atm,\downarrow}$	the downwelling atmospheric radiance reflected by each component
R_{emis}^{neig}	the downwelling atmospheric radiance reflected by the neighborhood component
s	the depth of the medium
$S_{f,i}$	the initial component abundance i composing the mixed pixel
S_j	the abundance of the component j in the mixed pixel
$S_{ret,i,j}$	the retrieved abundance of component i in mixed pixelj
$S_{true,i,j}$	the true abundance of component i in mixed pixel j
$\vec{S}$	the vector of component abundances in the mixed pixel
T	radiant temperature
T_b	brightness temperature
T_d	dew point temperature
T_g	the brightness temperature at ground level at channeli
T_i	the brightness temperature at TOA at channel i
T_{i1}	the brightness temperature at TOA in the MIR channel
T_n , T_f	the at-sensor brightness temperatures measured in the nadir and forward views
T_p	the atmospheric temperature at pressure layer p
$T_{ret,i,j}$	the retrieved temperature of component i in mixed pixel j

T_s	land surface temperature
$T_{s,f,i}$	the initial component temperature i
$T_{s,j}$	the LST of the component j in the mixed pixel
$T_{st,i}$	the brightness temperature at TOA at a strong-absorption channel i
$T_{true,i,j}$	the true temperature of component i in mixed pixel j
$T_{we,i}$	the brightness temperature at TOA at a weak-absorption channel near the strong-absorption channel i
$\vec{T}$	atmospheric temperature profile
$\overrightarrow{T_s}$	the vector of component temperatures in the mixed pixel

1 Introduction

1.1 Background

Land surface temperature (LST) is a key parameter in climate systems. LST is used for various thematic applications, such as earth surface energy budget studies (Zhou et al. 2003), numerical weather/climate forecasting (Le Marshall et al. 2006), climate variability analysis, global sea circulation study (Valor and Caselles 1996), and soil moisture/evapotranspiration estimations (Rhee et al. 2010).

LST is defined as the radiant temperature calculated from the thermal radiation emitted by the observed surface. Because the thermal radiation acquired by a radiometry is in reality emitted by a thin layer of surface, radiant temperature is also called the skin temperature.

Ground measurements cannot practically provide LST values over vast region. Thermal infrared (TIR) remote sensing has become an effective method to measure LST on large spatial scales (Dash et al. 2002; Li et al. 2013). In remote sensing-based way, space-borne sensors measure the surface emitted radiance modified by the atmosphere in different spectral channels; brightness temperatures are calculated from the radiance by reversing Planck's function. Various methods are used to retrieve LST from the brightness temperatures with auxiliary data. The merits of remote sensing in measure of LST include: requirement of less human labour and material resources; its feasibility of measure of LST in large spatial scale; its efficiency in producing LST data.

Atmospheric correction is one critical process for retrieving LST from spaceborne radiometry. Surface emitted thermal radiation reaching spaceborne sensor is affected by atmospheric absorption attenuation and a deduction caused by the atmospheric emission. The aerosol scattering and absorption in 8 -12 μm is negligible and generally ignored. The atmospheric absorption gases in thermal infrared region include trace gases such as CO_2, O_3, CO, CH_4, and water vapor. The volume of trace gases in the atmosphere is nearly invariant spatially and temporally. Unlike the trace gases, water vapor varies on short spatial-scales and on short time-scales, which make it important to correct of atmospheric effects.

Temperature and emissivity separation is another critical process for retrieving LST from spaceborne radiometry. Because surface emission in a channel is a function of LST and LSE, LST is one of the coupling physic parameters in radiance measured by spaceborne sensor. LSE varies dramatically over continental surfaces due to the change of surface characteristics

such as vegetation fraction, soil moisture, surface type and surface roughness.

Various methods can be used to retrieve LST from satellite-based multispectral TIR data: the single-channel method (Hook et al. 1992), the split-window (SW) method (McMillin 1975) and the multi-channel method (Sun and Pinker 2003; Sun and Pinker 2005, 2007), the multi-angle method (Chedin et al. 1982), the physical-based day/night operational method (Wan and Li 1997), the Temperature and Emissivity Separation (TES) method (Gillespie et al. 1998), the multi-temporal physical method (Li et al. 2011), the Kalman filter physical method (Masiello and Serio 2013) and the Two Step Retrieval Method (TSRM) (Ma et al. 2000; Ma et al. 2002). The single-channel method requires good knowledge of LSE at the channel used and an accurate atmospheric profile. This is difficult or even impossible to satisfy in most practical situations. The SW method utilizes differential atmospheric absorption in two adjacent channels centred at 11 μm and 12 μm, which does not require information about the atmospheric profile for ocean applications at the time of the acquisition (McMillin 1975). However, the SW method requires accurate atmospheric water vapour content and LSE for land applications (Li et al. 2013). The multi-channel method uses characteristics of the mid-infrared (MIR 3-6 μm) channel i_1 at 3.9 μm and channel i_2 centred at 8.7 μm to improve atmospheric correction at night, which does not require atmospheric water vapour content (Sun and Pinker 2003; Sun and Pinker 2007). However, the multi-channel method cannot be utilized in applications at daytime. Similar to the principle of the SW method, the multi-angle method is based on the differential water vapour absorption measured by sensor from different angles. The multi-angle method suffers from the phenomenon of LSE angular dependence and LST angular dependence (Sobrino and Jiménez-Muñoz 2005). The four methods mentioned above require good knowledge of LSE, which is difficult to obtain. Therefore, the following methods have been developed to retrieve LST and LSE simultaneously. The physical-based day/night operational method utilizes two-time measurements at 7 MIR and TIR channels to constrain the ill-posed temperature/emissivity separation with known atmospheric corrections (Ma et al. 2002). However, the physical-based day/night operational method suffers from problems of geometry mis-registration, variations in the viewing zenith angle and inaccurate atmospheric correction (Wan and Li 2008). The TES method relies on an empirical relationship between spectral contrast and minimum emissivity to separate LST and LSE from five atmospherically corrected Advanced Spaceborne Thermal Emission Radiometer (ASTER) TIR data (Gillespie et al. 1998). However, the TES method exhibits significant errors under hot and wet atmospheric conditions (Gillespie et al. 2011). The multi-temporal physical method (Li et al. 2011) and the Kalman filter physical method (Masiello et al. 2013) utilize the invariance feature of LSEs measured within a short time period (six hours) to separate LST and LSE from geostationary thermal infrared radiances provided that good atmospheric correction has been perform. The

TRSM method simultaneously retrieves the atmospheric profiles, LST and LSE from the Moderate Resolution Imaging Spectroradiometer (MODIS) channel data, which does not require atmospheric correction or knowledge of LSE (Ma et al. 2002). However, the requirement of adequate channels and the TRSM method's complex nature make it difficult to apply.

The LST retrieval methods mentioned above use satellite data measured at several broad channels such as the Advanced Very High Resolution Radiometer (AVHRR) TIR data (band width: 1 μm), MODIS TIR data (0.5 μm), ASTER TIR data (band width: 0.4 to 0.7 μm). However, hyperspectral TIR sensors, namely, TIR sensors with many narrow and contiguous channels, have much higher spectral resolution and provide opportunity to develop new methods for retrieving LST. For example, the Spatially Enhanced Broadband Array Spectrograph System (SEBASS) has 128 TIR channels (spectral resolution: ~4 cm^{-1} at 10 μm), the Atmospheric InfraRed Sounder (AIRS) has 2738 TIR channels (resolution: 0.55 cm^{-1}). The hyperspectral TIR data with thousands of channels provide plenty of information on the atmosphere and land surface.

Meanwhile, various spaceborne hyperspectral TIR sensors exist to provide this type of data. The first successful sensor, AIRS (Susskind et al. 2003), has been providing hyperspectral TIR data since 2002. There are hyperspectral TIR data observed by other space-borne sensors, such as the Infrared Atmospheric Sounding Interferometer (IASI) (Chalon et al. 2001; Simeoni et al. 2004) and the Cross-track Infrared Sounder (CrIS) (Bloom 2001). In the future, the infrared sounder[1] (IRS) will also provide this type of hyperspectral TIR data. There is a pressing need for methodological development in order to retrieve LST from these space-borne hyperspectral TIR data.

Various methods exist to retrieve LST from space-borne hyperspectral TIR data: the linear regression method (Schlussel and Goldberg 2002; Zhou et al. 2002; Goldberg et al. 2003; Weisz et al. 2007; Zhou et al. 2011), the Artificial Neural Network (ANN) method (Aires et al. 2002a; Wang et al. 2013a), the stepwise LST and LSE retrieval method (Pequignot et al. 2008), the simultaneous LST and LSE retrieval method (Susskind et al. 2003; Paul et al. 2012), the physical simultaneous atmospheric profiles, LST and LSE retrieval method (Rodgers 1976; Li et al. 2007; Masiello and Serio 2013). The ANN method and linear regression method are based on a linear/nonlinear empirical relationship between principal component amplitudes of brightness temperature spectrum at Top Of Atmosphere (TOA) and LST or LSE. The linear regression method and the ANN method do not require extra atmospheric data and are fast enough for near real-time application (Wang et al. 2013b).

[1] http://www.eumetsat.int/Home/Main/Satellites/MeteosatThirdGeneration/index.htm

However, the linear regression method and the ANN method require thousands of channels and have much error for complex physical situations (Paul et al. 2012). For example, aerosols hamper the application of the linear regression method and the ANN method. The stepwise LST and LSE retrieval method relies on the phenomenon that LSE is close to unity at a certain channel to separate LST and LSE with known atmospheric profile. The stepwise LST and LSE retrieval method requires accurate atmospheric profile and good knowledge of LSE at the used channel. The simultaneous LST and LSE retrieval method depends on an empirical relationship between principal components of LSE and each channel LSE to constraint iterative solution of LSE and LST with known atmospheric profile. The simultaneous LST and LSE retrieval method does not require good knowledge of LSE at a certain channel. However, the simultaneous LST and LSE retrieval method requires accurate atmospheric profile. The physical simultaneous atmospheric profile, LST and LSE retrieval method utilizes physical constraint based on spectral smoothness characteristic of LSE to iterative solve LST, LSE and atmospheric profile simultaneously with the support of atmospheric radiative transfer model. The physical simultaneous retrieval method does not require atmospheric profile or good knowledge of LSE, but it has low computation efficiency because of its complex nature. The hyperspectral TIR data contains damaged data due to the dysfunction of instrument or other damage in the data transfer. However, these methods cannot be used for hyperspectral TIR data containing damaged data at certain channels.

The LST retrieval methods mentioned above only retrieve a single LST for a pixel, it is not correct for heterogeneous surfaces. Although satellite launching missions such as Micro Satellite for Thermal Infrared Ground surface Imaging (Garcia-Moreno et al. 2009) (spatial resolution: 50 m; 1- or 2- day interval) and hyperspectral Infrared Imager (HyspIRI) (Chien et al. 2009) (spatial resolution: 60 m; 5-day interval) will provide data with higher spatial and temporal resolutions and airborne thermal sensors provide images with spatial resolution of several meters (Hecker et al. 2010), mixed pixels are inevitable in TIR data from these satellite sensors.

LSEs and abundances of subpixel materials, which is also called component emissivities and component abundances, are important for geological study such as mineral mapping because silicate materials in rocks and soils have various spectral shapes in emissivity (Vaughan et al. 2003). In the 8 μm to 12 μm atmospheric window, mineral groups such as silicates, carbonates, sulfates, and phosphates have spectral features related to the fundamental vibrational frequencies of their interatomic bonds. The features are known as reststrahlen bands and can be used to identify a mineral sample. Also, component emissivities and adundances are used for other applications such as urban environment study, surveillance (Schaepman et al. 2009).

LSTs of subpixel materials, which is also called the component temperatures, are widely used for various applications such as the estimation of evapotranspiration (Archer and Jones 2006), urban climate and environment analysis (Deng and Wu 2013). For instance, the merits of usage of component temperatures for urban thermal pattern analysis mainly include: convenient separation/identification of thermal behaviours of different urban surface materials, inherent integration with ecological models.

TIR radiance data is a function of the component abundances, of the component emissivities and of the component temperatures. TIR data is widely used to obtain spatially distributed component emissivity, component temperature and component abundances.

Various methods for simultaneously retrieving temperature and emissivity from TIR data exist in literature. However, these methods require the assumptions that a pixel is composed of only one material (Borel 1997; Wan and Li 1997; Gillespie et al. 1998) or that the pixel is composed of one or more material at the same temperature (Collins et al. 2001), while in reality many pixels are composed of various materials at different temperatures.

Various methods exist for retrieving component temperatures from coarse or medium spatial resolution TIR data: the multi-spectral temperature unmixing (TUM) method (Dozier 1981; Song and Zhao 2007), the multi-angular TUM method (Li et al. 1999; Jia et al. 2003; Timmermans et al. 2009), the multi-pixel and multi-resolution TUM method (Dozier 1981; Zhang et al. 2005; Zhang et al. 2008; Zhan et al. 2011a), and the multi-temporal TUM method (Zhang et al. 2003b). These methods are developed for low/medium spatial resolution TIR data and they are not suitable for high spatial resolution TIR data.

For high spatial resolution TIR data, the Spectral Unmixing and Thermal Mixing (SUTM) method estimates LST of high spatial resolution from Landsat ETM+ visible and TIR data by approximating the mixing of temperature as a linear mixing of component temperatures (Deng and Wu 2013). The SUTM method can only coarsely retrieve component temperatures and is not suitable for high spatial resolution TIR data with thousands of channels. The physics-based Thermal Infrared method for Unmixing Subpixel Temperature (TRUST) method simultaneously retrieving component temperatures and component abundances over mixed pixels by a minimization of reconstruction error of the mixed-pixel Bottom Of Atmosphere (BOA) radiance (Cubero-Castan et al. 2015). The TRUST method for physically unmixing component temperatures cannot be utilized for heterogeneous surfaces the large variation of component temperatures.

1.2 Objectives

In this dissertation a framework is described to achieve the following ultimate objectives:

developing a flexible method for retrieving LST from hyperspectral TIR data and developing an improved physics-based method for unmixing subpixel temperatures from high spatial resolution hyperspectral TIR data.

Specifically, the study will pay attention to the following.

A multi-channel method for retrieving LST from hyperspectral TIR data with assumption of LSE of unity is developed.

- A LSE-adjusted multi-channel method for retrieving LST from hyperspectral TIR data with known LSE condition and known water vapor content is developed. The method is developed in the following two steps.

  － reduction of the dimension of the LSE spectrum using a linear function

  － development of a multi-channel method for retrieving LST from hyperspectral TIR data with the proposed LSE linear function

- An improved physics-based method for unmixing subpixel temperatures from hyperspectral TIR data with consideration of larger variation of subpixel temperatures is developed.

1.3 Flowchart of the dissertation research and organization of the dissertation

1.3.1 Flowchart of the dissertation research

To achieve the objectives in Section 1.2, the research work was carried out according to the procedures shown in Figure 1.1. First, a large simulation database was created for IASI using atmospheric data and land surface data with simulation model the Operational release for Automatized Atmospheric Absorption Atlas (4A/OP). Second, a method for retrieving LST for high emissivity surfaces from hyperspectral TIR data was developed by using an empirical relationship between LST and a combination of IASI brightness temperatures with the simulation database. In this step, the sensitivity analysis and the validation of the developed multi-channel method were carried out using simulation data and satellite data. Third, the developed multi-channel method was extended to natural land surfaces by refitting the coefficients in the empirical relationship with consideration of LSEs of natural land surfaces, and the sensitivity analysis and the validation were carried out using simulation data and satellite data. Fourth, a new TUM method was developed by using an improved solution of the radiative transfer equations for component abundances and component temperatures

with known atmospheric condition, and the developed TUM method was evaluated using simulation data.

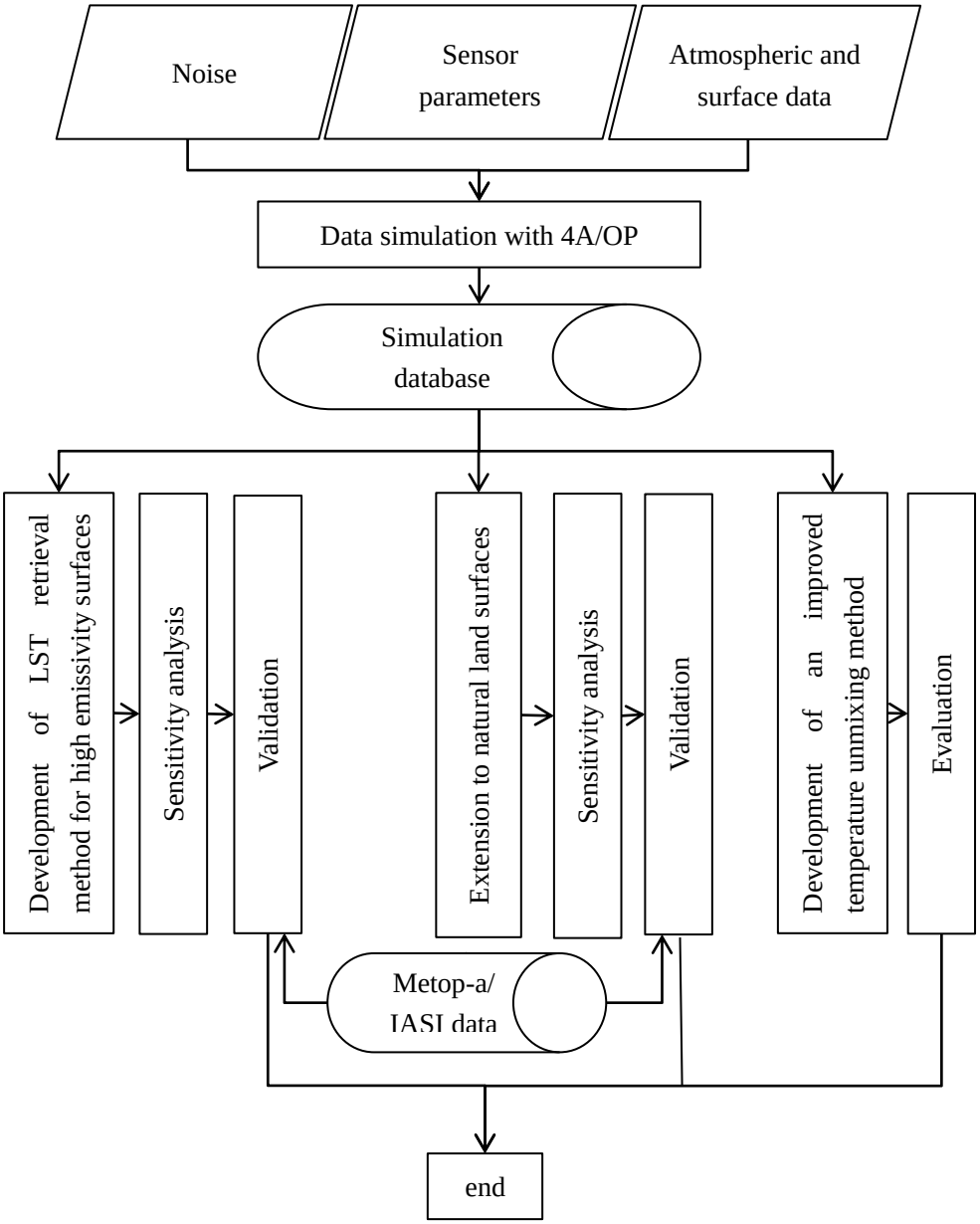

Figure 1.1 The flowchart of the dissertation research

1.3.2 Organization of the dissertation

The dissertation is composed of eight chapters.

In the first chapter, the importance of LST and component parameters is presented. The background of retrieval of LST from TIR data and the background of estimation of

component temperatures are illustrated.

The second chapter is devoted to basic theories for retrieving LST from hyperspectral TIR data, to basic theories for unmixing component temperatures from hyperspectral TIR data.

The third chapter is to present a review of methods for retrieving LST from the multispectral and hyperspectral TIR data and for retrieving component temperatures from TIR data.

The fourth chapter is to introduce satellite data and related data used for developing a flexible method for retrieving LST from hyperspectral TIR data and for developing an improved physics-based method for unmixing component temperatures from hyperspectral TIR data.

The fifth chapter is to develop a multi-channel method for retrieving LST for high emissivity surfaces from hyperspectral TIR data, to evaluate the developed method and analyze its sensitivities to spectral resolution, instrumental noise.

The sixth chapter is to develop a multi-channel method for retrieving LST for natural land surfaces from hyperspectral TIR data with known water vapor content and known LSE condition, to investigate its sensitivities to error of water vapor content, to variation of LSE and to instrumental noise.

The seventh chapter is to develop an improved physics-based method for unmixing component temperatures from hyperspectral TIR data, to evaluate the developed TUM method.

The conclusions of this study and prospects are presented in the eighth chapter.

2 Fundamental definitions and theories on the thermal radiation

2.1 Definitions

1) Wavelength

Wavelength, namely λ, is defined as the distance that an electromagnetic wave transfers in a vibrational period. This definition is not restricted to electromagnetic wave. The unit of wavelength for the infrared radiation usually is μm.

Wavenumber, namely ν, is another concept which is usually used in infrared remote sensing. The wavelength is defined as the number of wavelength per unit length along direction of radiation transfer. The unit of wavenumber for infrared region usually is cm^{-1}. If the unit of wavelength is μm and the unit of wavenumber is cm^{-1}, the relationship between wavelength and wavenumber is expressed as

$$\lambda \cdot \nu = 10000 . \tag{2.1}$$

2) Solid angle

To analyze the radiation field, it is required to consider the electromagnetic energy confined to an element of solid angle. The solid angle is defined as the ratio of the area of a spherical surface σ intercepted at the core to the square of the radius r as shown in Figure 2.1 and in equation 2.2.

$$\Omega = \frac{\sigma}{r^2} \tag{2.2}$$

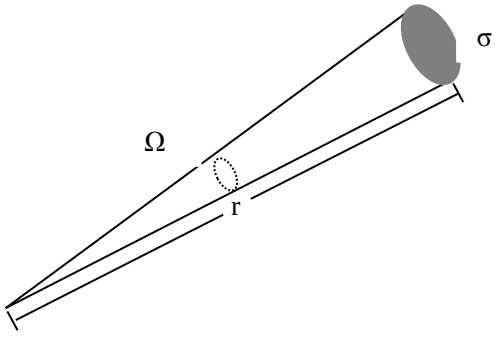

Figure 2.1 Definition of a solid angle Ω, where σ denotes the area, and r denotes the radius

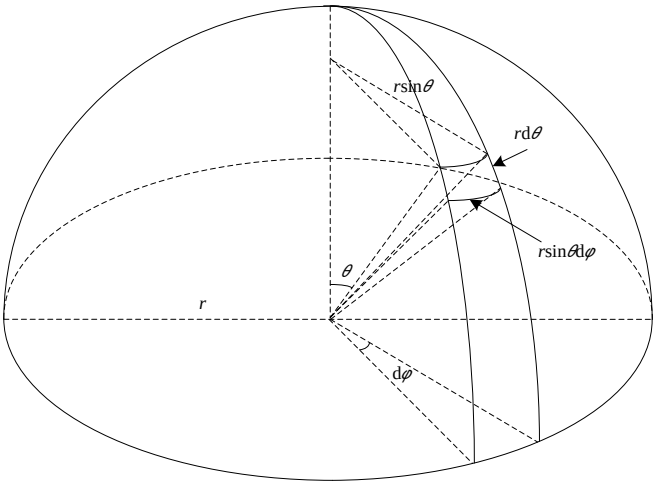

Figure 2.2 Illustration of a differential solid angle. The notifications are defined in the text.

Here, the differential solid angle is expressed as

$$\Omega = \frac{d\sigma}{r^2} = \sin\theta d\varphi d\theta , \tag{2.3}$$

where θ denotes the zenith angle, and φ denotes the azimuthal angle.

3) Radiant exitance

Radiant exitance is defined as the amount of radiant energy gives out by an emitting surface per unit area and per unit time and is expressed as

$$M = \frac{d^2Q}{d\sigma dt} , \tag{2.4}$$

where Q is the radiant energy in unit of J;

M is the radiant exitance in unit of W/m^2.

4) Irradiance

Irradiance is defined as the amount of radiation incident on a surface per unit area and per unit time and expressed as

$$E = \frac{d^2Q}{d\sigma dt}, \tag{2.5}$$

where E is the irradiance in unit of W/m^2.

5) Radiant intensity

Radiant intensity is defined as the amount of radiant energy gives out by an emitting point in unit time in directions confined to unit solid angle and is expressed as

$$I = \frac{d^2Q}{d\Omega dt} \tag{2.6}$$

where I is the radiant intensity in unit of W/sr.

6) Radiance

Radiance is the amount of radiant energy gives out by an emitting surface in unit time, which crosses unit intercepted area vertical to the direction of radiation transfer, in the directions confined to unit solid angle, which is oriented at an angle θ to the normal of the intercepted area and is expressed as

$$R = \frac{d^3Q}{d\Omega d\sigma \cos\theta dt} \tag{2.7}$$

where R is radiance in unit of W m^{-2} sr^{-1}.

7) Spectral Radiance

Spectral radiance R_λ is defined as the amount of radiance gives out by an emitting surface per unit wavelength.

$$R_\lambda = \frac{d^3Q}{d\Omega d\sigma \cos\theta dt d\lambda} \tag{2.8}$$

8) Kinetic temperature

Kinetic temperature is defined as the average temperature of the molecules in the object. It can be measured by laying the thermometer on the object or by burying the thermometer in the object (Becker and Li, 1995).

9) Brightness temperature

Brightness temperature is defined as the temperature of blackbody which gives out the same amount of radiant energy as the observed object and expressed as

$$T_b(\lambda) = B_\lambda^{-1}[R_\lambda(T)], \tag{2.9}$$

where $T_b(\lambda)$ is brightness temperature of the observed object;

T is the radiant temperature of the observed object;

R_λ is the observed spectral radiance;

$B_\lambda(x)$ is the Planck's function.

2.2 Thermal radiation theories

Any substance at a finite absolute temperature emits electromagnetic energy. Any object hot gives off light which is known as thermal radiation. The relationship between the amount of energy emitted by a blackbody, its wavelength and the temperature of blackbody is an equation known as the Planck's law.

2.2.1 Planck's law

In general, a certain fraction of the energy incident upon the surface of a solid object is absorbed and the remainder is reflected. A blackbody is defined as an idealized, perfectly opaque material that absorbs all the incident radiation at all the frequencies, reflecting none. In addition to being a perfect absorber, the blackbody also emitted all the absorbed radiation to keep its temperature stable.

According to Planck's law, given a temperature T, the spectral emittance of a blackbody is

$$E(T,\lambda)=\frac{2\pi c^2 h}{\lambda^5}(\exp\frac{ch}{k\lambda T}-1)^{-1}=\frac{C_1}{\lambda^5}(\exp\frac{C_2}{\lambda T}-1)^{-1},[W\cdot m^{-2}\cdot \mu m^{-1}] \quad (2.10)$$

where $E(T,\lambda)$ is spectral emittance, which is defined as the energy per unit time per unit wavelength crossing a unit area perpendicular to the viewing angler of the sensor;
h is the Planck constant;
λ is the wavelength in μm;
k is the Bolzmann constant;
c is the speed of the light;
$C_1=2\pi hc^2=3.7418\times10^{-16}$ W ṁ^2; $C_2=hc/k=14388$ μm Ḳ.

For a blackbody radiates uniformly in all directions, the spectral radiance $B(T,\lambda)$ can be written as

$$B(T,\lambda)=\frac{E(T,\lambda)}{\pi},[W\cdot m^{-2}\cdot sr^{-1}\cdot \mu m^{-1}] \quad (2.11)$$

where $B(T,\lambda)$ is blackbody spectral radiance, namely, the energy per unit area per unit solid angle per unit wavelength.

Sometimes, people prefer to express spectral radiance on terms of $B(T,\nu)$ rather than on

terms of B(T,λ). The spectral radiance can be written as

$$B(T,\upsilon)=\frac{2h\upsilon^3}{c^2}(\exp\frac{h\upsilon}{kT}-1)^{-1},[W\cdot m^{-2}\cdot sr^{-1}\cdot \mu m^{-1}]. \quad (2.12)$$

2.2.2 non-blackbody radiation

Generally, an object emits less energy than a blackbody and does not absorb all the incident radiation. The spectral emissivity is defined as the ratio of spectral radiance emitted by an object at a certain temperature to the spectral radiance emitted by a blackbody at the same temperature. The spectral emissivity of blackbody is unity and the spectral emissivity of non-blackbodies ranges from zero to unity. Given spectral emissivity ε(θ, λ), spectral radiance of a non-blackbody at temperature of T (K) is

$$R(\theta,\lambda)=\varepsilon(\theta,\lambda)B(T,\lambda)=\varepsilon(\theta,\lambda)\frac{2c^2h}{\lambda^5(\exp\frac{ch}{k\lambda T}-1)} \quad (2.13)$$

where θ is the incident angle.

Given spectral radiance R(θ,λ) and its actual temperature T (K), a blackbody equivalent radiative temperature T_b, also called brightness temperature, is defined as

$$B(T_b,\lambda)=R(\theta,\lambda)=\varepsilon(\theta,\lambda)B(T,\lambda). \quad (2.14)$$

2.3 Emission and scattering

To quantitatively exam the interaction of radiation with a dialectic slab, the effective reflectivity ρ, the effective transmissivity τ, and the effective absorptivity α are used expressions, where the adjective "effective" refers to the steady-state solution incorporating all multiple reflections within the slab. The relationship between the three parameters can be written as

$$\alpha(\lambda)+\tau(\lambda)+\rho(\lambda)=1. \quad (2.15)$$

According to Kirchhoff's law, for the material in thermodynamic equilibrium, α is equal to its effective emissivity ε. Here, we have

$$\varepsilon(\lambda)+\tau(\lambda)+\rho(\lambda)=1 \quad (2.16)$$

In thermal infrared remote sensing, natural surfaces is assumed to be opaque, τ = 0, in which case equation 2.16 can be written as

$$\varepsilon(\lambda) + \rho(\lambda) = 1 \cdot \tag{2.17}$$

As seen from the equation 2.17, in TIR spectral region, the effective emissivity of an object is high when its effective reflectivity is low. Otherwise, its effective emissivity is low.

For the rough surface, more general expression of the emissivity should be defined. According to Kirchhoff's Law, the emissivity of a rough surface observed at the direction (θ_v, φ_v) can be defined as

$$\varepsilon(\theta_v, \varphi_v) = 1 - \int_0^{2\pi} \int_0^{\pi/2} \rho_b(\theta_i, \varphi_i, \theta_v, \varphi_v) \sin\theta_i \cos\theta_i d\theta_i d\varphi_i \tag{2.18}$$

where θ_v is the viewing zenith angle;

φ_v is the viewing azimuth angle;

θ_i is the incident zenith angle i;

φ_i is the incident azimuth angle i;

$\rho_b(\theta_i, \varphi_i, \theta_v, \varphi_v)$ is the directional hemispherical reflectance.

2.4 Atmospheric radiative transfer theories

2.4.1 Interaction of electromagnetic energy with atmosphere

For infrared region, atmospheric absorption is mainly caused by atmospheric gases, such as water vapor, ozone, carbon dioxide. Through understanding the absorption, emission behavior of atmospheric gases, the infrared remote sensing technique is utilized to monitor the atmospheric parameters and to forecast weather condition.

In addition to these gases, other atmospheric gases such as methane and nitrous oxide also have absorption lines in the infrared region. The total transmissivity is defined as the sum of the absorption of the atmosphere.

According to the quantum theory, the absorption (or emission) of a molecule consists of sharply defined frequency lines corresponding to the transitions between sharply defined energy levels of the molecule.

1) Water vapor absorption

Water vapor has most significant absorption for electromagnetic radiation. Most of water vapor is distributed in the low layers of the atmosphere. Water vapor content varies dramatically with time and location. The higher the water vapor content, the more serious the absorption is. In infrared region, water vapor has two strong absorption bands: 2.5um - 3.0um,

and 5.0um - 7um.

2) Carbon dioxide absorption

Carbon dioxide is an important absorption gase in the infrared region. Carbon dioxide has three absorption bands in the infrared region: one around 4.3um, one from 14um to 18 um and one narrow absorption band at 2.7 um.

3) Ozone absorption

Ozone has strong absorption for electromagnetic radiation. Ozone is mainly in the 20 to 30 km altitude of the atmosphere. Ozone has two strong absorption bands: one at 0.3 um and one around 9.6 um.

Besides absorption of atmospheric constituents, atmospheric gases also emit radiation which contributes to the radiation observed at the TOA. In most atmospheric conditions, the atmospheric emission cannot deduct atmospheric absorption attenuation, so the brightness temperature observed at TOA is less than the brightness temperature of the observed object at surface. In some atmospheric cases, the brightness temperature at TOA is larger than the brightness temperature at surface.

2.4.2 Schwarzschild's equation

When electromagnetic radiation transfers in a medium, the radiation is diminished due to the absorption and scattering of the medium. Assuming the radiant intensity I_λ changes to $I_\lambda + dI_\lambda$ after passing through a thin layer of a medium with a depth of ds in the direction of transfer of radiation, we have

$$dI_\lambda = -\rho_m k_\lambda ds \tag{2.19}$$

where ρ_m is the density of the medium,
k_λ is the mass extinction coefficient.

Meanwhile, the radiant intensity increased in this transfer process due to the emission of radiation and multiple scattering of radiation by the medium. By defining the source function coefficient as j_λ,which has the same physical meaning as the mass extinction coefficient, the amount radition dI_λ added to radiant intensity I_λ is written as

$$dI_\lambda = \rho_m j_\lambda ds \tag{2.20}$$

.

By combining the decrease of radiation in equation 2.19 and the increase of radiation in equation 2.20, we have equation 2.21 to express the change of radiation intensity.

$$dI_\lambda = -\rho_m k_\lambda ds + \rho_m j_\lambda ds \tag{2.21}$$

Here, we define the source function J_λ as

$$J_\lambda = \frac{j_\lambda}{k_\lambda} . \tag{2.22}$$

So equation 2.21 can be written as

$$\frac{dI_\lambda}{\rho k_\lambda ds} = -I_\lambda + J_\lambda . \tag{2.23}$$

In TIR remote sensing, scattering of radiation by the atmosphere can be neglected. It is generally assumed that, in localized portion, the atmosphere is in thermodynamic equilibrium and being plane-parallel. When a beam of light in TIR region passes through the atmosphere, TIR radiation is simultaneously affected by atmospheric absorption and emission. Here, the source function in equation 2.22 can be defined by the planck function and equation 2.23 is expressed as

$$\frac{dI_\lambda}{\rho k_\lambda ds} = -I_\lambda(s) + B[\lambda, T(s)] \tag{2.24}$$

where T(s) is atmospheric temperature at the point where the depth of the medium in the direction of radiation transfer is s.

Here we define the monochromatic optical thickness of the medium from s to s_1 as shown in Figure 2.3 in the form

$$\tau'(s, s_1) = \int_s^{s_1} \rho k_s ds' . \tag{2.25}$$

To multiply the terms in both sides of equation 2.24 by $e^{-\tau'(s,s1)}$ and to integrate ds from 0 to s_1, we have

$$I_\lambda(s_1) = I_\lambda(0) e^{\int_0^{s_1} \rho k_s ds'} + \int_{s=0}^{s_1} B[\lambda, T(s)] e^{\int_0^{s_1} \rho k_s ds'} \rho k_s ds . \tag{2.26}$$

The first term in left side of equation 2.26 denotes the absorption attenuation of radiant intensity by the medium. The second term in the left side of equation 2.26 denotes the part of radiation emitted by the atmosphere itself. Schwarzchild (1914) proposed equation 2.24 within the context of Kirchhoff'law and without considering the scattering, and derived an integral solution of equation 2.24. Equation 2.24 is also called the Schwarzchild's equation (Liou,2002).

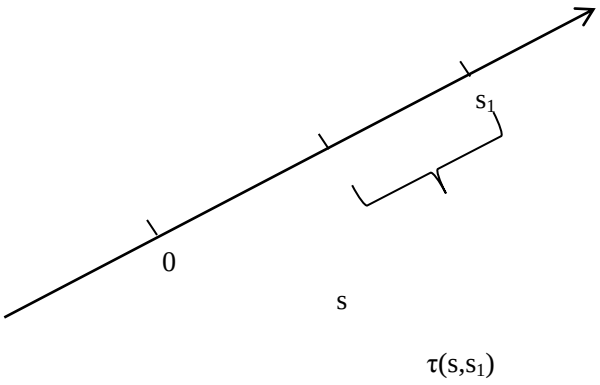

Figure 2.3 Illustration of the monochromatic optical thickness of the medium from s to s_1

2.4.3 Radiative transfer equation

For spectral radiance measured by a remote sensor at TOA, atmospheric effects cannot be ignored. Figure 2.4 illustrates the different terms in the radiative transfer equation at a wavenumber λ for the TIR spectrum, which form the spectral radiance measured by a sensor at TOA. Surface emission, which is a function LST and LSE, is denoted as [1] in Fig. 2.4. Part of spectral radiance emitted by the atmosphere reaches the surface, and then reflected by the surface towards the sensor ([2] in Figure 2.4). Meanwhile, atmosphere directly emits radiance upwards to the sensor ([5] in Fig. 2.4). For the MIR spectrum in daytime, direct solar radiance penetrate the atmosphere and part of it reaches the surface, and then is reflected by the surface towards the sensor ([4] in Figure 2.4). The atmosphere scatters the solar radiance directly upwards to the sensor ([7] in Figure 2.4). Part of solar radiance scattered by the atmosphere reaches the surface, and then is reflected by the surface towards the sensor ([3] in Figure 2.4). The spectral radiance measured by a sensor at the TOA can be written as

$$R_s(\theta_v, \varphi_v, \lambda) = R_g(\theta_v, \varphi_v, \lambda)\tau(\theta_v, \lambda) + R_{at\uparrow}(\theta_v, \lambda) + R_{s\uparrow}(\theta_v, \lambda) \quad (2.27)$$

where $R_s(\theta_v, \varphi_v, \lambda)$ is the total radiance reaching the sensor;

$R_g(\theta_{v0}, \varphi_v, \lambda)$ is the spectral radiance by a sensor at the ground;

λ is the wavelength;

θ_v is the viewing zenith angle;

φ_v is the viewing azimuth angle;

$\tau(\theta_v, \lambda)$ is the total atmospheric spectral transmittance;

$R_{at\uparrow}(\theta_v, \lambda)$ is the upwelling atmospheric radiance;

$R_{s\uparrow}(\theta_v, \lambda)$ is the upwelling atmospheric spectral diffusion radiance resulting from the scattering of solar radiance at zenith angle θ_v;

with

$$R_g(\theta_v,\lambda)=\varepsilon(\theta_v,\varphi_v,\lambda)B(T_s,\lambda)+\int_0^{2\pi}\int_0^{\pi/2}\rho_b(\theta_v,\varphi_v,\theta',\varphi',\lambda)[R_{at\downarrow}(\lambda)+R_{s\downarrow}(\lambda)]\sin\theta'\cos\theta' d\theta' d\varphi' +\rho_b(\theta_s,\theta_v,\varphi_s,\varphi_v,\lambda)E_{sun}(\theta_s,\lambda) \tag{2.28}$$

where $\varepsilon(\theta_v, \varphi_v, \lambda)$ is the land surface emissivity;

T_s is the land surface temperature;

$\rho_b(\theta_v, \varphi_v, \theta', \varphi', \lambda)$ is the bi-directional spectral reflectivity;

$R_{at\downarrow}(\lambda)$ is the downwelling atmospheric spectral radiance;

φ_s is the solar azimuth angle;

θ_s is the solar zenith angle;

$R_{s\downarrow}(\lambda)$ is downwelling hemispheric atmospheric spectral diffusion radiance resulting from the scattering of solar radiance divided by Π;

$E_{sun}(\theta_s, \lambda)$. is the direct solar spectral irradiance at the ground level;

and with

$$R_{at\downarrow}(\theta_v,\lambda)=\int_0^{p_s}B(T_p,\lambda)\frac{\partial\tau(\lambda,\theta',\varphi',p)}{\partial p}dp$$
$$R_{at\uparrow}(\theta_v,\lambda)=\int_0^{p_s}B(T_p,\lambda)\frac{\partial\tau(\lambda,\theta_v,\varphi_v,p)}{\partial p}dp \tag{2.29}$$

where $\tau(\lambda,\theta',\varphi',p)$ is the transmittance of the atmosphere between the top of atmosphere and the pressure p observed at incident angle (θ',φ');

p_s, and p is the pressure measured at the land surface and at the pressure layer p in hPa;

T_p is the atmospheric temperature at pressure layer p in K.

For the spectral radiance at TIR channels, nighttime measurement at the MIR channels, $E_{sun}(\theta_s, \lambda)=0$ and $R_{s\uparrow}(\theta_v, \lambda)= R_{s\downarrow}(\lambda)=0$. In the TIR remote sensing, we generally assume that natural land surfaces are lambertian, namely, $\rho_b(\theta_v,\varphi_v, \theta',\varphi',\lambda) =\rho_b(\theta_v,\varphi_v, \theta_s,\varphi_s,\lambda)=\rho_0$.

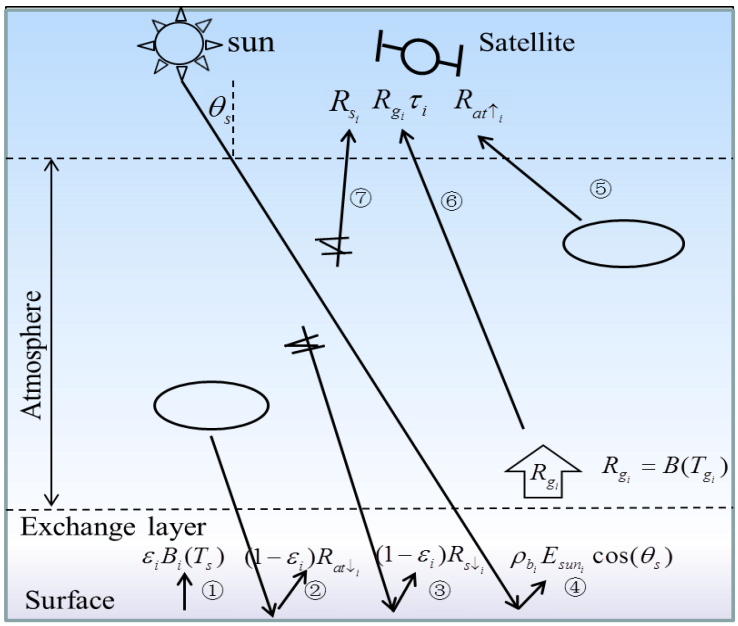

Figure 2.4 Illustration of radiative transfer equation in the infrared region. Here, path ① represents the emission emitted by the surface. Path ② represents the downwelling atmospheric emission reflected by the surface. Path ③ represents the downwelling hemispheric solar diffusion radiance divided by ∏. Path ④ represents the direct solar radiance reflected by the surface. Path ⑤represents the upwelling atmospheric radiance. Path ⑥represents the radiance observed at the ground attenuated by the atmosphere. Path ⑦ represents the upwelling solar diffusion radiance.

For a sensor onboard satellite with finite range of spectral response, the radiance measured by the sensor at channel i, the so-called channel-averaged radiance, is defined as

$$R_i(\theta_v) = \frac{\int_0^\infty f_i(\lambda) R_g(\theta_v,\lambda)\tau(\theta_v,\lambda)d\lambda}{\int_0^\infty f_i(\lambda)d\lambda} + \frac{\int_0^\infty f_i(\lambda)[R_{at\uparrow}(\theta_v,\lambda)+R_{s\uparrow}(\theta_v,\lambda)]d\lambda}{\int_0^\infty f_i(\lambda)d\lambda} \quad (2.30)$$

where $R_i(\theta_v)$ is the channel-averaged radiance;
$f_i(\lambda)$ is the spectral response function of the channel i.

For the channels with narrow spectral range (~1.0 μm), without introducing significant errors, equation 2.30 can be approximated as (Li et al., 1999)

$$R_i(\theta_v) = B_i(T_i,\theta_v) = \tau(\theta_v)B_i(T_{g,i},\theta_v) + R_{at\uparrow_i}(\theta_v) + R_{s\uparrow_i}(\theta_v) \quad (2.31)$$

with

$$B_i(T_{g,i},\theta_v) = \varepsilon_i(\theta_v)B_i(T_s,\theta_v) + [1-\varepsilon_i(\theta_v)](R_{at\downarrow_i} + R_{s\downarrow_i}) + \rho_i(\theta_s,\theta_v,\varphi)E_{sun,i}(\theta_s)$$

where T_i is the brightness temperature at TOA at channel i;

$T_{g,i}$ is the brightness temperature at ground level at channel i;

ε_i is the channel-averaged emissivity;

$R_{at\uparrow i}$ is the channel-averaged upwelling atmospheric radiance;

$R_{at\downarrow i}$ is the channel-averaged downwelling atmospheric radiance;

$B_i(T_s)$ is the channel-averaged planck function;

$R_{s\downarrow}$ is channel-averaged downwelling atmospheric diffusion radiance resulting from scattering of solar radiation;

$R_{s\uparrow}$ is channel-averaged upwelling atmospheric diffusion radiance resulting from scattering of solar radiation;

$\rho_i(\theta_s, \theta_v, \varphi)$ is the channel-averaged bi-directional reflectivity;

$E_{sun,i}(\theta_s)$ is the channel-averaged direct solar spectral radiance at the ground level;

and with

$$X_i = \frac{\int_0^\infty f_i(\lambda)X(\lambda)d\lambda}{\int_0^\infty f_i(\lambda)d\lambda} \tag{2.32}$$

where X_i is the channel-averaged terms measured at channel i;

$X(\lambda)$ is the corresponding term measured at wavelength λ.

In thermal infrared region, the solar radiation is neglected, and the natural land surface is assumed to be lambertian, namely $R_{s\uparrow i}(\theta_v) = R_{s\downarrow i} = E_{sun,i}(\theta_s) = 0$, and $\varepsilon_i(\theta_v) = \varepsilon_i$. For channels with narrow spectral interval in the TIR region, the radiance measured by sensor at channel i in equation 2.31 is expressed as

$$R_i(\theta_v) = \varepsilon_i \tau_i(\theta_v) B_i(T_s) + \tau_i(\theta_v)(1-\varepsilon_i)R_{at\downarrow_i} + R_{at\uparrow_i}(\theta_v) \tag{2.33}$$

2.5 Mixing models for mixed pixels

Mixed pixel is defined as a pixel which is consists of more than one materials. On the contrary, a pixel which includes only one material is the so-called pure pixel. Remotely sensed thermal infrared images, especially the remotely sensed thermal infrared images with low spatial resolution usually have many mixed pixels.

Component is a material that is decomposed from a mixed pixel. Component is the minimum unite in a mixed pixel. Component cannot be divided any more in the mixing model for mixed pixels. For a mixed pixel consists of vegetation, bare soil and water body, vegetation, bare soil and water body are the components for the mixed pixel. The number of components is determined according to the requirement of the operational application, the information content of remotely sensed data and the difference among the components.

Temperature unmixing is defined as a group of genetic processes by which component temperatures in a pixel is decomposed based on multi-temporal, angular, spectral, or spatial observations. Different components in a pixel can be separately distributed, jointly inter-shaded, or entirely intermingled in rural croplands.

The mixing model for mixed pixels in the thermal infrared spectrum can be expressed as a function

$$R_g = F(T_{s,1}, \varepsilon_1, S_1, T_{s,2}, \varepsilon_2, S_2, \cdots, T_{s,n}, \varepsilon_n, S_n, X) \tag{2.34}$$

where R_g is the radiance measured by at the ground for a mixed pixel;
$T_{s,n}$ is the LST of n^{th} component;
ε_n is the LST of the n^{th} component;
S_n is the abundance of the n^{th} component;
X is other parameter of component.

2.5.1 Mixing model for flat surfaces

For a flat-ground scene, the spectral radiance measured by a sensor at the ground over a mixed pixel can be modeled as a linear mixture of radiances stemming from each pure component in the pixel:

$$R_g(\theta_v, \lambda, x, y) = \sum_{j=1}^{N} (\varepsilon_{\lambda,j}(\theta_v) B(T_{s,j}, \lambda, x, y) + (1 - \varepsilon_{\lambda,j}(\theta_v)) R_{at\downarrow}(\lambda)) S_j(x, y) \tag{2.35}$$

where $R_g(\theta_v,\lambda,x,y)$ is spectral radiance measured by a sensor at the ground for the mixed pixel (x,y); N is the number of components composing the mixed pixel (x,y); $\varepsilon_{\lambda,j}(\theta_v)$ is the emissivity of the pure component j in the mixed pixel; $T_{s,j}$ is the LST of the component j in the mixed pixel; $S_j(x,y)$ is the abundance of the component j in the mixed pixel.

2.5.2 Mixing model for rough surfaces

The mixing model for flat surfaces is not suitable for ground surface with 3D structure. Li extended the mixing model for flat surfaces to heterogeneous 3D surfaces (Li et al. 1999). Fontanilles developed a mixing model for urban surfaces (Fontanilles et al. 2010). Cubero Custan proposed a mixing model to combine component radiance at a fine aggregation surface (Cubero-Castan et al. 2012). According to mixing model in (Cubero-Castan et al. 2012), the spectral radiance measured at the ground over a mixed pixel is a combination of the radiance emitted by components in the pixel R_{emis}, the radiance of component j reflected

by component i R_{emis}^{neig}, the downwelling atmospheric radiance reflected by each component $R_{atm,\downarrow}$, and the downwelling atmospheric radiance reflected by the neighborhood component R_{emis}^{neig}:

$$R_g(\theta_v, \lambda, x, y) = R_{emis} + R_{atm,\downarrow} + R_{emis}^{neig} + R_{atm,\downarrow}^{neig} \tag{2.36}$$

In the infrared spectral region, we assume that the atmospheric radiance reflected by neighborhood is small in comparison with the emissive neighborhood radiance. Following Kirchof's law, the hemispheric directional reflectance is related to hemispheric directional emissivity by ρ+ε=1. The definition of the aggregation surfaces is shown in Figure 2.5, which is useful to represent fine surfaces of urban 3D structures. Given a scene composed by many facets, the emissivity of facet i $\varepsilon_{\lambda,i}$, and the temperature of facet i $T_{s,i}$, equation 2.36 can be expressed as

$$\begin{aligned} R_g = & \sum_i (\varepsilon_{\lambda,i} \cdot B(T_{s,i}) + \frac{(1-\varepsilon_{\lambda,i})}{\pi} \cdot R_{atm,\downarrow}) \cdot \frac{\Delta\Omega_i}{\Omega_s} \\ & + \sum_i \sum_{j \neq i} \frac{(1-\varepsilon_{\lambda,i})}{\pi} \cdot \varepsilon_{\lambda,j} \cdot B(T_{s,j}) \cdot \frac{\Delta\Omega_{j \to i}}{2\pi} \cdot \frac{\Delta\Omega_i}{\Omega_s} \end{aligned} \tag{2.37}$$

where $\Delta\Omega_i$ is the solid angle on which the facet i is seen by the sensor, and Ω_s is the instantaneous field of view of the sensor; $\Delta\Omega_{j\to i}$ is the solid angle on which facet j is seen by facet i.

The mixing model is nonlinear model because multiple reflections due to the 3D structure are taken into account and that the planck's law is used.

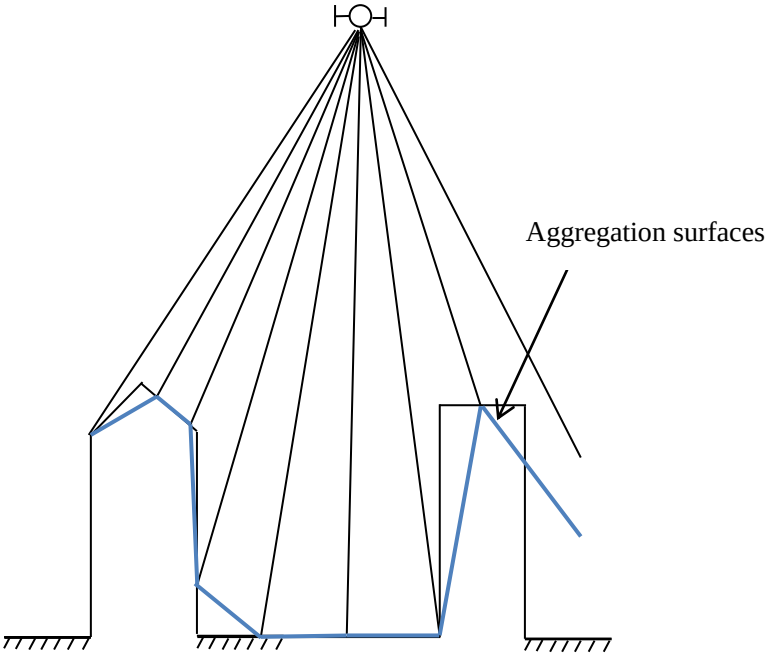

Figure 2.5 The illustration of aggregation surfaces in instantaneous field of view (Blue: aggregation surfaces).

3 State of art of estimation of LST and unmixing component temperatures from TIR data

LST is a key parameter in climate systems. TIR remotes sensing is an effective way to acquire LST over vast region.

Space-borne multispectral TIR sensors exist for a long time and provide large amount of data for retrieving LST over regional or global regions. With the development of hyperspectral TIR sensor, hyperspectral TIR data is an important source of information for retrieving LST from space. Various methods exist to retrieve LST from the multispectral and hyperspectral TIR data.

The LST retrieval methods mentioned above only retrieve a single LST for a pixel. It is not correct for heterogeneous surfaces. Various methods exist to unmixing component temperatures from TIR data.

3.1 Review of methods for retrieving LST from space-borne TIR data

3.1.1 LST retrieval methods for multispectral TIR data

Multispectral TIR data observed at the TOA is an important type of satellite data for retrieving LST in large spatial scale. For retrieving LST from multispectral TIR data observed at TOA, there are the two important steps: atmospheric correction and temperature and emissivity separation. According to the characteristics of the LST retrieval methods, the LST retrieval methods can be classified into: stepwise methods for retrieving LST and LSE from multispectral TIR data, methods for simultaneously retrieving LST and LSE and methods for simultaneously retrieving LST, LSE and atmospheric profile.

3.1.1.1 Stepwise methods for retrieving LST from multispectral TIR

data

In this case, LST and emissivity are retrieved in two steps: LSE is firstly determined, and then LST is retrieved using the determined emissivity. The proposed stepwise LST retrieval methods include: single-channel method, the multi-channel method, the multi-angle method.

1) Single-channel method

With emissivity value calculated in advance, the single channel method uses satellite data observed at one channel located in the atmospheric window for retrieving LST by inversion of the radiative transfer model in equation 2.33 and by correcting of the effects atmospheric attenuation and emission from radiance observed at TOA using atmospheric radiative transfer code with atmospheric profile data. The atmospheric profile data can be obtained either from the ground-based atmospheric radiosounding, from satellite vertical sounders, the weather forecasting model (e.g. ECWMF, NCEP).

To reduce the dependence of the single-channel method on the atmospheric profile data, several algorithms are developed by parameterizing the atmospheric profile. Qin proposed a method to retrieve LST from Landsat-5 data using only the near-surface atmospheric temperature and water vapor content and using a linear relationship between the atmospheric transmittance and total water vapor content (Qin et al. 2001). Jiménez-Muñoz, Jiménez-Muñoz and Cristóbal provided a method for retrieving LST from any satellite TIR data with FWHM (full width at half maximum) of about 1 um with the known LSE and the known total water vapor content (Jiménez‐Muñoz and Sobrino 2003; Jimenez-Munoz et al. 2009). This algorithm requires minimum input data and can be used for any sensors using the same equation and coefficients.

It should be noted that the single-channel methods requires accurate LSE, which is rarely known.

2) Multi-channel method

An alternate method, the so-called split-window method, was first proposed by McMillin to estimate Sea Surface Temperature (SST) from satellite data and was extended to retrieve LST from space (McMillin 1975). This method relies on the phenomenon that the atmospheric attenuation suffered by the surface emitted radiance is proportional to the difference between the at-sensor radiances measured simultaneously in two adjacent channels. On the basis of the first order of the Taylor series of the radiative transfer equation, LST can be retrieved by a linear function of at-sensor brightness temperatures centered at two adjacent TIR channels in the spectral region of 10~12.5 μm. With the known LSE of two adjacent channels, a typical linear split-window algorithm can be written as equation 3.1 (Becker and

Li 1990; Prata 1993; Sobrino et al. 1994; Becker and Li 1995; Wan and Dozier 1996; Tang et al. 2008; Atitar and Sobrino 2009).

$$T_s = a_0 + a_1 T_i + a_2 (T_i - T_j) \tag{3.1}$$

where T_i and T_j are brightness temperatures measured at two adjacent channels and a_i (i=0,1,2) are coefficients related with the spectral response function of two adjacent channels, the two channel LSEs ε_i and ε_j and the water vapor column (WV) and the viewing zenith angle (VZA). The coefficients a_i (i= [1,2]) are pre-determined by fitting the simulation data with various atmospheric conditions and various LSE conditions or by comparing the satellite data against the matched in-site LST data. Different split-window algorithms, using linear and nonlinear functions of brightness temperatures of the two channels, are developed by employing a combination of LSE, WV and the VZA for parameterizing the coefficients a_i (i= [1, 2]) (Becker and Li 1995; Wan and Dozier 1996; Coll and Caselles 1997; Francois et al. 1997; Sun and Pinker 2003; Sobrino et al. 2004a; Sobrino and Romaguera 2004b; Sun and Pinker 2007). Because of its little requirement of atmospheric data, which is difficult to obtain for most of the satellite sensors, and also because of its easy operation, the multi-channel method is applied to many satellite sensors, such as the AVHRR, MODIS, SEVIRI, FY-3 (Kerr et al. 1992; Wan and Dozier 1996; Sun and Pinker 2003; Jiang and Li 2008; Tang et al. 2008; Hulley and Hook 2011). Because of accurate LSE is hard to acquire, the LST cannot be retrieved as accurate as the SST using the split-window method.

When satellite TIR sensors with more than two channels were available, LST can be retrieved by a linear or nonlinear function of at-sensor brightness temperatures of more than two TIR channels using the methods as the split-window methods (Sun and Pinker 2005, 2007). Assuming channel LSEs are known in advance, Sun and pinker (2003) developed a three-channel linear algorithm to retrieve night-time LSTs from the Geostationary Operational Environmental Satellite (GEOS) data using a linear function of brightness temperatures in two TIR channels and one MIR channel. The three-channel algorithm is expressed as

$$LST = d_0 + (d_1 + d_2 \frac{1-\varepsilon_i}{\varepsilon_i})T_i + (d_3 + d_4 \frac{1-\varepsilon_j}{\varepsilon_j})T_j + (d_5 + d_6 \frac{1-\varepsilon_{i1}}{\varepsilon_{i1}})T_{i1}, \tag{3.2}$$

where T_i and T_j are the brightness temperatures at TOA in the two TIR channels;

T_{i1} is the brightness temperature at TOA in the MIR channel;

ε_i and ε_j are the LSE measured in the two TIR channels;

ε_{i1} is the LSE measured in the MIR channel.

d_i (i=[1,6]) are the constant coefficients independent on the atmosphere and the VZA.

Furthermore, Sun and pinker (2005) proposed a four-channel non-linear algorithm to retrieve night-time LSTs from the Spinning Enhanced Visible and Infrared Imager (SEVIRI)

data with coefficients depending on the land surface types to account for LSE effects. To account for the solar radiation during the daytime, a solar correction term $d_6 T_{i1} \cos\theta_s$ should be added to equation 1.2 or a solar correction must be performed to the T_{i1} using methods proposed by Adams et al. (1989) and Mushkin et al. (2005) (Adams et al. 1989; Mushkin et al. 2005). Evaluation with ground observations shows that the LST retrieved by the four-channel multi-channel method is more accurate than those obtained by the generalized split-window algorithm. Error of solar correction and the phenomenon that the variation of MIR channel LSE is larger than the TIR channel LSEs harm the wide application of the multi-channel method.

3) Multi-angle method

Similar to the SW method, the multi-angle method relies on that the differences among the at-sensor brightness temperatures measured at different viewing angles in a given channel for the same object is proportional to the atmospheric attenuation suffered by the surface emitted radiance. Assuming LST and LSE are independent on the VZA and the atmosphere is horizontally uniform and stable over the observation time, with the known LSE in the given channel, Prata (1993, 1994) developed a dual-angle method to retrieve SST and LST from ATSR data. The dual-angle method can be expressed as

$$T_s = \frac{1}{\varepsilon_i} T_n + \frac{p_1}{\varepsilon_i}(T_n - T_f) + p_2 \frac{1-\varepsilon_i}{\varepsilon_i}, \tag{3.3}$$

where ε_i is the LSE measured at the given channel,

p_k (k=1,2) are the constant coefficients,

T_n and T_f are the at-sensor brightness temperatures measured in the nadir and forward views. Sobrino (1996) developed an improved dual-angel algorithm which accounts for the emissivity at nadir ε_n and the emissivity at forward view ε_f (Sobrino et al. 1996):

$$T_s = T_n + p_1(T_n - T_f) + p_2 + p_3(1-\varepsilon_n) + p_4(\varepsilon_n - \varepsilon_f), \tag{3.4}$$

where p_k (k=[1,4]) are coefficients related to atmospheric transmittances and mean air equivalent temperatures in the nadir and forward views. This algorithm is only dependent on the LSEs and not dependent on the WV. To reduce the influence of the WV on the LST retrieval, Sorbrino (2004c) proposed a nonlinear dual-angle algorithm using a nonlinear function of (T_n-T_f) to estimate atmospheric attenuation suffered by the surface emitted radiance and using a combination of WV and LSEs at the nadir and forward views to parameterize the coefficients. Comparison of the nonlinear dual-angle algorithm with the nonlinear SW algorithm incorporating LSEs, WV, and VZA showed that the dual-angle

algorithm performs better than the SW algorithm provided that the spectral and angular variations of the LSEs are well known (Sobrino and Jimenez-Munoz, 2005). However, the multi-angle method suffers from the angular dependence of LSE and angular dependence of LST and mis-registration when applied to satellite data.

3.1.1.2 Methods for simultaneously retrieving LST and LSE

The LST retrieval methods above (such as the single channel method, multi-channel method, multi-angle method) require accurate LSE in advance, which causes much error to the retrieved LST when error of LSE is significant. Therefore, it is needed to retrieve LST and LSE simultaneously.

1) Gray body method

With TIR data measured at N channels, N equations can be obtained. Assuming atmospheric correction is well performed, we have N+1 unknowns (1 LST and N LSEs) in the N equations. It is an ill-posed problem to solve LST and LSE from the N equations. The method assumes LSE does not change with wavelength for wavelengths larger than 10 um. For two or more TIR channels, the number of unknowns are equal to or less than that of radiative transfer equations in this case, and then LST and LSE will be retrieved from the multiple-channel TIR data (Barducci and Pippi 1996). The gray body method is accurate for dense vegetation and water body, but it is difficult to be applied to surfaces with high emissivity spectral contrast. Moreover, the gray body method has large error when atmospheric correction is not accurate.

2) Temperature and Emissivity Separation method (Zhou et al.)

The TES method relies on an empirical relationship between the minimum channel LSE and spectral contrast of LSE to increase the number of equations, which makes the ill-posed problem deterministic (Gillespie et al. 1998).

The TES method includes three modules: Normalization Emissivity Method (NEM) (Gillespie, 1995), the Spectral Ratio (SR), the maximum minimum apparent emissivity Difference Method (MND) (Matsunaga, 1994). Assuming maximum channel LSE of each pixel is a constant, the NEM estimates the initial LST from the atmospherically corrected TIR radiances. The SR is to calculate the ratio of normalized emissivities to their average. The SR can describe the shape of emissivity accurately even if the initial LST is coarsely estimated. With the results of the SR method, the MMD is utilized to derive the minimum channel LSE using an empirical relationship between the minimum channel LSE and the spectral contrast of channel LSEs. Once the minimum channel LSE is estimated, other channel LSEs can be retrieved by the SR method and the LST can be refined and estimated.

The TES method can be applied to all the land surfaces without requiring known spectral variation in the LSE spectra. The TES method is accurate for surfaces with high emissivity spectral contrast such as rocks and soils (Gillespie et al. 1998; Sobrino et al. 2008), but the TES method exhibits much error for surfaces with low emissivity spectral contrast (e.g. water, snow, vegetation) and for hot and wet atmospheric conditions (Sawabe et al. 2003; Coll et al. 2007; Hulley and Hook 2009b, 2011; Gillespie et al. 2011).

3) Two Temperature Method (TTM)

The TTM relies on that LSE is unchanged during two observations to increase the number of equations. In this method, TIR data at N channels correspond to N×2 equations and N+1 unknowns. When a sensor has N ≥ 2, LST and LSE can be retrieved by this method from the two observations (Watson, 1992). TTM doesn't require any assumption about the shape of the emissivity spectrum, except that the emissivity spectrum is time-invariant. However, the high correlation of the radiative transfer equations at two adjacent TIR channels cause the retrieval sensitive to error of atmospheric correction and error of the measured data (Gillespie 1986; Caselles et al. 1997; Watson 1992) and the mis-registration degrades the accuracy of the method (Wan 1999).

4) Physics-based day/night operational method

Wan and Li (1997) further developed a physics-based day/night method (D/N) to simultaneously retrieve LST and LSE from a combined use of the day/night pairs of MIR and TIR data (Wan and Li 1997). The method assumes that emissivities are unchanged from day to night and the angular form factor has very small variations in the MIR spectral region of interest to reduce the number of unknowns and make the retrieval stable. To reduce the error of atmospheric correction on the retrieval, the air temperature at the surface level and the water vapor column are introduced to modify the initial atmospheric profile in the retrieval.

The D/N method improved accuracy of the LST and LSE by using measurements at the MIR channels to reduce the high correlation of radiative transfer equations and by refining the atmospheric data with near-surface air temperature and the water vapor column. However, similar to other multi-temporal method, the D/N method suffers from the critical problem of mis-registration and the variation of LSE in the VZA. Moreover, the D/N method requires at least seven channels in MIR and TIR wavelength.

3.1.1.3 Methods for simultaneously retrieving LST, LSE and atmospheric profile

The methods for simultaneously retrieving LST, LSE require accurate atmospheric data for atmospheric correction, but the atmospheric data, which are synchronously measured with the satellite data, is not always available. It is ideal to retrieve LST, LSE and atmospheric profile simultaneously from TIR data. Ma (2000) first developed a two-step physical retrieval method to simultaneously retrieve LST, LSE and atmospheric profile from MODIS data by assuming that LSEs are constant in the MIR channels and in the TIR channel and by ignoring the solar contribution in the MIR channels (Ma et al. 2000). Ma (2002) further developed an extended TRSM method by considering the solar contribution (Ma et al. 2002).

The TSRM method stems from the physics-based atmospheric profile retrieval method. Firstly, the TRSM method is to tangent-linearize the atmospheric radiative transfer equation with respect to the atmospheric temperature and moisture profile, LST and LSE. After that, a large amount of the equations are obtained by using the differential technique with the first-guess atmospheric temperature and moisture profile, LST and LSE. Finally, Newton iteration is ultilized with the regularized solution as the first-guess values to find the final maximum likelihood solution of the atmospheric temperature and moisture profile, LST and LSE.

Unlike the other methods, the TSRM method doesn't require accurate atmospheric correction. However, the TSRM method is highly dependent on the initial guess (Ma et al. 2002). And, due to the physical nature of the TSRM method, it requires adequate number of channels in specific window, and its complex nature causes a low computational efficiency. These shortcomings make it difficult to apply the method to satellite data. Moreover, the reduction of unknowns in radiative transfer equation degrades the accuracy the TSRM method.

3.1.2 LST retrieval methods for hyperspectral TIR data

Hyperspectral TIR data with thousands of continuous bands has high spectral resolution, therefore allows improving the accuracy of the retrieval of the atmospheric profile, LST and LSE. The LST retrieval methods for multispectral TIR data have their advantages and disadvantages. Moreover, selection of the LST retrieval method is dependent on the characteristic of the sensor. It is required to develop methods to retrieve surface and atmospheric parameters from hyperspectral TIR data.

3.1.2.1 Iterative Spectral Smooth Temperature/Emissivity Separation (ISSTES) method

Basing on that the typical LSE spectrum is smooth in comparison with the spectral

feature caused by atmospheric absorption and radiation to reduce the number of unknowns, Borel (1997) proposed the ISSTES method to iteratively retrieve LST and LSE from hyperspectral TIR data provided the atmospheric correction is accurately performed (Borel 1997). If LST is not accurate, the LSE spectrum calculated by inverting the radiative transfer equations will exhibit the atmospheric spectral feature, namely there will be sawteeth on the estimated LSE spectrum. The LST and LSE are estimated when the spectral smoothness S of the retrieved LSE spectrum is maximized. After that, different smoothness indexes, which utilizing the first and second derivative of LSE spectrum, have been proposed (Kanani et al. 2007; Borel 2008; Cheng et al. 2010; OuYang et al. 2010), although they have the same statistical performance regardless of the detail of the smoothness index.

Ingram and Muse (2001) evaluated the method's sensitivity to the smoothness assumption and measurement noise and found that the assumption doesn't cause significant error to the retrieved results but the retrieval accuracy of the method dependent on the SNR (Ingram and Muse 2001). Moreover, the method requires that atmospheric correction is accurately performed. Wang (2011) reported that the occurrence of singular point may lead to difficulty in finding the acceptable solution when LST is close to the equivalent temperature of atmospheric downwelling radiance.

3.1.2.2 Linear emissivity constraint temperature and emissivity separation method (LECTES)

The LECTES assumes the LSE spectrum can be divided into M segments and that LSE in each segments varies linearly with the wavelength. As a result, the retrieval of LSE becomes retrieval of the coefficients of each line, which reduces the number of unknowns (Wang et al. 2011). For hyperspectral TIR data with M segments (n channels in each segments), the number of equations is $n \times M$ and the number of unknowns is $M \times$ 2LSE+1LST. The requirement of $n \times M \geq 2M+1$ is easily fulfilled for hyperspectral TIR data because thousands of channels are available.

Wang (2011) analyzed the sensitivity of the method to the proposed assumption and found that the error caused by the assumption can be negligible if the width of each segment is well chosen. A width of segment of 10 cm^{-1} is recommended. In comparison with the ISSTES method, this method produces fewer singular points and is more resistant to both white noise and error in the downwelling atmospheric radiance. Similar to ISSTES method, LECTES method is only suitable for hyperspectral TIR data and requires accurate atmospheric correction.

3.1.2.3 Linear Empirical Orthogonal Function regression method

The traditional statistical regression method cannot be applied to hyperspectral TIR data of high dimension, which is called the “curse of dimension”, therefore dimension reduction techniques are required for LST retrieval using the hyperspectral TIR data. The linear EOF regression method bases on the principal component analysis (PCA) technique to simultaneously retrieve atmospheric profile, LST and LSE (Zhou et al. 2011). The PCA technique is ultilized to convert the TIR radiance spectrum to amplitudes in EOF dimensions with a transformation matrix determined in advance using simulation data. Given the EOF amplitudes of the hyperspectral TIR radiance spectrum, LST can be retrieved by a linear function of EOR amplitudes of hyperspectral TIR radiance spectrum and of the surface pressure.

The linear EOF regression method ultilizes only the spectral information in the radiance spectrum, and doesn’t require any atmospheric data and LSE data. Moreover, the method is fast enough to be applied to satellite data. However, the method relies on an empirical linear relationship between the principal component scores and the state parameters, which make the accuracy of the method dependent on the simulation data.

3.1.2.4 ANN method

ANN can robustly perform highly complex, non-linear, parallel computations. ANN is widely used by the remote sensing community (Mas and Flores 2008). ANN method simulates the function of the brain in two steps: acquiring the knowledge by a learning process; storing knowledge using interneuron connection strengths (Mas and Flores, 2008).

In comparison with other existing LST retrieval methods, the main advantage of the ANN methods is their ability to learn complex pattern, their generalization ability to noisy environments, their abilities to incorporate of both experimental knowledge and physical constraints (Mas and Flores, 2008). Due to the nonlinear feature of the ANN method, ANN methods are employed to retrieve surface and atmospheric parameters without knowledge of the complex physical mechanisms. For example, Mao (2008) used an ANN to retrieve LST and LSE from ASTER data and Aires (2002b) and Blackwell (2005) used an ANN to retrieve atmospheric profiles from hyperspectral TIR data (Aires et al. 2002b; Blackwell 2005; Mao et al. 2008). To reduce the effect of coupling between the surface and atmosphere, Aires (2002b) used an ANN to retrieve both the atmospheric and surface temperatures assuming LSE is unity, and Wang (2010) established an ANN to simultaneously retrieve the LST, LSE and atmospheric profiles from the hyperspectral TIR data (Wang et al. 2010). RMSEs of the LST and temperature profiles in troposphere are about 1.6K and 2K, respectively; RMSE of LSE is less than 0.01 in the spectral interval from 10 μm to 14 μm.

The ANN performs like the black boxes, the retrieval process cannot be well controlled

and it is difficult to determine the weights assigned to each input and to improve the output due to the complex nature of the network. Moreover, the accuracy of the ANN method depends on its architecture and the training data (Mas and Flores, 2008), which are difficult to obtain. The architecture and the learning scheme are directly related to their ability to learn and generalize. The characteristics of the training data, such as the size and the representativeness, are also of considerable importance. The use of too few samples will cause large error to the retrieved results, while the use of too many samples will result in that it requires much time for training.

3.1.2.5 The extended two step retrieval method

Li (2007) firstly proposed the extended TSRM method to simultaneously retrieve LST, LSE and atmospheric profile from hyperspectral TIR data by assuming the LSE spectrum can be represented by several principal component scores to reduce the number of unknowns (Li et al. 2007). Similar to TSRM method, this method includes three steps: linearizing of atmospheric radiative transfer equation, solving a lot of equations with the first-guess values, refining the estimated atmospheric and surface parameters using Newton iteration with the regularized solution as the first-guess values. To stabilize the solution of surface and atmospheric parameters, various LSE constraints were proposed to reduce the number of unknowns and various regularization techniques (Masiello and Serio 2013; Wang et al. 2013a) were developed to find the optimum regularization parameter, and no-linear ANN method was employed to improve the accuracy of the first-guess values (Wang et al. 2013a). Meanwhile, evaluation of the retrieval accuracy of the extended TSRM method with simulation data showed that: LST can be retrieved by the method with RMSE of 1 K; RMSE of the retrieved LSE ranges from 0.01 to 0.02 in the wavelength region between 10 μm and 12 μm (Wang et al. 2013a).

The extended TSRM method doesn’t require extra atmospheric information, and the retrieval accuracy of the method is better than those of the empirical methods (Wang et al. 2013b). However, similar to the TSRM method, the extended TSRM method is difficult to be applied to satellite data because of its complex nature.

3.2 Review of methods for unmixing temperature from TIR data

3.2.1 Temperature unmixing methods for low/medium spatial resolution TIR data

As mentioned above, the component temperatures are an important parameter in many applications. However, the methods mentioned above are developed for retrieving a single LST for a pixel from satellite TIR data. It is need to develop methods to decompose the component temperatures from various satellite data, which are called TUM methods in the literature.

For TIR data with N channels measured over a mixed pixel containing 2 components, the unkonwns includes 2 component temperatures, 1 fraction of the hot component, N channel emissivities of 2 components, which is significantly larger than the number of radiative transfer equations for multi-spectral TIR data. It is more challenging to retrieve component temperatures from TIR data.

3.2.1.1 Multi-angle TUM method

The multi-angle TUM method is a long-established method which retrieves the component temperatures by inverting the forward thermal radiative transfer process (Jacob et al. 2008; Menenti et al. 2008). The fundamentals of multi-angle TUM methods are the angular-dependent component temperature and emissivity, which results in a directional effect in the thermal radiance observed at various spatial scales. Li (1999) proposed a conceptual model for effective directional emissivity from non-isothermal surfaces to account for the effects of 3D-structure and heterogeneity on the directional TIR measurements (Li et al. 1999). To reduce ill-posed problem of model inversion, Jia (2003) proposed a method to retrieve soil and foliage component temperatures from bi-angular ATSR-2 data by estimating the fractional vegetation covers (FVCs) from visible, near-infrared and shortwave infrared measurements within a pixel and by inverting the linear mixing model using the retrieved FVCs and the atmospherically corrected TIR radiance data (Jia et al. 2003). To retrieve more than two components, Timmermans (2009) proposed an algorithm to retrieve sunlit/shaded soil, sunlit/shaded leaf component temperatures from simulated directional thermal measurements and field measurements by Bayesian inversion of no-linear soil-vegetation-atmosphere transfer model (Timmermans et al. 2009).

The multi-angle TUM method requires multi-angle data, for which the time continuity is highly deficient. Moreover, this method is designed for specific vegetation types and geometrical structures which are difficult to parameterize analytically.

3.2.1.2 Multi-spectral TUM methods

Dozier (1981) developed a physics-based method to retrieve the component fractions and component temperatures which is modified and widely applied to various sensors. This multi-spectral TUM method retrieves temperatures and fractions of two sub-pixel objects by solving the linear mixing model for combining the radiance of components with two assumptions: that the two components are blackbodies and that background object's temperature can be obtained from adjacent pixel. This method cannot use to separate soil and vegetation temperatures. To unmixing soil and vegetation temperatures over mixed pixels, Song (2007) proposed a constraint optimization algorithm – the genetic algorithm – to retrieve soil/vegetation component temperatures from MODIS satellite data with neglecting nonlinear factors such as the vertical structure, the conductance and the convection between the two components, in combination of the component radiations.

The multi-spectral TUM methods are widely used because the multispectral satellite data is available. And these methods are designed for specific land surface types, for which component emissivities are known. The uncertainty in component emissivities, the emissivity directionality (Li, 1999) and the nonlinear additive relationship of components (McCabe et al. 2008) degrade the accuracy of these multi-spectral TUM methods.

3.2.1.3 Multi-pixel and multi-resolution TUM methods

The multi-pixel and multi-resolution TUM methods both rely on assumption that the component temperatures doesn't change in a specific spatial scale. Multi-pixel TUM method utilizes the geographical correlation among component temperatures of adjacent pixels in which the associate component fractions differ pixel by pixel. The multi-resolution TUM method utilizes multi-resolution data.

Dozier (1981) first proposed a multi-pixel TUM method by assuming that the background temperatures and the temperatures of hot components of the adjacent pixels are the same and that the component fractions differ from each other. This assumption is correct when the temperature contrast between components is high. In reality, slight variations of component temperatures among adjacent pixels appear (Barducci et al. 2004), and Zhan (2011) used a quadric function to express the gradual and spatial variations of component temperatures (Zhan et al. 2011b). Other multi-pixel TUM methods employ a trapezoidal (Zhang et al. 2005; Zhang et al. 2008) or a triangular shape in the VI-LST feature space to

retrieve soil and vegetation component temperatures.

To build the convex polygon in a feature space, the multi-pixel and multi-resolution TUM methods require a large number of adjacent pixels in which the surface parameters have large variations pixel by pixel. And it is difficult to fit the dry edge and wet edge of the formulated trapezoids or triangles. The uncertainty in components selection degrades the accuracy of the retrieved component temperatures. Besides, application of spatial autocorrelations of physical properties among neighboring pixels partially decreases the spatial resolution of decomposed component temperatures (Zhan et al. 2011b). The last shortcoming of these methods is the neglect of horizontal advection at high spatial resolution (Zhang et al. 2005).

3.2.1.4 Multi-temporal TUM method

Due to high deficiency of the multi-angular TIR data, Zhang (2003) proposed a method to retrieve component temperatures using bi-temporal field measurement and NOAA/AVHRR data (Zhang et al. 2003a). This multi-temporal TUM method inverts the linear mixing equations for soil and vegetation component temperatures at two time by using the fact that radiometric temperature difference between soil and vegetated surface are close to zero when net radiation is equal to zero and by using a linear relationship between Diurnal Amplitude (DA) of radiometric temperatures of soil and the DA of radiometric temperatures of mixed pixel. The coefficients in these linear relationships are determined in advance using field measurements with a given percentage of vegetation cover (PVC). The soil and vegetation radiometric temperatures are converted to true surface temperatures with estimated component emissivities.

The multi-temporal TUM method requires the assumption that a mixed pixel consists of soil and vegetation, which is not suitable for heterogeneous surfaces. Its requirement of field measurements, is another shortcoming of this multi-temporal TUM method. Also, the temporal resolution of satellite TIR data is low, which cause that least attention is shown on the multi-temporal method.

3.2.2 Methods for unmixing temperatures from high spatial resolution TIR data

TIR data with high spatial resolution, especially hyperspectral TIR data with high spatial resolution, can provide spectral and spatial information about the composition of heterogeneous surfaces and it is useful for retrieving parameters of components. The above TUM methods are not suitable for TIR data of high spatial resolution because the component

emissivities in high spatial resolution imagery are different from those in low and medium spatial resolution imagery. It is in urgent need to develop TUMs for this type of the TIR data.

3.2.2.1 The Spectral Unmixing and Thermal Mixing (SUTM) method

Assuming component temperatures invariant in the image scene, the SUTM method retrieves the component temperatures of vegetation/wet soil/bright impervious surfaces and dry soil/dark impervious surfaces from Landsat ETM+ data by utilizing both the reflectance data and the TIR data. The component temperatures of these land surface types are derived by using the triangular shape in the feature space scatterplot of the VI and the LST. The LST image at a higher spatial resolution is derived by applying a linear mixing of component temperatures with the reflectance data.

The SUTM method takes into consideration of the four component land surface type rather than the two land surface types of soil and vegetation, and can be applied to urban surfaces. However, the neglect of gradual spatial variation of the component temperatures causes much error to the results of the method and the method requires reflective wavelengths. Another shortcoming of this method is the neglect of the nonlinear effects of conductance and horizontal advection.

3.2.2.2 Physics-based TUM method

The physics-based TUM method, also called the TURST method, simultaneously retrieve component temperatures and component fractions by inverting the radiative transfer equations provided atmospheric correction is accurately performed and the component emissivities are accurately retrieved (Cubero-Castan et al. 2015).

In the first step, the first-guess component temperatures and component emissivities are derived for all the components from pure pixels using TES method with atmospherically corrected radiances.

In the second step, assuming that variation of component temperature is close to the mean component temperature, that the emissivity of component ε_i is known, and that component abundance S_i is known, component temperatures are retrieved by inverting linearized radiative transfer equations using the best linear unbiased estimator. The linearized radiative transfer equations are derived by the first-order approximation of BOA radiance. In this step, the mean component temperatures, component abundances, component emissivities are assumed to be known. If the component abundances are unknown, the component temperatures and abundances are retrieved by minimization of the reconstruction error in the

next step.

In the third step, component temperatures and component abundances are determined simultaneously by the TRUST method using two cost functions. For each set of materials that could compose the mixed pixel, with all the possible values of component abundances, component temperatures and component abundances are retrieved by a minimization of the reconstruction error using the cost function $D(\vec{S})$. The cost function $D(\vec{S})$ is expressed as

$$D(S) = \sqrt{\frac{1}{N_\lambda}\sum_{\lambda}\left(\frac{R_s(\lambda) - R_{atm\uparrow}(\lambda)}{\tau_{atm\uparrow}(\lambda)} - R_g(\vec{S}, \vec{T}_s, \lambda)\right)^2} \tag{3.5}$$

where N_λ is the number of the used channels; $\vec{S}$ is the fractions of meterials composing the mixed pixels; $R_s(\lambda)$ is the satellite measured radiance at λ μm; $R_{atm\uparrow}(\lambda)$ is the upwelling atmospheric radiance; $\overrightarrow{T_s} = \{\overline{T_{s,i}} + \Delta T_{s,i}, i=<1,N>\}$ is the estimated component temperatures and $\overrightarrow{\Delta T}$ is calculated in the second step and depends on component abundances $\vec{S}$. Then, a second minimization is performed to determine the true set of materials. To identify the classes of materials with the same emissivity but different temperatures, a second cost function is introduced

$$D_T(\vec{S}) = D(\vec{S}) + \gamma\sqrt{\frac{1}{N}\sum_{i=1}^{N}(\Delta T_{s.i})^2} \tag{3.6}$$

where γ is a parameter which weighs the impact of the estimation of $\Delta T_{s,i}$.

The TRUST method can retrieve component temperatures for surfaces with small standard deviations of component temperatures from high spatial resolution TIR images. But the TRUST method requires that the variations of component temperatures are small and has large error if a pixel contains more than two components. The requirement of images in the reflective domain also hampers its wide application.

3.3 Drawbacks of current methods and possible solutions

3.3.1 Drawbacks of current methods for retrieving LST from hyperspectral TIR data

With the so-called ill-posed problem, it is difficult to retrieve LST from hyperspectral TIR data. Specifically, the difficulties in retrieving LST from hyperspectral TIR data include the following aspects:

(1) The difficulty of atmospheric correction. Most of the atmospheric correction methods

are designed for airborne hyperspectral TIR data. The atmospheric correction methods for space-borne TIR data require the extra atmospheric profile data. Efficient atmospheric correction methods for space-borne hyperspectral TIR data using only the satellite TIR data are required to be developed.

(2) The difficulty of simultaneously retrieving LST, LSE and atmospheric profile. Current methods for simultaneously retrieving atmospheric profile, LST and LSE are complex and require the support of fast atmospheric radiative transfer model, therefore they are difficult to be applied to satellite data. Efficient atmospheric radiative transfer model are in urgent demand. Moreover, the performance of the physical methods for simultaneously retrieving atmospheric profile, LST and LSE are not stable.

(3) The difficulty of validation of retrieved results. The spatial resolutions of spaceborne hyperspectral TIR sensors are low with a resolution of 12 km for IASI and a resolution of 13.5 km for AIRS. The LST retrieved from hyperspectral TIR data are cross validated by using other sensor's LST product as a reference. However, the error in the validated LST products itself, the uncertainty of spatial registration and the temporal discrepancy between the two LST products degrade the performance of this validation. The radiance-based validation methods require known LSE and known atmospheric profile. The above shortcomings make these validation methods difficult to be applied to heterogeneous surfaces. It is required to develop methods for accurately validating the retrieved LST.

3.3.2 Drawbacks of current methods for unmixing temperatures from high spatial resolution TIR data

To retrieving component temperatures and component abundances from high spatial resolution TIR images is an ill-posed problem. The difficulties for unmixing component temperatures from high spatial resolution TIR data include following aspects:

(1) The difficulty of unmixing temperatures over heterogeneous surfaces with large variation of component temperatures. The current physics-based TUM method for high spatial resolution TIR images requires an assumption that the variation of component temperature is small, the assumption is not always correct for heterogeneous surfaces.

(2) The difficulty of unmixing temperatures over rough surfaces. Most of the current TUM methods for high spatial resolution TIR data don't take nonlinear factors such as the conductance and horizontal advection into consideration. The roughness of urban surface is not negligible for TIR radiance data with high spatial resolution.

(3) The difficulty of determination of the number of components. The TUM methods for

high spatial resolution TIR data still have large error for mixed pixels containing more than two components.

4 Data collection, data pre-processing and model

4.1 Research areas

4.1.1 Research area for retrieving LST for high emissivity surfaces from hyperspectral TIR data

The first research area for this study is the Mediterranean Sea which has a latitude ranging from 30 ºN to 43 ºN and has a longitude ranging from 12 ºE to 32 ºE (Figure 4.1). The Mediterranean Sea is in the middle latitude region; the sky over this area is frequently clear. This area was utilized to map the error of LST retrieved by the proposed multi-channel method for high emissivity surfaces from the Metop-A/IASI data.

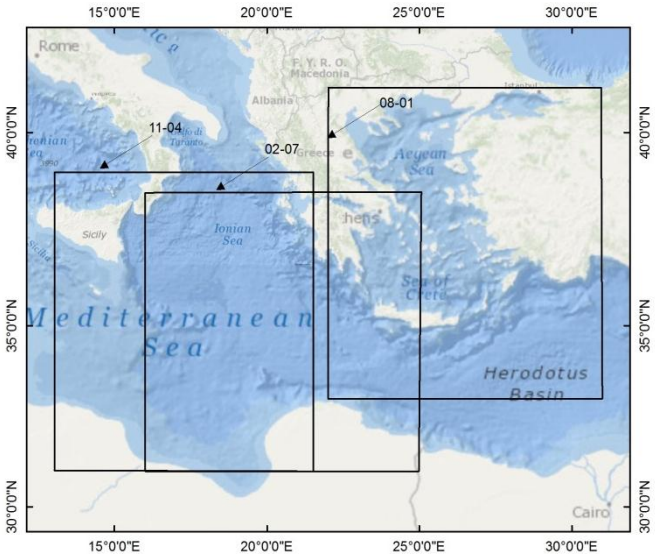

Figure 4.1 The Mediterranean Sea area used for mapping the error of the LST retrieved by the multi-channel method from Metop-A IASI data.

4.1.2 Research area for retrieving LST for natural land surfaces from hyperspectral TIR data

IASI data and radiosonde data from NOAA/Earth System Research Laboratory (ESRL) database over Australia in April and August 2014 were collected for evaluating the proposed LST retrieval method for natural land surfaces. The Australia has latitude ranging from 43 ℃S to 0 ℃N and has longitude ranging from 112 ℃E to 152 ℃E (Figure 4.2). The reason for selecting the area is that the time of Metop-A/IASI data measured over Australia in the morning is close to the time of the ESRL radiosonde data measured in this area.

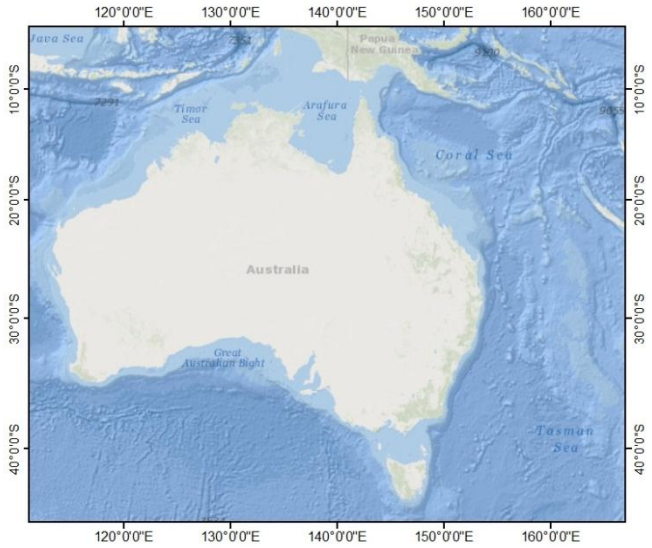

Figure 4.2 The Australia area used for collecting data for evaluating the LST retrieved by the proposed multi-channel method from Metop-A IASI data.

4.2 Satellite data and related data

4.2.1 IASI data

4.2.1.1 Metop-A/IASI sensor

With the development of hyperspectral TIR sensor, various spaceborne hyperspectral TIR data is available. AIRS equipped on the Earth Observing System (EOS)/Aqua is the first successful spaceborne hyperspectral TIR sensor which was launched in May 2002. After that, IASI equipped on Metop-A satellite was launched in June 2006 and CrIS on Suomi-NPP

satellite was launched in October 2011. The characteristics of these spaceborne hyperspectral TIR sensors are listed in Table 4.1.

Table 4.1 The characteristics of the main on-orbit hyperspectral TIR sensors

Sensor Name	Light splitting method	Spectral region(μm)	Spectral Resolution (cm^{-1})	Spatial resolution at nadir	Radiometric Noise
AIRS	Grating spectrometer	8.80 -15.4 6.20 -8.22 3.74 -4.61	0.55 1.2 2	13	0.15-0.35(280K)
IASI	Interferometer	3.62 -15.5	0.5	12	0.20-0.35(280K)
CrIS	Interferometer	9.13 -15.38 5.71 -8.62 3.92 -4.65	0.625 1.25 2.5	14	0.10-0.50(280K)

Up to now, IASI is the most accurate thermal infrared sounding interferometer (Chalon et al. 2001; Simeoni et al. 2004). The expected accuracy for atmospheric temperature profile and surface temperature retrieved from Metop-A/IASI is 1 K, and that for atmospheric moisture profile is 10%. IASI on the polar-orbiting meteorological satellite Metop-A equipped on the space-borne hyperspectral TIR sensor was utilized for this study.

IASI has 8461 continuous channels centered in the spectral interval of 645 $cm^{-1}$to 2760 cm^{-1} (Hilton et al. 2012). The spectral sampling frequency for the IASI is 0.25 cm^{-1}, respectively. The scanning angle of IASI is 48 ?20 ´. IASI scans the Mediterranean area in mid-morning orbit every day. The major spectral characteristics of IASI are shown in Table 4.2. The radiant noise of main IASI channels in noise equivalent differential temperature at a temperature of 280 K is shown in Table 4.3. The radiant noise of IASI channel i at a temperature of Tb' is calculated by the following equation

$$NE\Delta T_{Tb'}(\nu) = \frac{\frac{\partial B(Tb=280,\nu)}{\partial Tb}}{\frac{\partial B(Tb=Tb',\nu)}{\partial Tb}} NE\Delta T_{280}(\nu) \quad , \tag{4.1}$$

where $NE\Delta T_{280}(\nu)$ is the radiant noise of channel i in noise equivalent differential temperature for a temperature of 280 K;

ν is central wavenumber of a channel i;

$NE\Delta T_{Tb'}(\nu)$ is the the radiant noise of channel i in noise equivalent differential temperature for a temperature of Tb'.

Table 4.2 The main spectral region used by Metop-A/IASI

Name	Spectral region	Application of IASI
R1	650 to 770 cm^{-1}	Temperature profile
R2	790 to 980 cm^{-1}	Surface and cloud properties
R3	1000 to 1070 cm^{-1}	O_3 sounding
R4	1080 to 1150 cm^{-1}	Surface and cloud properties
R5	1210 to 1650 cm^{-1}	Humidity profile CH_4 and N_2O column amount
R6	2100 to 2150 cm^{-1}	CO column amount
R7	2150 to 2250 cm^{-1}	Temperature profile N_2O column amount
R8	2350 to 2420 cm^{-1}	Temperature profile
R9	2420 to 2700 cm^{-1}	Surface and cloud properties
R10	2700 to 2760 cm^{-1}	CH_4 column amount

Table 4.3 The radiative noise of IASI channels in noise equivalent differential temperature (NEΔT) at a temperature of 280 K

Wavenumber (cm^{-1})	NEΔT (K)	Wavenumber (cm^{-1})	NEΔT (K)	Wavenumber (cm^{-1})	NEΔT (K)	Wavenumber (cm^{-1})	NEΔT (K)
650	0.419	1200	0.095	1750	0.170	2300	0.239
700	0.157	1250	0.096	1800	0.200	2350	0.287
750	0.145	1300	0.098	1850	0.224	2400	0.351
800	0.145	1350	0.100	1900	0.250	2450	0.400
850	0.150	1400	0.105	1950	0.240	2500	0.700
900	0.150	1450	0.105	2000	0.130	2550	0.900
950	0.165	1500	0.111	2050	0.135	2600	1.100
1000	0.165	1550	0.116	2100	0.141	2650	1.300
1050	0.176	1600	0.125	2150	0.151	2700	1.600
1100	0.200	1650	0.137	2200	0.172	2750	1.935
1150	0.200	1700	0.160	2250	0.200		

IASI is an optical mechanical scanning system, which scans the earth surface in a direction perpendicular to the satellite orbit track step by step with scanning angle of ±48°20. Each scanning in measurement track includes 30 views in the ground direction which are the so-called Effective Field Of Views (EFOVs). Each EFOV contains 2×2 Instantaneous Field Of Views (IFOVs) as shown in Figure 4.3. The diameter of each IFOV is 14.65 mrad which

corresponds to a circular pixel of 12 km diameter at sub-satellite point.

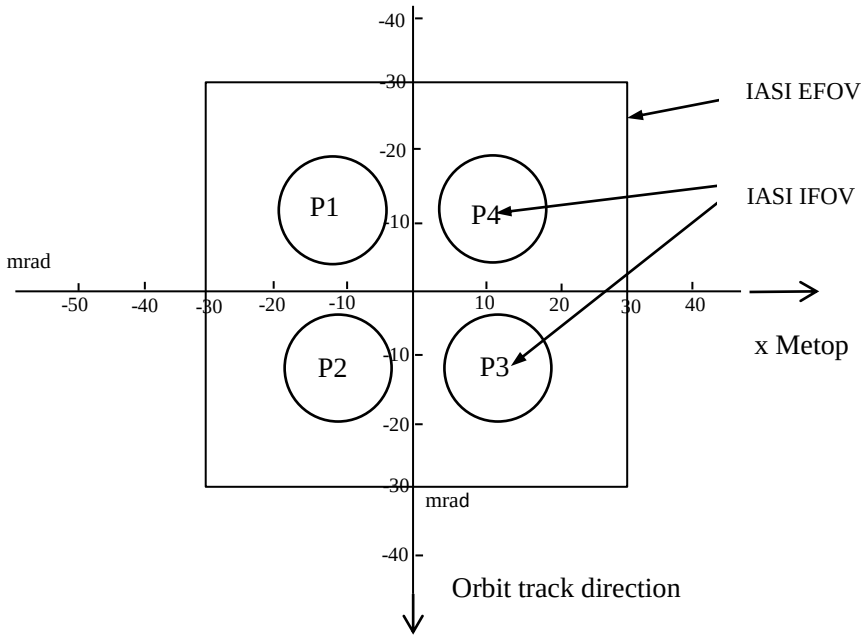

Figure 4.3 Illustration of IASI IFOV

4.2.1.2 Metop-A/IASI data products

Metop-A/IASI data products consist of five types of products from Level 0 to Level 4. Level 0 product is raw IASI radiance data which includes spectra without calibration. Level 1 A product consists of spectra without apodization. Processing in this step comprises decoding, spectral calibration and radiometric post-calibration. Level 1B product consists of spectra which are derived by spectral resampling. Level 1C product consists of spectra derived after apodization. Level 2A products are products derived from IASI data which includes the atmospheric temperature and moisture profile, spatial distribution of atmospheric trace gases, LST and cloud parameters. Level 2B products are land surface products derived from the combination of IASI data and data of other sensors on Metop-A, and are generally more accurate and have higher spatial resolution. Level 3 products are spatially and temporally averaged land surface products. Level 4 are products derived from multi-satellite data. Metop/IASI products are created by the EUMETSAT Polar System Core Ground Segement, located in EUMETSAT headquarters at Darmstadt Germany, and also in eight decentralized Satellite Application Facilities (SAF), hosted by other EUMETSAT Member States.

The Level 1C product not only contains radiance spectra, but also contains information about observing angle, time and geolocation. Metop-A/IASI Level 1C data product in the first weeks of Feb, August and November 2014 over the Mediterranean Sea research area was collected to evaluate the accuracy of the proposed multichannel method for high emissivity

surfaces. More details about the Level 1C data can be found in IASI Level 1 product guide (http://www.eumetsat.int/website/wcm/idc/idcplg?IdcService=GET_FILE&dDocName=pdf_iasi_level_1_prod_guide&RevisionSelectionMethod=LatestReleased&Rendition=Web).

Metop-A/IASI Level 2A LST product was also used in this study. The IASI LST product includes cloud fraction and LST product. The LST product is retrieved from clear-sky IASI Leve1C radiances by the EOF linear regression method (Zhou et al. 2011). The cloud fractions are retrieved by the CO_2-slicing method (Menzel et al. 1983; Smith and Frey 1990). The cloud fractions in the IASI LST product varies from 0 to 100%: 0 signifying no cloud, 0.1%-99.9% signifying small cloud, 100% signifying full of cloud. The accuracy of the cloud fractions and the LST product is 10% and 2 K. The IASI LST product and cloud fraction data in April and August 2012 over Australia was collected to evaluate the accuracy of the LST retrieved by the proposed multi-channel method over natural land surfaces.

4.2.2 Metop-A/AVHRR SST product

AVHRR on Metop-A has six channels centered in the visible - near infrared region and in the TIR region. The spatial resolution of the Metop-A/AVHRR data at nadir in TIR region is 1 km. The spectral characteristics of the AVHRR channels in TIR region are shown in Table 4.4. The instrumental spectral response functions for the two TIR channels of Metop-A/AVHRR data are depicted in Figure 4.4.

The SST product from Metop-A/AVHRR is retrieved by the SW method (Le Borgne et al. 2007) The AVHRR SST product is available from the OSA-SAF since 2007. The Metop/AVHRR product with spatial resolution of 1.0 km in satellite projection was used in this study. This SST product includes SST, cloud information and quality information. The standard error (absolute mean error + standard deviation of error) of the daytime Metop/AVHRR SST product is 0.5 K and the standard error of the nighttime Metop/AVHRR SST product is 0.66 K. The Metop/AVHRR SST product over Mediterranean Sea in the first weeks of February, August, and November, 2014 was collected for this study. The Metop-A/AVHRR SST product was taken as a reference to evaluate the LST retrieved by the proposed multi-channel method for high emissivity surfaces from Metop-A/IASI data.

Table 4.4 The main radiant and spectral characteristics of Metop-A/AVHRR

No. of channel	Wavelength (μm)	NEΔT at 300K (K)	Applications
4	10.3-11.3	<0.12 K, 0.20 mW/(m2 sr cm-1)	Day/night cloud and surface temperature mapping
5	11.5-12.5	<0.12K, 0.21 mW/(m^2 sr cm^{-1})	Cloud and surface temperature, Day/night cloud mapping

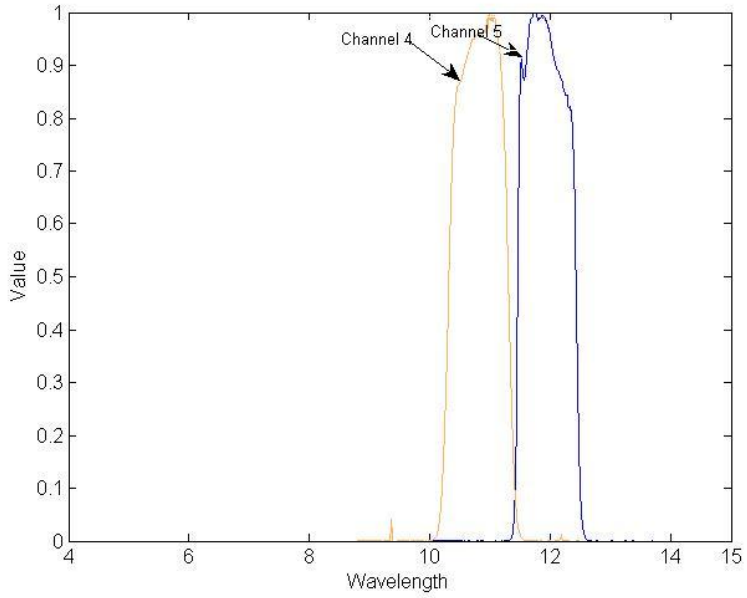

Figure 4.4 The instrumental spectral response functions of AVHRR TIR channels

4.2.3 The MOD11B1 LSE product

The MOD11B1 v5 LSE product has daily LSE data produced using the day/night LST retrieval algorithm from MODIS/Terra data (Wan and Li 1997a). The MOD11B1 LSE product has bands 20, 22, 23, 29, 31, 32 centered at 3.7μm, 3.9 μm, 8.6 μm, 11 μm and 12 μm with spatial resolution of 6 km. The MOD11B1 LSE product is available since March 2000. The MOD11B1 LSE product covers the Australia at midnight daily. The MOD11B1 LSE product was used to evaluate the proposed multi-channel method for natural land surfaces.

4.2.4 TIGR Atmospheric profile database

Atmospheric profile data from the Thermodynamic Initial Guess Retrieval (TIGR)

database consists of atmospheric moisture, temperature and ozone profile data (Chedin et al. 1985; Chevallier et al. 1998). Each TIGR atmospheric profile is measured at 40 pressure layers (between 0.05 hPa and 1013 hPa). The 2311 atmospheric profiles in the TIGR 2002 v1.1 database, which are selected from approximately 80000 atmospheric profiles measured by the radiosondes over the global, represent typical atmospheric situations from polar to tropical atmosphere: the profiles with numbers from 1 to 872 denote the Tropical atmospheric profiles, those with numbers from 873 to 1260 denote the first type Middle latitude atmospheric profiles, those with numbers from the 1261 to 1614 denote the second type Middle latitude atmospheric profiles, those with numbers from 1617 to 1718 denote the first type Polar atmospheric profiles, those with numbers from 1719 to 2311 denote the second type Polar atmospheric profiles. The TIGR 2000 v1.1 database is provided by the Atmospheric Radiation Analysis Group (http://ara.abct.lmd.polytechnique.fr/index.php?page=tigr). In this study, the TIGR atmospheric profile data was utilized to develop the proposed multi-channel method for retrieving LST from hyperspectral TIR data for high emissivity surfaces and to extend the proposed multi-channel to natural land surfaces. The 40 pressure layers of each TIGR atmospheric profile are shown in Table 4.5.

Table 4.5 The 40 pressure layers of each TIGR atmospheric profile

0.05	0.09	0.17	0.30	0.55	1.00	1.50	2.23
3.33	4.98	7.43	11.11	16.60	24.79	37.04	45.73
56.46	69.71	86.07	106.27	131.20	161.99	200.00	222.65
247.87	275.95	307.20	341.99	380.73	423.85	471.86	525.00
584.80	651.04	724.78	800.00	848.69	900.33	955.12	1013.00

4.2.5 NOAA/ESRL atmospheric profile database

Atmospheric profile data from NOAA/Earth System Research Laboratory (ESRL) database consists of atmospheric dewpoint temperature and temperature profile (http://esrl.noaa.gov/raobs/General_Information.html). Each dewpoint temperature profile and temperature profile have data measured at 15-20 pressure layers. The pressure layers for atmospheric dewpoint temperature profile and for atmospheric temperature profile are between 5 hPa and 1014 hPa. The atmospheric profile data are measured by the radiosonde which is generally launched twice a day (at 0:00 and 12:00 UTC time) at global radiosonde sites. The NOAA/ERSL atmospheric profile data in April, November 2016 over Australia was

collected to evaluate the accuracy of the proposed multi-channel method for natural land surfaces. The spatial distribution of the radiosonde sites over Australia is shown in Figure 4.5. A dewpoint temperature profile and an atmospheric temperature profile from NOAA/ESRL database are shown in Figure 4.6.

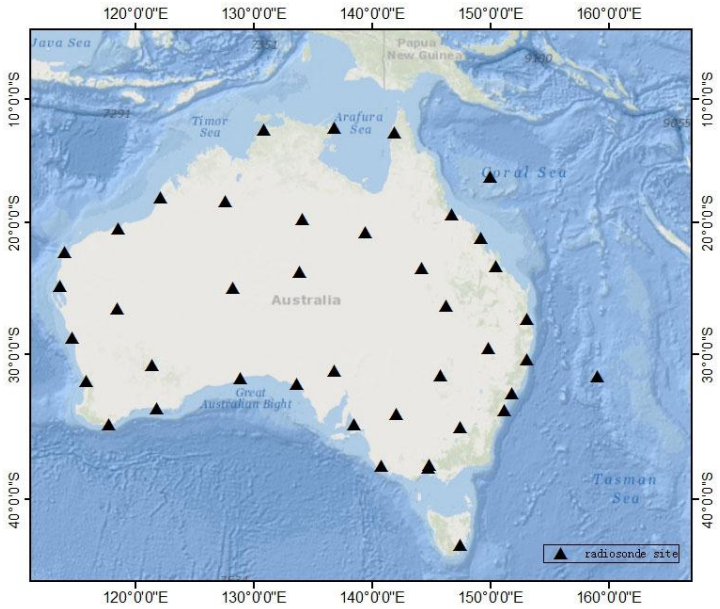

Figure 4.5 The spatial distribution of radiosonde sites for the selected NOAA/ESRL atmospheric profile data

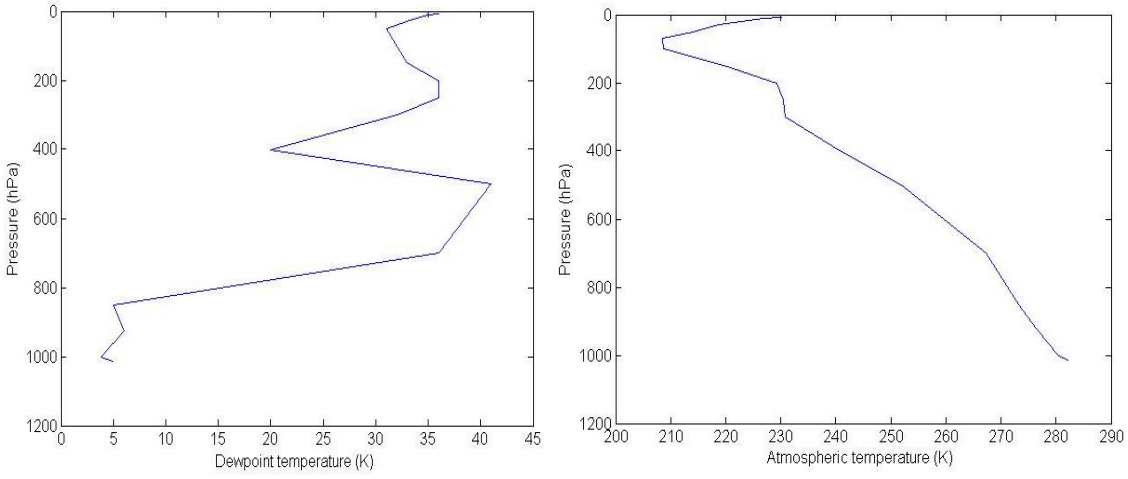

(a) (b)

Figure 4.6 A typical NOAA/ESRL atmospheric dewpoint temperature (a) and temperature (b) profile

4.2.6 ASTER emissivity library

The ASTER emissivity library includes data from three emissivity libraries: the Johns Hopkins University (JHU) spectral library, the Jet Propulsion Laboratory (JPL) spectral library, and the United States Geological Survey (USGS - Reston) spectral library. The ASTER emissivity library consists of LSE information of soils, rocks, vegetations, water bodies, minerals, meterorites and manmade materials (Salisbury et al. 1994). The merit of the spectrums in ASTER emissivity library is that they have wide spectral interval which covers the visible and infrared region and they have continuous measurements in the whole spectral interval.

Specially, the measurements in JHU spectral library, which provides most of spectrums for this study, include two types of spectrums: the bi-directional reflectance spectrum and the directional hemispheric reflectance spectrum. The measurements of minerals and meterorites in JHU are bi-directional reflectance spectra with spectral interval from 2.05 μm to 25 μm. For other materials the measurements are directional hemispheric reflectance spectra. The directional hemispheric reflectance spectra have a spectral interval of 0.4 μm – 15 μm and consist of two parts of spectra: the spectra covering region from the visible to short-wave infrared region, and the spectra covering the region from short-wave infrared region to thermal infrared region. The directional hemispheric reflectance of these materials in the MIR and TIR region is measured with a Transformed Infrared spectrometer and an integration sphere. The measurements of directional hemispheric reflectance are converted to directional hemispheric emissivity using the Kirchoff's law: $\varepsilon = 1 - \rho$. The latter part of spectra of the directional hemispheric reflectance is measured with the Nicolet FTIR spectrometer and the error of the Nicolet FTIR is within 1%. The ASTER LSE data was used to extending the proposed multi-channel method to natural land surfaces in this study. The emissivity spectra used in this study from ASTER emissivity library are shown in Figure 4.7.

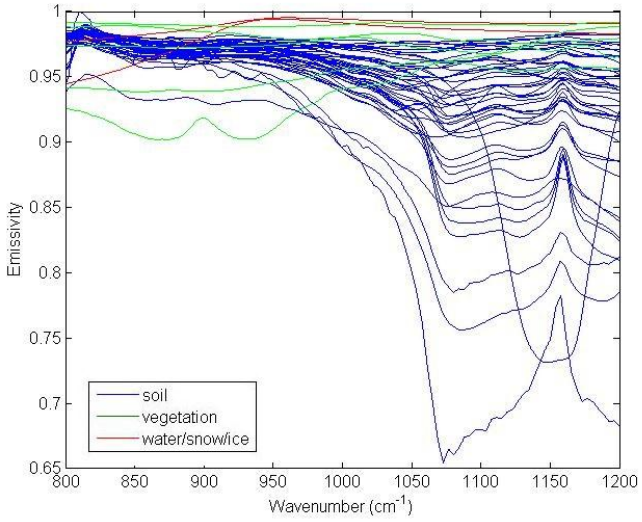

Figure 4.7 The emissivities of soils, vegetations, water bodies selected from ASTER emissivity library and the emissivity of fresh leaf from the MODIS UCSB emissivity library

4.2.7 MODIS UCSB emissivity library

This data set contains emissivity spectrums of different manmade and natural materials, collected by Zhengming Wan at the institute for Computational Earth System Science at the University of California, Santa Barbara (USCB; http://www.icess,ucsb.edu/modis/EMIS/htm-1/em.html). The wavenumber of the emissivity spectrums in this data set is between 3.5 μm and 14.0 μm. With emissivity spectrums of various vegetations, this data set supplements the ASTER emissivity library. In this study, we selected a LSE spectrum of fresh leaf, which has mean emissivity value less than 0.95 in spectral interval of [800 cm^{-1}, 950 cm^{-1}], to extend the proposed multi-channel method to natural land surfaces (shown in Figure 4.7).

4.2.8 Urban surface emissivities and urban surface temperatures

These urban surface emissivities and urban surface temperatures are measured during the Detection in Urban scenario using Combined Airborne imaging Sensors (DUCAS) campaign (Renhorn et al. 2013). The wavenumber of the LSE spectrums are between 833 cm^{-1} and 1428 cm^{-1}. The materials in the urban surface emissivity data and urban surface temperature data are grass, gravel roof and asphalt roof. The LSE spectrums and the urban surface temperatures were utilized to simulate IASI data to evaluate the proposed physics-based unmixing method mentioned above. The urban emissivity data is shown in Figure 4.8.

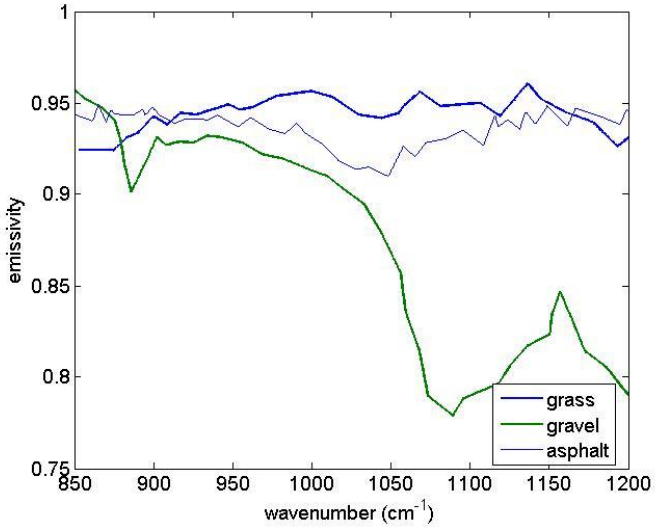

Figure 4.8 The emissivity spectrums of urban materials adopted from the literature (Cubero-Castan et al. 2015)

4.3 Data pre-processing

ESRL atmospheric dewpoint temperature profile data is converted to total precipitable water vapor column data using an equation mentioned in (Lawrence 2005) and an equation extracted from MODTRAN code. Given the atmospheric dewpoint temperature and temperature profile, the atmospheric moisture profile is computed by

$$\vec{H} = \exp\left(\frac{-A_1 \cdot \vec{T} \cdot (B_1 + \vec{T_d}) \,/\, (B_1 + \vec{T}) + \vec{T_d} \cdot A_1}{B_1 + \vec{T_d}}\right) \cdot 100 \qquad (4.2)$$

where $\vec{H}$ is relative humidity profile;

A_1 and B_1 are the coefficients: A_1=17.625, B_1=243.04 ℃;

$\vec{T_d}$ Td is the dew point temperature profile in Kelvin;

$\vec{T}$ is the atmospheric temperature profile in degree Celsius;

With atmospheric moisture profile, pressure profile, and temperature profile, mixing ratio profile of atmospheric water vapor is expressed as

$$\vec{r} = \frac{\vec{H} \cdot N_A \cdot \exp[18.9766 - 14.9595 \cdot \frac{273.15}{\vec{T}} - 2.43882 \cdot (\frac{273.15}{\vec{T}})^2]}{10^8 \cdot n_0 \cdot m_{air} \cdot (\frac{\vec{p}}{1013.25})} \cdot 100 \qquad (4.3)$$

where $\vec{r}$ is mixing ratio profile of atmospheric water vapor in g/g;

$\vec{p}$ is the atmospheric pressure profile in hPa;

$\vec{T}$ is the atmospheric temperature profile in K;

n_0 is the Loschmidt coefficient in (number of molecules) /cm^{-3} n_0 =2.6867774$\times 10^{19}$;

m_{air} is the average molecular weight of the air: m_{air} =28.964 g/mole;

N_A is the Avogadro coefficient: N_A =6.02214179 $\times 10^{23}$.

With atmospheric moisture profile in the format of mixing ratio and atmospheric pressure profile, atmospheric total precipitable water vapor column is written as

$$wv = \frac{\frac{(r_{1:n-1}+r_{2:n})}{2}\cdot(p_{2:n}-p_{1:n-1})}{1000+\frac{(r_{1:n-1}+r_{2:n})}{2}}\cdot\frac{1}{9.80665}\cdot 10 \tag{4.4}$$

$$WV = \sum_{i=1:n-1} wv_i$$

where **wv** is the precipitable water vapor profile in g/cm^2;

wv_i is the precipitable water vapor content at pressure layer i (i=[1:n-1]) in g/cm^2;

$p_{2:n}$ is atmospheric pressure profile measured from the 2nd pressure layer to nth pressure layer in hPa;

$p_{1:n-1}$ is the atmospheric pressure profile measured from the 1st pressure layer to the n-1th pressure layer in hPa;

$r_{1:n-1}$ is the mixing ratio profile of atmospheric water vapor measured from the first pressure layer to the n-1th pressure layer in g/kg;

$r_{2:n}$ is the mixing ratio profile of atmospheric water vapor measured from the 2nd pressure layer to the nth pressure layer in g/kg;

WV is the total precipitable water vapor content column in g/cm^2.

4.4 Atmospheric radiative transfer model

4A/OP is a line-by-line model. It relies on an optical thickness database, which is created in advance, to perform fast simulation of the radiative transfer. 4A/OP supports simulation of radiance spectrum in the infrared region; the usual spectral domain is between 600 and 3000 cm^{-1}. It can be used for various atmospheric and land surface conditions. Spectra with high spectral resolution can be computed by 4A/OP (the normal spectral resolution is 5·10^{-4}). Users can simulate spectra with different spectral resolutions using various types of instrumental functions. The newest version of the model allows simulation of the scattering of aerosol. Partial derivatives of the radiances with respect to the temperature and gas mixing ratio can also be computed.

The scheme of the 4A/OP is shown in Figure 4.9. The core code of the 4A/OP uses the

optic thickness in atlases, the reference thermodynamic parameters, default gas mixing ratio, atmospheric profiles, simulation definition parameters and instrumental spectral response functions as inputs. Optical thickness in atlases, reference thermodynamic parameters, and default gas mixing ratio are fixed input parameters. Atmospheric profiles, land surface emissivity, instrumental spectral response functions, simulation definition parameters are user-defined input parameters. The output parameters include radiance spectra, atmospheric transmittance spectra, and partial derivatives of radiance with respect to temperature and gas mixing ratio. Detailed instruction of the 4A/OP can be seen in (Chaumat et al. 2009). 4A/OP was used to simulate Metop-A/IASI data in this study.

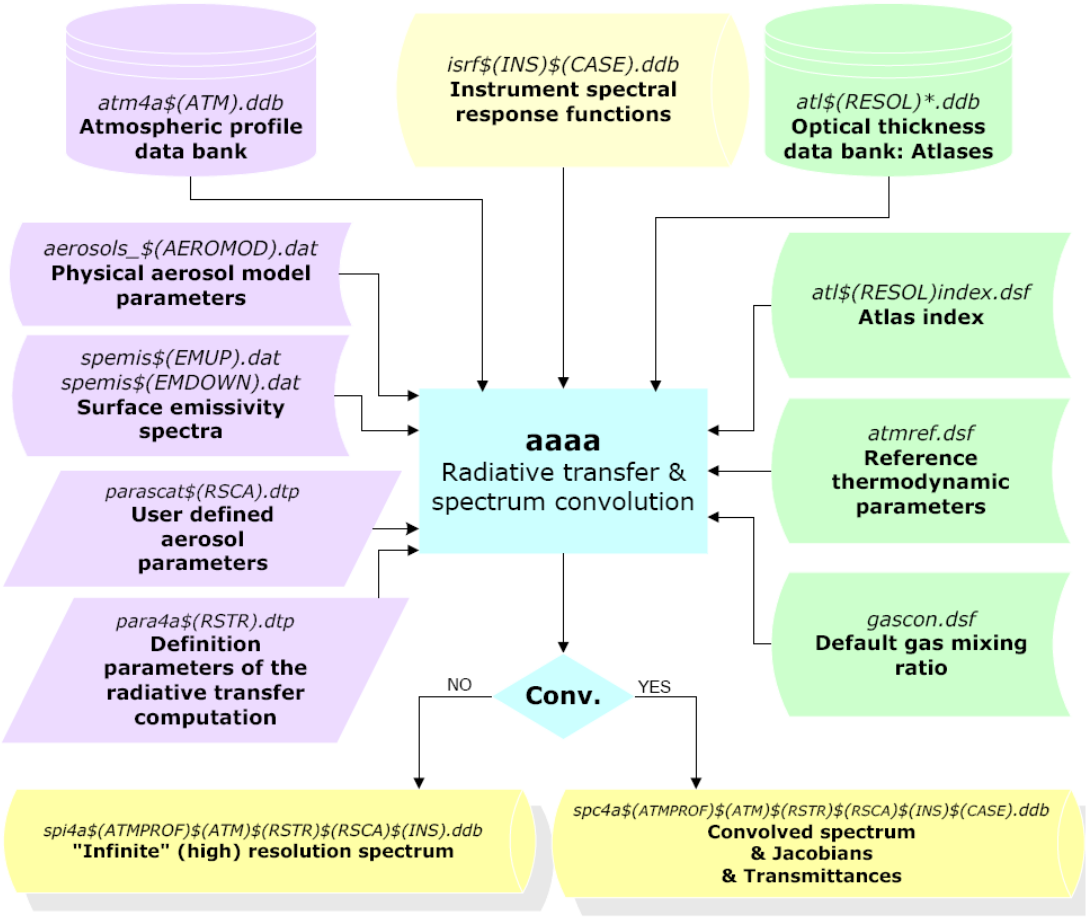

Figure 4.9 Scheme of 4A/OP (Chaumat et al. 2009)

5 Retrieving LST for high emissivity surfaces from hyperspectral TIR data using a muli-channel method

5.1 Introduction

LST is a key parameter in climate systems. Hyperspectral TIR sensors with thousands of channels provide new way to retrieve LST from space.

Various methods exist to retrieve LST from space-borne hyperspectral TIR data: the principal component regression method (Zhou et al. 2002; Schlussel and Goldberg 2002; Goldberg et al. 2003; Weisz et al. 2007; Zhou et al. 2011), the ANN method (Aires et al. 2002a; Wang et al. 2013a), the stepwise LST and LSE retrieval method (Pequignot et al. 2008), the simultaneous LST and LSE retrieval method (Susskind et al. 2003; Paul et al. 2012), the physical simultaneous atmospheric profiles, LST and LSE retrieval method (Rodgers 1976; Li et al. 2007; Masiello and Serio 2013). These methods cannot be used for retrieving LST from hyperperspectral TIR data containing damaged data at certain channels. The objective of this study is to develop a multi-channel method for retrieving LST for high emissivity surfaces (surfaces of dense vegetation areas, surfaces of water areas) from space-borne Hyperspectral TIR data.

5.2 Physical basis of the multi-channel method

Assuming that the land surface is a black body, the radiance at TOA at a hyperspectral TIR channel R_i can be written as

$$R_i = B_i(T_s)\tau_i + R_{at\uparrow i} \tag{5.1}$$

where $B_i(T_s)$ is the surface radiance at a channel i with a surface temperature of T_s, $R_{at\uparrow i}$ is the upwelling radiance emitted by the atmosphere, and τ_i is the atmospheric transmittance.

If equation 5.1 is linearized around LST, equation 5.1 can be rewritten as

$$T_i = \tau_i T_s + (1-\tau_i) Ta_i, 1 \le i \le p \quad (5.2)$$

where T_i is the brightness temperature at TOA at channel i, Ta_i is the equivalent atmospheric temperature at channel i, τ_i is the transmittance at channel i, and p is the number of channels selected for retrieving LST.

Inspired by the SW method for LST retrieval, we propose a multi-channel method for retrieving LST for high emissivity surfaces from hyperspectral TIR data. In this method, LST can be written as

$$T_s = w_0 + \sum_{i=1:p} w_i T_i \quad (5.3)$$

where w_i are regression coefficients. The number of channels is p, and the centre wavenumbers at channel i (i=[1,p]), and coefficients w_i (i=[0,p]) can be determined using stepwise regression with simulation data.

5.3 Determination of the coefficients w_i and the central wavenumbers

5.3.1 Data for simulation

Although there are large amounts of hyperspectral TIR data measured at TOA, it is still difficult to find spatially and temporally collocated atmospheric moisture and temperature profile data. Additionally, there are few field-measured LST data at the spatial scale of a satellite IFOV (12 km for IASI). Therefore, we have resorted to synthetic method for determining the parameters in equation 5.3.

We selected typical profiles from the TIGR database for simulation (Chedin et al. 1985; Chevallier et al. 1998) in two steps. First, we classified the 946 clear-sky TIGR profiles into six groups according the concentration of water vapour. The method for determining the clear-sky atmospheric situations are detailed by (Galve et al. 2008). The total precipitable water-vapour ranges of the six groups are between 0 and 1 g/cm^2, between 1 and 2 g/cm^2, between 2 and 3 g/cm^2, between 3 and 4 g/cm^2, between 4 to 5 g/cm^2, and between 5 and 6 g/cm^2, respectively. After that, we randomly selected nearly 23 profiles from each group to make sure the selected profiles were representative. The air mass types for the selected atmospheric profiles are tropical, temperate, cold temperate and summer polar, cold polar, and winter polar types. The total precipitable water vapours of the selected atmospheric profiles range from 0 g/cm^2 to 6 g/cm^2. The bottom atmospheric temperatures of the selected

atmospheric profiles range from 230 K to 320 K. The variation of bottom temperature with the total precipitable water vapour for the 139 selected atmospheric profiles is presented in Figure 5.1.

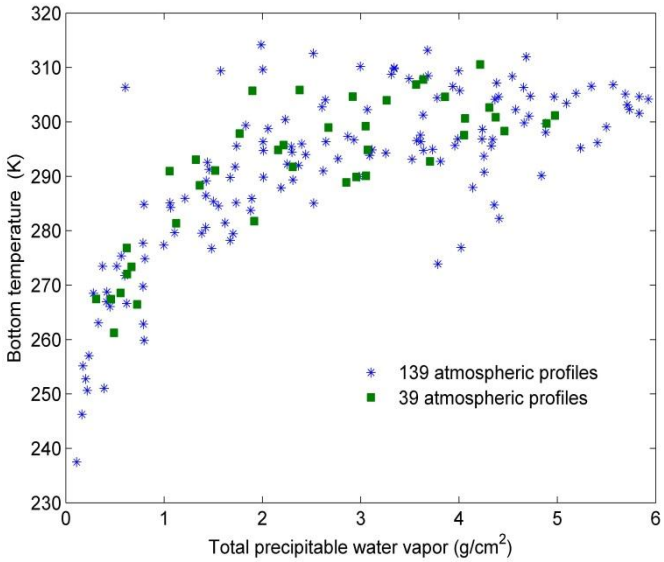

Figure 5.1 The bottom temperatures as a function of the total precipitable water vapour for the 139 atmospheric profiles and other 39 atmospheric profiles.

To describe the rapid variation of LST for each profile, the six LSTs for simulation are sums of bottom atmospheric temperature (Ta0) and one out of six perturbations. The six perturbations are [-15 K, -5 K, 0 K, 5 K, 10 K, and 15 K] when Ta0 <280K, and these perturbations are [-10 K, -5 K, 0 K, 5 K, 10 K, and 20 K] when Ta0 ≥280K (Wang et al. 2013a).

5.3.2 Procedures for determining the central wavenumbers and the coefficients w_i

We used the stepwise regression method with the simulation data to determine the centre wavenumbers at channel i and coefficients w_i in equation 5.3 for IASI. The procedures are shown in Figure 5.2.

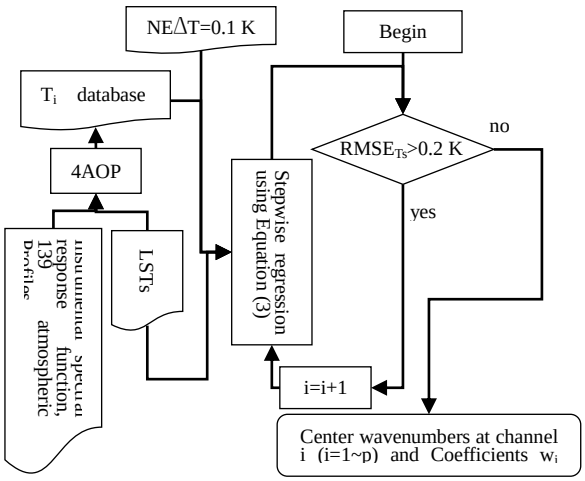

Figure 5.2 The scheme for determining the centre wavenumbers of channel i (i=[1,p]) and the coefficients w_i (i=[0,p]).

For this study, we have simulated large IASI data using 4A/OP with the data mentioned in Section 5.3.1. The flowchart for simulating hyperspectral brightness temperature data at TOA is shown in Figure 5.3. The 4A/OP is used to simulate atmospheric transmittance and upward radiance using atmospheric profile data. Brightness temperature database is calculated using the radiative transfer equation with output atmospheric radiative terms of 4A/OP. The spectral interval and spectral sampling frequency for simulation are 800 - 1200 cm^{-1} and 0.25 cm^{-1}, respectively. The viewing angle for simulation is restricted to nadir observation. For each simulation case, a random noise dimension of 1601 generated by a Matlab random number generator with NEΔT of 0.1 K is added. The NEΔT has been set according to that of the IASI (Aires et al. 2002c). Because O_3 has a strong absorption feature in hyperspectral TIR radiance spectrum, only hypersepctral TIR data at channels in the spectral interval of 800-985 cm^{-1} and in the spectral interval of 1150-1200 cm^{-1} have been used for stepwise regression (Wang et al. 2009).

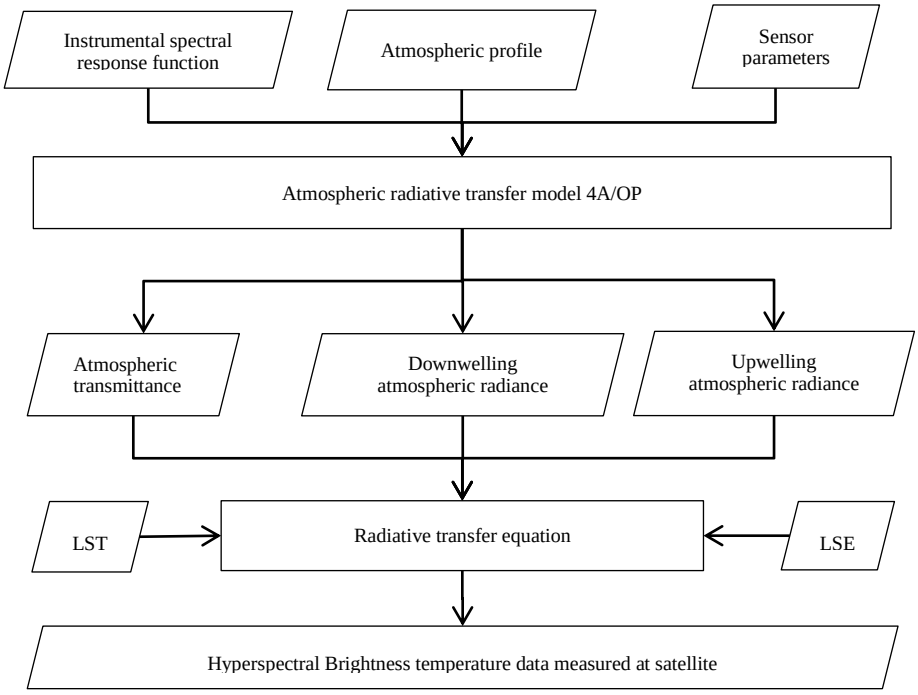

Figure 5.3 Flowchart for simulating hyperspectral brightness temperature data at satellite

The stepwise regression is used to determine the centre wavenumbers of channel i and the coefficients w_i with the simulation data above. First, the channel centred at a wavenumber of 1158.5 cm^{-1}, where transmittance is the largest, is selected as the initial channel.

In step m+1 of stepwise regression, for each remaining channel, a linear relationship fitted by the least square method is written as

$$T_s = w_0 + \sum_{i=1}^{m} w_i T_i + w_{m+1} T_{m+1} \tag{5.4}$$

where T_i (i=[1,m]) are the channel brightness temperatures determined before this step, and T_{m+1} is the brightness temperature at each remaining channel. The coefficients w_i (i=[1,m+1]) in equation 5.4 is calculated by the following equation

$$W = \left(X^T X\right)^{-1} X^T Y \tag{5.5}$$

where W is the coefficient vector of dimension m, X is hyperpsectral TIR brightness temperature n×m matrix, and Y is the LST vector of dimension n. Here, X contains n samples of the m channel hyperspectral TIR brightness temperatures. A sum of squares for partial regression (U_k) is used to calculate the contribution of T_{m+1} and is defined as

$$U_k = SS_k - SS_{-k} \tag{5.6}$$

where SS_k and SS_{-k} are the sum of the squares for regression with channel k, and without channel k, respectively. The sum of squares for regression is defined as

$$SS = \sum_{i=1}^{n} \left(w_0 + \sum_{j=1}^{l} w_0 Tb_{ij} - \bar{y} \right)^2 \tag{5.7}$$

where *l* is the number of channels and *n* is the number of simulation cases, and $\bar{y}$ is the mean of n samples of LSTs. The $m+1^{th}$ TIR brightness temperature at channel i added by the stepwise regression is the one with largest partial regression square sums among the remaining TIR brightness temperatures. We also check to see if the spectral interval of two nearby central wavenumbers is larger than 4.5 cm^{-1}. If not, TIR brightness temperature at this channel is replaced by the one with second-largest sum of squares for partial regression.

The criterion for determining the number of channels for equation 5.3 is that the root mean square error (RMSE) of the LST retrieved using equation 5.3 from the simulation data mentioned above is less than 0.2 K. The output coefficients w_i and centre wavenumbers of channel i are the solutions.

The variation of RMSE of the retrieved LST with the number of channels in the process of determining the centre wavenumbers of channel i and the coefficients w_i is shown in Figure 5.4: the error of the LST that is retrieved using the corresponding regression equation with the simulation data above decreases with the growing number of channels, and the RMSE of the retrieved LST is less than 0.2 K when the number of channels is larger than 10.

The centre wavenumbers of channel i (i=[1,p]) and the coefficients w_i are shown in Figure 5.5. From this figure, we can see that the centre wavenumbers correspond to the wavenumbers where water vapour absorption is weak. The reason may be that the assumption that LST can be expressed as a linear function of p hyperspectral TIR brightness temperatures is more reliable at these wavenumbers. Figure 5.5 also shows that all the coefficients w_i are varying in a relatively small range between: -0.80~0.80.

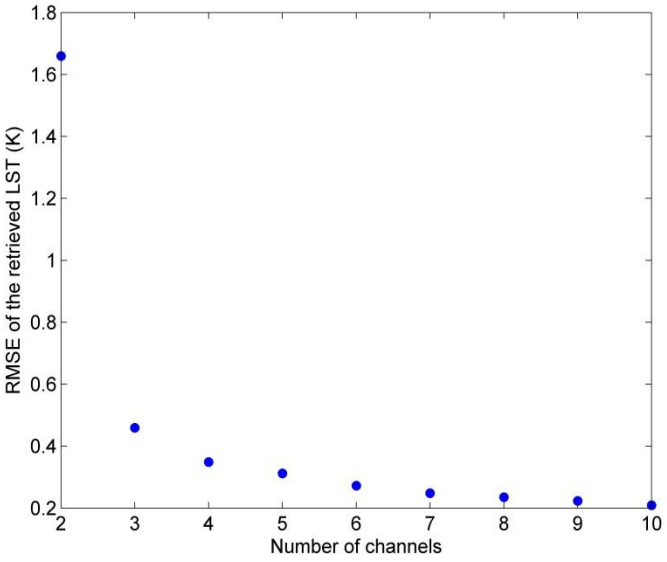

Figure 5.4 The variation of RMSE of the retrieved LST with the number of channels in the process for determination of centre wavenumbers and coefficients.

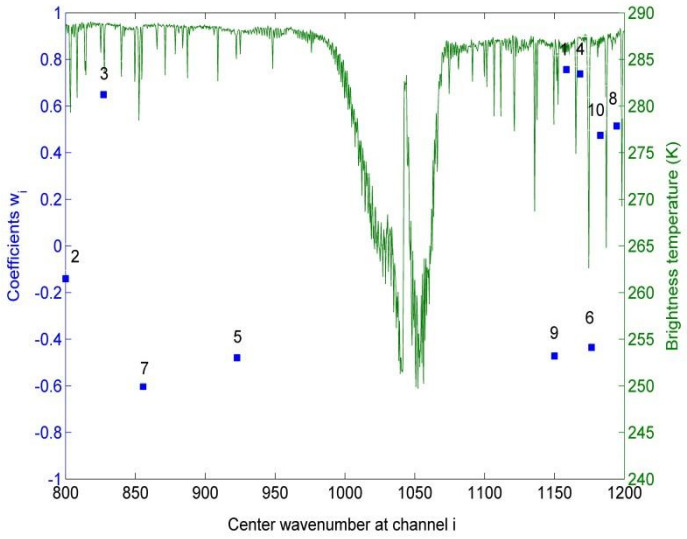

Figure 5.5 The centre wavenumbers at channel i (i=[1,p]) and coefficients w_i (i=[0,p]) superimposed on a typical IASI spectrum. (w_0=2.486; the No. above each blue square indicate the order of each channel in the determination process).

5.4 Sensitivity analysis

5.4.1 Sensitivity to spectral sampling frequency

We analysed the sensitivity of the method to spectral sampling frequency by refitting the coefficients w_i in equation 5.3 for each spectral sampling frequency, using five simulation databases and studying the error of LST retrieved using these refitted coefficients w_i from five other independent simulation databases.

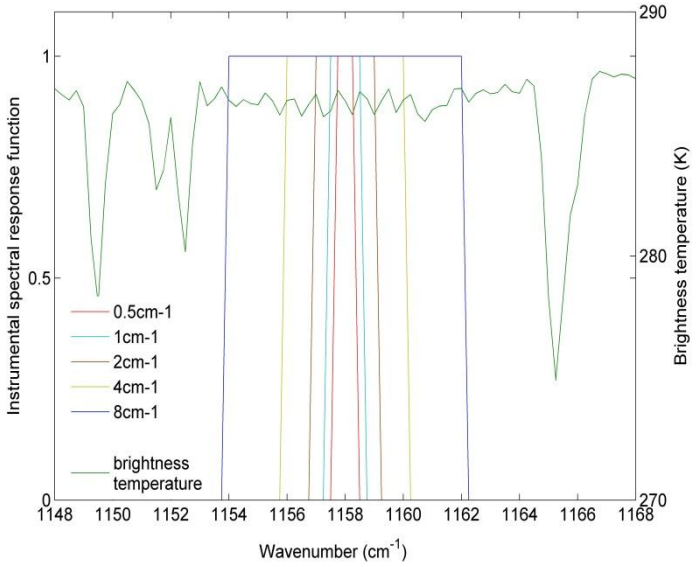

Figure 5.6 The five ISRFs at the channel with the centre wavenumber = 1158 cm^{-1} superimposed on one typical IASI spectrum in the spectral interval of 1148-1168 cm^{-1}.

To refit the coefficients w_i, we created five simulation databases for five hyperspectral TIR sensors with spectral sampling frequencies = 0.5,1,2,4,8 cm^{-1}. We assumed that the five sensors have 10 channels with the centre wavenumbers shown in Figure 5.6. The instrumental spectral response functions (ISRFs) for the five sensors are rectangular impulse functions. The ISRFs for the five sensors at one channel are shown in Figure 5.6. The simulation database for each of the five sensors is resampled from the simulation data mentioned in Section 5.3 using each ISRF. The coefficients w_i refitted for each spectral sampling frequency are shown in Table 5.1. The main spectral and radiant characteristics of the five proposed sensors are shown in Table 5.2.

Table 5.1 The coefficients w_i refitted for each spectral sampling frequency using linear regression with simulation data.

Fq* (cm^{-1})	w_0	w_1	w_2	w_3	w_4	w_5	w_6	w_7	w_8	w_9	w_{10}
0.5	-0.435	0.688	0.025	0.788	0.877	-0.535	-0.516	-0.795	0.575	-0.609	0.504
1	0.676	0.614	0.132	1.126	1.050	-0.693	-0.624	-1.170	0.586	-0.603	0.579
2	-0.372	0.738	-0.148	2.249	0.939	-2.158	-1.210	-1.339	0.953	0.259	0.720
4	-0.080	0.531	1.555	-0.102	3.360	-3.164	-1.772	0.197	0.053	0.089	0.257
8	1.083	2.833	0.931	-1.686	2.256	-1.431	-2.140	1.996	0.683	-2.549	0.102

* Fq=Spectral sampling frequency

Table 5.2 The main radiant and spectral characteristics of the five proposed sensors for analysing the sensitivity of the developed method to spectral sampling frequency

No. of the sensor	Spectral sampling frequency(cm^{-1})	Spectral interval (cm^{-1})	NEΔT (K)	Number of channels
1	0.5	800-1200	0.1K	800
2	1	800-1200	0.1K	400
3	2	800-1200	0.1K	200
4	4	800-1200	0.1K	100
5	8	800-1200	0.1K	50

To evaluate the accuracy of the LST retrieved using refitted coefficients w_i, an independent simulation database are created using the other part of TIGR atmospheric profile data (shown in Figure 5.1. in green asterisk) and resampled for each of the five hyperspectral TIR sensors using each ISRF. The other part of TIGR profiles are selected in two steps. We

classified all the remaining clear-sky TIGR profiles into five groups according to the total precipitable water vapour column, except for the 139 profiles mentioned in Section 5.3.1, and then we selected nearly 8 profiles from each of these five groups for evaluation. The total precipitable water-vapour ranges of the five groups are between 0 and 1 g/cm^2, between 1 and 2 g/cm^2, between 2 and 3 g/cm^2, between 3 and 4 g/cm^2 and between 4 and 5 g/cm, respectively. The variation of the bottom temperature with total precipitable water vapour for the 39 atmospheric profiles is represented in Figure 5.1 by green squares. The LST data and other parameters for this independent simulation are the same as those in Section 5.3. The refitted coefficients w_i and the 10 central wavenumbers determined in section 5.3 are then used for retrieving LST from these five independent simulation databases. The LST errors that were retrieved using equation 5.3 from each of the five independent simulation databases with the refitted coefficients are analysed with the spectral sampling frequencies and shown in Figure 5.7.

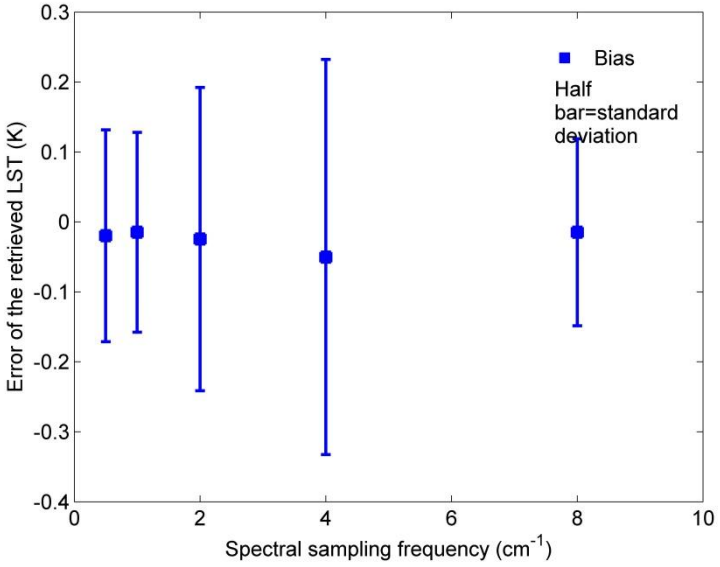

Figure 5.7 Errors of the LST retrieved by equation 4.3 using the refitted coefficients w_i from each of the five independent simulation databases as a function of spectral sampling frequency.

The coefficients w_i refitted for each spectral sampling frequency using simulation data vary significantly with spectral sampling frequencies. Therefore, we can conclude that the coefficients in equation 5.3 are dependent on spectral sampling frequency. For the five spectral sampling frequencies, the biases of the LST retrieved by equation with refitted coefficients w_i from each of the five independent simulation databases vary between -0.01 K and -0.05K, and the corresponding standard errors of the retrieved LST for each independent simulation database are less than 0.30 K. The LST can be retrieved accurately using equation

5.3 with the refitted coefficients w_i (i=[0, 10]) for each spectral sampling frequency.

5.4.2 Sensitivity to instrumental noise

To do this sensitivity analysis, three simulation databases are created by adding to noiseless IASI data noises with NEΔT = 0.1 K, 0.2 K, and 0.3 K, respectively. The noiseless IASI data is created using simulation data with the other part of TIGR atmospheric profiles, as mentioned in Section 5.4.1. For each noiseless IASI spectrum, 20 noise-added IASI spectrums are created for each level of noise, including 20 random noises with the dimension of 1,601. Each random noise is generated by the Matlab random number generator with corresponding NEΔT. The central wavenumbers at channel i and coefficients w_i, used for retrieving ST from the three simulation databases above, are those determined in Section 5.3. Figure 5.8 depicts the errors of the LST retrieved using equation 5.3 from each of the three simulation databases as a function of instrumental noise.

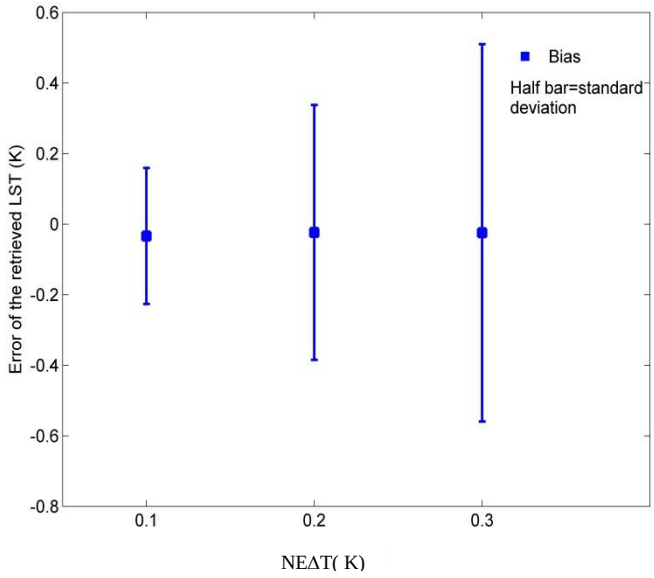

Figure 5.8 Errors of the LST retrieved using equation 5.3 from each the three simulation databases as a function of instrumental noise.

With NEΔT instrumental noise growing from 0.1 K to 0.3 K, the standard error of the retrieved LST goes from 0.19 K to 0.53 K. Therefore, the impact of instrumental noise on the accuracy of the LST retrieved by equation 5.3 is of the order of magnitude of the instrumental noise.

5.5 Accuracy evaluation

5.5.1 With simulation data

First, we have evaluated the developed method by comparing the LST retrieved by that developed method with the true LST using the simulation data in Section 5.3. The error of the retrieved LST is shown in Figure 5.9. From this figure, we can see that the RMSE of the retrieved LST is approximately 0.20 K, and the error of the retrieved LST ranges from -0.6 to 0.9K. Consequently, LST can be accurately retrieved using equation 5.3, with only 10 measurements in the spectral interval of 800 -1200 cm^{-1}.

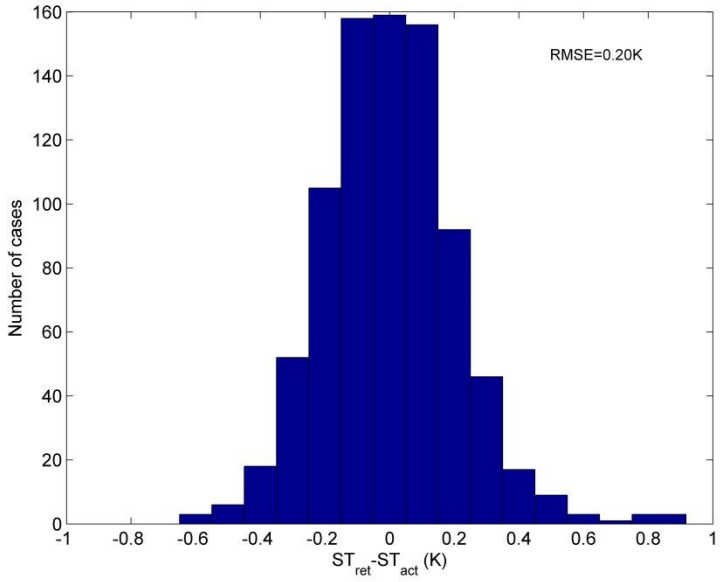

Figure 5.9 Error of the LST retrieved by equation 5.3 from the simulation data with the 139 atmospheric profiles. (STret= the retrieved LST, STact=the true LST)

To evaluate the method independently, we retrieved LST from the independent simulation data mentioned in Section 5.4.1 using equation 5.3 with the coefficients w_i and the central wavenumbers determined in Section 5.3.The error of LST retrieved from this independent simulation data is shown in Figure 5.10. The RMSE of LST retrieved by equation 5.3 is 0.21 K. Our method is quite accurate and promising.

5.5.2 With satellite data

Our developed method was applied to part of the collected Metop-A/IASI data

mentioned in Section 4.2. The five-minute Metop-A Level 1C IASI images sensed in the morning on three clear days in the year 2014 (Feb. 2, Aug. 1 and Nov. 4) were used to evaluate the accuracy of the developed multi-channel method. The used IASI data has a viewing zenith angle less than 15^0 (the surface area covered by this used data is shown in Figure 3.1 with rectangles). The cloud information in the Metop-A/AVHRR SST product was used to select the clear-sky IASI data. Only IASI data with more than 90% clear AVHRR pixels was used for this evaluation. In total, 386 matched IASI samples were used for this application. The procedures for matching Metop-A/IASI data at nadir and Metop-A/AVHRR SST product are described in the following text and in Figure 5.11.

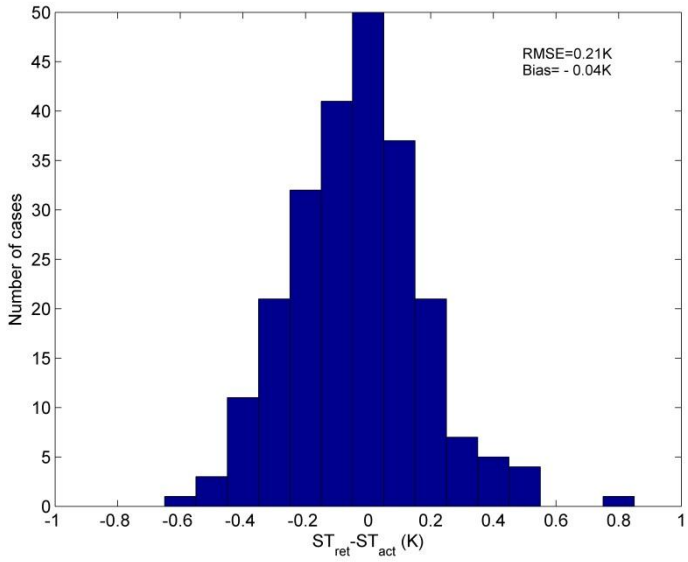

Figure 5.10 Error of the LST retrieved by equation 5.3 from independent simulation data with the other part of TIGR atmospheric profiles. (STret=the retrieved LST, STact=the true LST)

1) The AVHRR pixel at the centre of a certain IASI pixel is located if the distance between the centres of the two pixels is less than 0.1 degree.

2) The criteria for determining other AVHRR pixels inside the IASI pixel is that the distance between the centre of an AVHRR pixel and that of the IASI pixel is less than 5 km.

3) The validated Metop-A/AVHRR SST product is taken as a reference to evaluate the LST retrieved by our developed method from IASI. The comparison of the LST retrieved by our developed method from IASI with the SST product from AVHRR is shown in Figure 5.12. From this figure, we can see that the RMSE of the LST from IASI is 0.43K. The LST can be retrieved accurately from satellite data by the developed method.

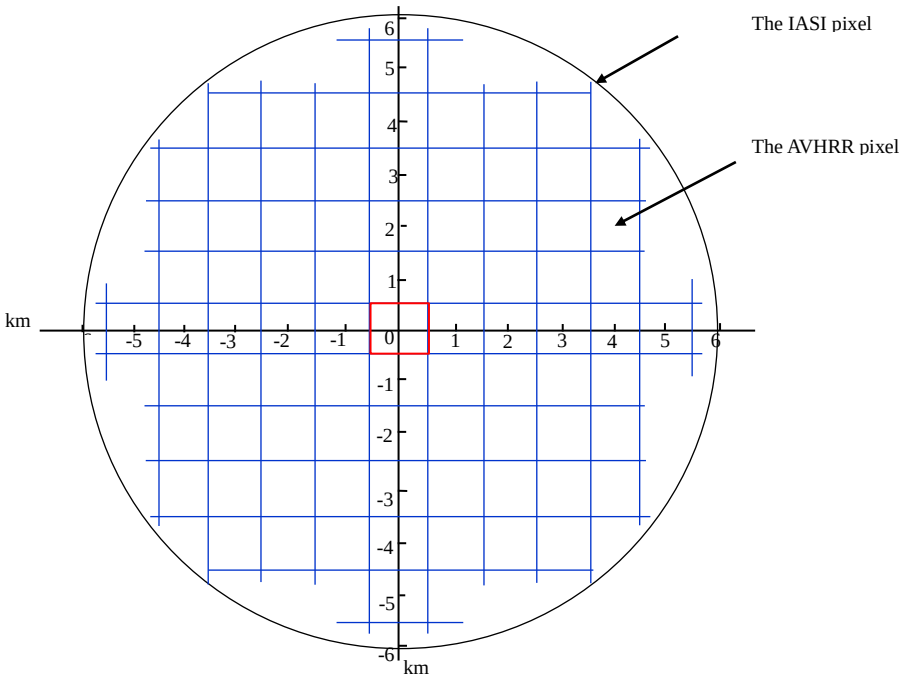

Figure 5.11 The matched Metop-A/AVHRR pixels plotted with the corresponding Metop-A/IASI pixel at nadir

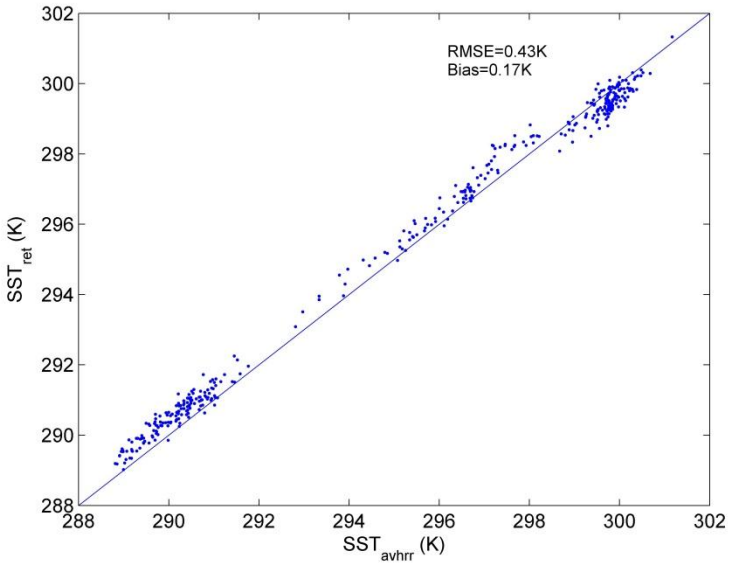

Figure 5.12 Comparison of the LST retrieved by our method from Metop-A IASI data with Metop-A AVHRR SST product over the Mediterranean Sea on three clear days. (ST_{ret}=the retrieved LST, SST_{avhrr}=the AVHRR SST)

The spatial pattern of the LST error retrieved by the developed method from the IASI

image sensed on 4 November 2014 over part of the Mediterranean Sea is shown in Figure 5.13. The error of the retrieved LST is homogeneously distributed, and no important deviation is seen.

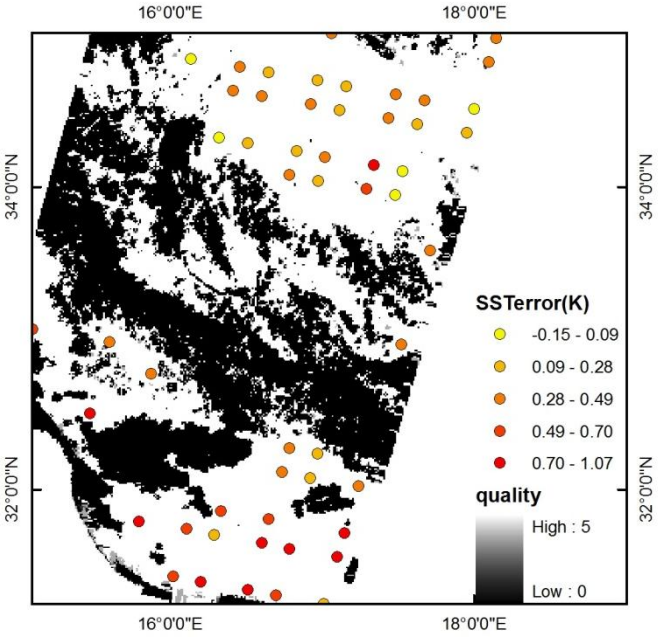

Figure 5.13 Error of the retrieved LST (IASI-AVHRR) plotted on a quality image of Metop-A AVHRR SST product over a part of the Mediterranean Sea on 4 November 2014. ($SSTerror=SST_{iasi} - SST_{avhrr}$)

5.6 Summary and conclusions

In this chapter, with the assumption that LSE is equal to unity, we have developed a multi-channel LST retrieval method for high-emissivity surfaces basing on 10 hyperspectral TIR measurements of a radiometer with a spectral interval of 800 -1200 cm^{-1} and a spectral sampling frequency of 0.25 cm^{-1}. Also, we have evaluated the method using independent simulation data. Moreover, we have analysed the sensitivity of the method to spectral sampling frequency and instrumental noise. This work draws the following conclusions:

1) LST of high emissivity surfaces can be retrieved by our method from independent simulation data with RMSE of 0.21 K, using only 10 hyperspectral TIR measurements. This method is very accurate and promising.

2) The coefficients w_i of the method are dependent on a spectral sampling frequency. Nevertheless, LST of high-emissivity surfaces can still be retrieved accurately when the coefficients are refitted for each spectral sampling frequency.

3) The impact of instrumental noise is not significant: the accuracy of the retrieved LST is of the order of magnitude of the instrumental noise.

4) In comparison with the AVHRR SST product, LST of high-emissivity surfaces can be retrieved from satellite data with a RMSE of 0.43 K. The performance of our method is good for retrieving LST for high-emissivity surfaces from satellite data.

The drawback of our method is that it requires the assumption of LSE of unity. It is only accurate for retrieving LST over high emissivity surfaces with the support of methods to for selecting high emissivity surfaces in land (Tonooka 2001). Our method can’t be applied to natural land surfaces yet.

6 Retrieving LST from hyperspectral TIR data using a multi-channel method with a linear LSE function

6.1 Introduction

In chapter 4, we developed a multi-channel method to retrieve LST for high emissivity surfaces from hyperspectral TIR data containing damaged data at certain channels. However, the multi-channel method for high emissivity surfaces requires the assumption of blackbody LSE. The objective of the work in this chapter is to extend the developed multi-channel method to natural land surfaces with proper consideration of LSE.

6.2 Physical basis of the multi-channel method with linear LSE function

6.2.1 Variation of the channel LSE

The multi-channel method for high emissivity surfaces requires assumption that land surface is blackbody. The higher the channel LSEs are and the less the spectral variation of channel LSE is, the less the effect of channel LSEs on this multi-channel method is. To find the spectral interval [ν_a, ν_b] where channel LSEs are high and constant, we used typical LSE data in the ASTER emissivity library to study the variation in LSE. The LSE data in ASTER emissivity library is introduced in chapter 4 of this thesis. Because pure pixels of rocks, minerals, meteorites, and manmade materials are rare in recent spaceborne hyperspectral TIR data with a spatial resolution of 12 km, we did not use the LSE data of these four materials for this analysis. To eliminate the effect of atmospheric ozone, the spectral interval of 985-1071 cm^{-1} is not considered.

The mean and the standard deviation of the channel LSE as functions of wavenumber are shown in Figure 6.1. The criteria for determining the spectral interval of [ν_a, ν_b] is that the mean values of the channel LSEs are larger than 0.95 and the standard deviations of the channel LSEs are not larger than 0.01. As seen from Figure 6.1, the mean channel LSEs in the spectral interval of 800–950 cm^{-1} are larger than 0.95, and the corresponding standard

deviations of the channel LSEs are approximately 0.01. The mean channel LSE decreases to about 0.943 in the spectral interval of 1071–1200 cm^{-1} and the standard deviation of the channel LSE increases to high values in the spectral interval of 1071–1200 cm^{-1}, ranging between 0.03 and 0.045. We only considered the channels in the spectral interval of 800–950 cm^{-1} in the determination of the central wavenumbers of the channels for the multi-channel method.

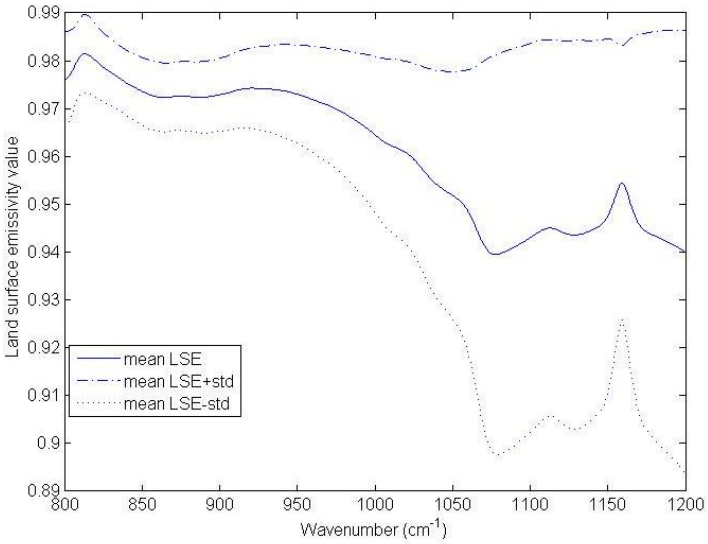

Figure 6.1 The mean value of channel LSE and the standard deviation of the channel LSE as a function of wavenumber

6.2.2 The linear function for expressing LSE spectra

After that, with the LSE data in the spectral interval of 800-950 cm^{-1}, we found that the channel LSEs in the spectral interval of 815-950 cm^{-1} can be represented by a linear function for each material with only two LSE values. The LSE value at channel i centered at wavenumber ν_i can be represented by the following linear function

$$\varepsilon_i = \varepsilon_{815} + \frac{\varepsilon_{950} - \varepsilon_{815}}{135}(\nu_i - 815) \tag{6.1}$$

where ε_i is the LSE value at channel i;

ν_i is the central wavenumber of channel i;

ε_{815} is the LSE value at the channel centered at 815 cm^{-1};

ε_{950} is the LSE value at the channel centered at 950 cm^{-1}.

The errors of the channel LSE reconstructed by the proposed linear function as a function of wavenumber are shown in Figure 6.2. The RMSE of each reconstructed channel LSE is less than 0.01 in the spectral interval of 815cm^{-1}-950cm^{-1}. The channel LSE centered at the

wavenumber ν_i (ν_i = [815 ~ 950 cm^{-1}]) can be accurately represented by the linear function in the left side of the equation 6.1 for most of the materials.

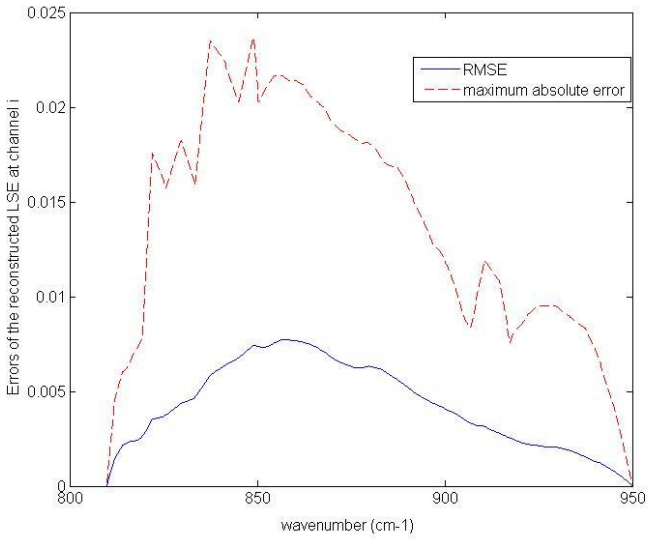

Figure 6.2 The errors the LSE value at channel i reconstructed by the linear function in equation 6.1 as a function of central wavenumber

6.2.3 The multi-channel method with the linear LSE function

Inspired by the SW method, we extended the multi-channel method for retrieving LST from hyperspectral TIR data for high emissivity surfaces to natural land surfaces by parameterizing the coefficients ωi using LSE. According to the extended multi-channel method, LST can be retrieved by

$$
\begin{aligned}
T_s &= \omega_0 + \sum_{i=1:n} (\omega_{s,i} T_{st,i} + \omega_{w,i} T_{we,i}) \\
\omega_{s,i} &= \beta_{s,i,0} + \beta_{s,i,1} \frac{1-\varepsilon_i}{\varepsilon_i} \\
\omega_{w,i} &= \beta_{w,i,0} + \beta_{w,i,1} \frac{1-\varepsilon_i}{\varepsilon_i}
\end{aligned}
\qquad (6.2)
$$

where ω_0, $\omega_{s,i}$ (i = [1:*n*]), $\omega_{w,i}$ (i = [1:*n*]), $\beta_{s,i,0}$, $\beta_{s,i,1}$, $\beta_{w,i,0}$, $\beta_{w,i,1}$ are the regression coefficients (also called ω_i in this paper);

$T_{st,i}$ (i = [1:n]) is the brightness temperature at TOA at a strong-absorption channel i in K;

$T_{we,i}$ (i = [1:n]) is the brightness temperature at TOA at a weak-absorption channel near a strong-absorption channel i in K;

ε_i is the LSE at channel i;

T_s is the land surface temperature in K.

Combination of the equation 6.1 and equation 6.2, LST (T_s) can be retrieved by

$$T_s = \omega_0 + \sum_{i=1:n} (\omega_{s,i} T_{st,i} + \omega_{w,i} T_{we,i})$$

$$\omega_{s,i} = \beta_{s,i,0} + \beta_{s,i,1} \frac{1 - (6.62 - \frac{\nu_{s,i}}{135})\varepsilon_{815} + (\frac{\nu_{s,i}}{135} - 6.62)\varepsilon_{950}}{(6.62 - \frac{\nu_{s,i}}{135})\varepsilon_{815} - (\frac{\nu_{s,i}}{135} - 6.62)\varepsilon_{950}}$$

$$\omega_{w,i} = \beta_{w,i,0} + \beta_{w,i,1} \frac{1 - (6.62 - \frac{\nu_{w,i}}{135})\varepsilon_{815} + (\frac{\nu_{w,i}}{135} - 6.62)\varepsilon_{950}}{(6.62 - \frac{\nu_{w,i}}{135})\varepsilon_{815} - (\frac{\nu_{w,i}}{135} - 6.62)\varepsilon_{950}} \quad (6.3)$$

where $\nu_{s,i}$, $\nu_{w,i}$ are the central wavenumber of the strong-absorption channel i and the weak-absorption channel i.

The coefficients ω_i and the central wavenumbers of channel i (i=[1:n]) in equation 6.3 are determined using simulation data with input of the LSE conditions and water vapor content. To reduce impact of the variation LSE, we only considered channels in the spectral interval of [815cm^{-1},950cm^{-1}] in determination of the central wavenumber of channel i. The procedures for determining the coefficients ω_i and the central wavenumbers of channel i (i=[1,n]) are detailed in the following section.

For determination of the coefficients ω_i and the central wavenumbers of channel i in equation 6.3, we classified the LSE conditions of natural surfaces into four types. The channel LSE value centered at 950 cm^{-1} as a function of the channel LSE value centered at 815 cm^{-1} is shown in Figure 6.3. As seen from the Figure 6.3, the LSE conditions of natural surfaces can be classified into 4 types according to the mean value of two channel LSEs centered at 815 cm^{-1} and centered at 950 cm^{-1} (ε_a) and the difference between the channel LSE at 950 cm^{-1} and the channel LSE at 815 cm^{-1} (ε_{950}-ε_{815}): (1) $\varepsilon_a > 0.95$, $\varepsilon_{815} - \varepsilon_{950} < -0.02$, (2) $\varepsilon_a > 0.95$, $-0.02 < \varepsilon_{815} - \varepsilon_{950} < 0.03$, (3) $\varepsilon_a > 0.95$, $0.03 < \varepsilon_{815} - \varepsilon_{950}$, (4) $\varepsilon_a < 0.95$, $-0.02 < \varepsilon_{815} - \varepsilon_{950} < 0.03$. In application of the proposed multi-channel method to satellite data, the channel LSE at 815 cm^{-1} ε_{815} and the channel LSE at 950 cm^{-1} ε_{950} were determined using MODIS LSE product (introduced in Section 4.2.3) in this study.

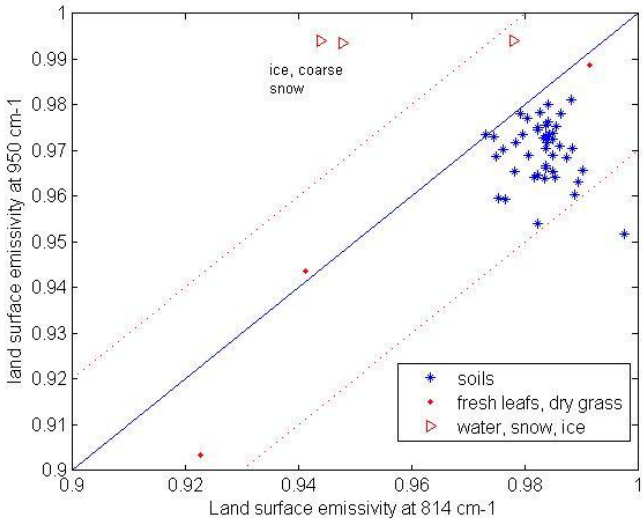

Figure 6.3 The channel LSE at 950 cm^{-1} as a function of the channel LSE at 815 cm^{-1}

6.3 Determination of the coefficients and the central wavenumbers

6.3.1 Construction of simulation database

To determine the initial strong-absorption channels and the initial weak-absorption channels for equation 6.3, we simulated data using 4A/OP with a tropical atmospheric profile from TIGR database. The total precipitable water vapor and the bottom temperature of the selected atmospheric profile are 3.98 g/cm^2 and 296.8 K, respectively. The LST and LSE for the simulation were 286.8 K and the LSE spectrum of deciduous trees from ASTER emissivity library, respectively. The hyperspectral brightness temperature data at TOA for nadir observations was simulated as mentioned in section 5.3.3.

To determine the ω_i coefficients the central wavenumbers of channel i in equation 6.3, we simulated a large amount of data using 4A/OP using the method mentioned in section 5.3.3 with typical clear-sky atmospheric profiles from the TIGR atmospheric profile database. The 139 TIGR profiles and the LST data for simulation were those mentioned in Section 5.3.1. For each simulation condition, the LSE data for the simulation was the data referred to in Section 6.2.1. A random noise with a NEΔT of 0.1 K was added to the simulated brightness temperature data at TOA. In total, 39198 simulation cases were used in this study.

6.3.2 Procedures for determining the central wavenumber of channel i and the coefficients ω_i

We selected the initial strong-absorption channels and the initial weak absorption channels in two steps using the simulated brightness temperature data mentioned in Section 6.3.1. We first selected a weak-absorption channel from each micro atmospheric window in the spectral interval of 815–950 cm^{-1}. Then, we selected a nearby strong-absorption channel for each weak absorption channel with the criteria that the brightness temperature difference between the strong-absorption and weak-absorption channel is larger than c K. The value of c for this study is an empirical value of 0.4.

Using the large amount of simulation data mentioned above, using the initial strong-absorption channels and the weak-absorption channels, we determined the ω_i coefficients and the central wavenumbers of channels in equation 6.3 using the stepwise regression method. The criterion for determination of the number of channels is that the RMSE of the LST retrieved from the simulation data using the determined channels and the determined coefficients reaches 0.5 K. The procedures for determination of the ω_i coefficients and central wavenumbers of channel pair i are shown in Figure 6.4.

The LST retrieved by the equation 6.3 from the simulation data decreases to about 0.5 K when the number of channel pairs increases to 5 (shown in Figure 6.5). The determined coefficients ω_i and the determined central wavenumbers of the strong-absorption channels and the weak-absorption channels are shown in Figure 6.6. The coefficients ω_i (i = [1, 5]) vary over a small range from approximately −3 to 3. The determined central wavenumbers distribute equally in the spectral interval of 815-950 cm^{-1}.

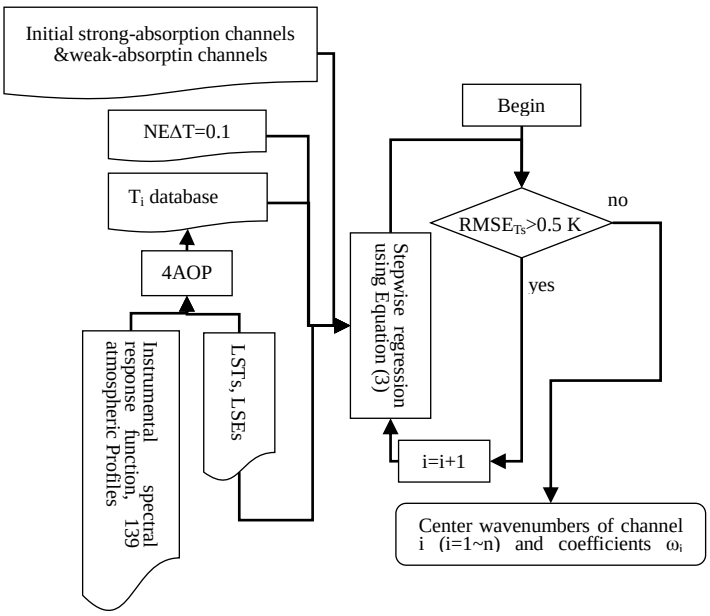

Figure 6.4 The procedures for determining the coefficients ω_i and the central wavenumbers of channels in equation 6.3

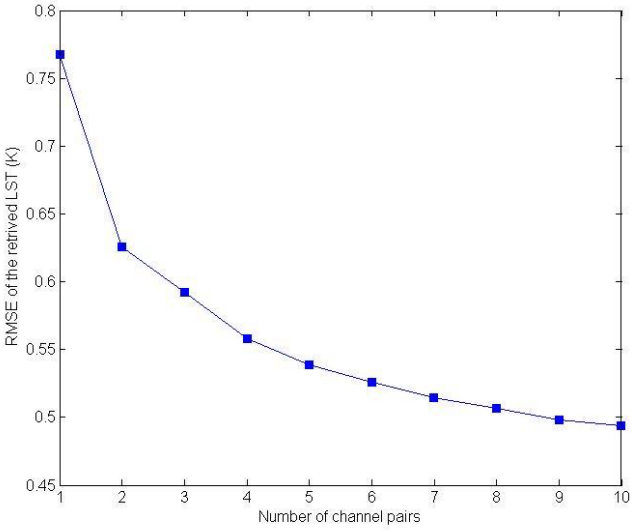

Figure 6.5 The RMSE of the retrieved LST as a function of the number of channel pairs in the process for determination of central wavenumbers and coefficients ω_i

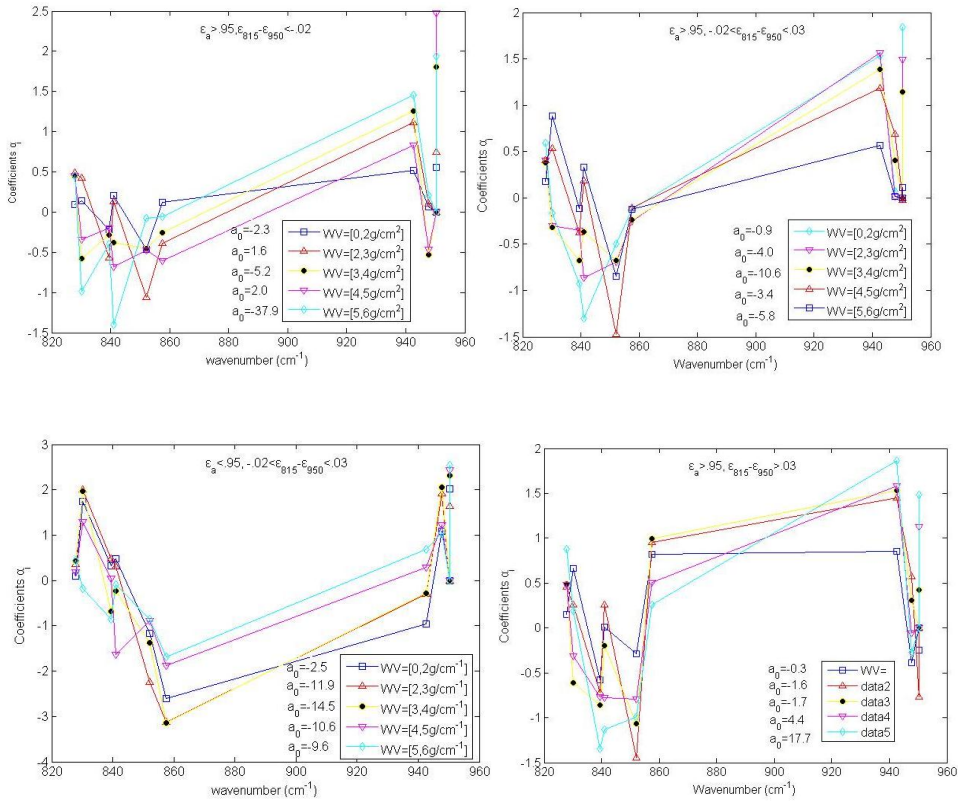

Figure 6.6 The determined ω_i coefficients and the determined central wavenumbers of channel pair i

6.4 Sensitivity analysis

6.4.1 Sensitivity to land surface emissivity

To analyze the sensitivity of this extended multi-channel method to LSE, we retrieved LSTs from the simulation data with the 139 atmospheric profiles mentioned in Section 5.3.1 using the extended multi-channel method with known water vapor content and known LSE condition, and analyzed the variation of the error of the retrieved LSTs with the four LSE conditions of natural surfaces. The error of the retrieved LSTs for each simulation database as a function of the LSE condition is shown in Figure 6.7.

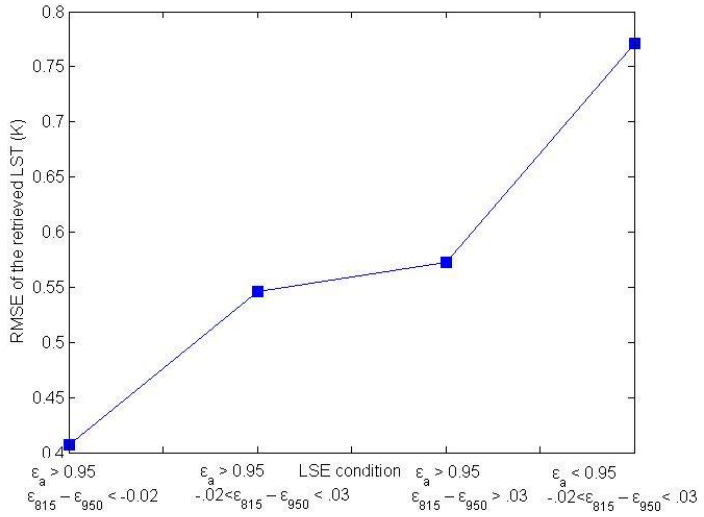

Figure 6.7 The error of the retrieved LSTs for each LSE condition as a function of the LSE condition

As the mean value of channel LSEs in the spectral interval of [815, 950cm-1] decreasing from larger than 0.95 to less than 0.95, the RMSE of the retrieved LSTs for the simulation database with the corresponding LSE condition grows from approximately 0.5 K to approximately 0.8 K. The LST retrieved by the extended multi-channel method has larger errors when the mean value of channel LSEs is low. Note that the RMSE of the retrieved LSTs for a large part of the simulation data with a mean channel LSE value of larger than 0.95 is less than 0.6 K.

6.4.2 Sensitivity to instrumental noise

To conduct this sensitivity analysis, we created three simulation databases by adding noise to noiseless IASI data with NEΔT = 0.1 K, 0.2 K, and 0.3 K. The noiseless IASI data were created using the atmospheric profile data, the LST data, and the LSE data mentioned in Section 5.3.1. The method for adding noise to the noiseless simulation data is detailed in Section 5.4.2. The extended multi-channel method was used to retrieve LST from the three simulation databases with known water vapor content and known LSE condition. Figure 6.8 depicts the error of the LST retrieved from each simulation database by the extended multi-channel method as a function of the instrumental noise.

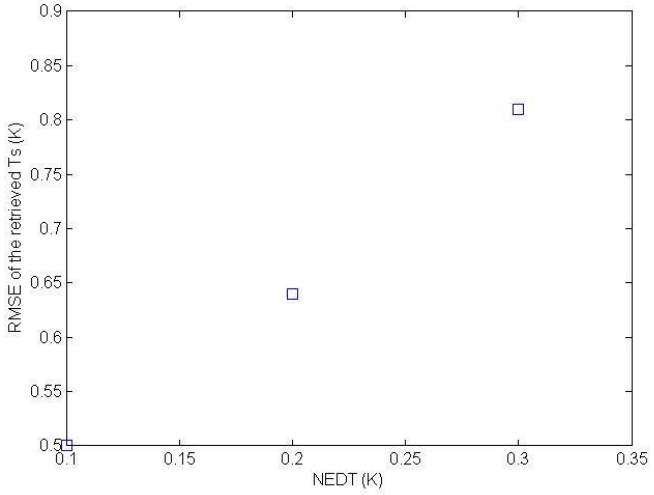

Figure 6.8 The error of the LST retrieved from each noise-added simulation database as a function of the instrumental noise

When the NEΔT for the simulation database is equal to that used to develop this extended multi-channel method (0.1 K), the RMSE of the LST retrieved from the simulation database is 0.5 K. For the NEΔTs of 0.2 K and 0.3 K, the RMSEs of the LST retrieved from the corresponding simulation databases increase to 0.65 K and 0.8 K, respectively. Therefore, the accuracy of the LST retrieved using equation 6.3 is not significantly affected by the instrumental noise.

6.4.3 Sensitivity to error of water vapor content

To conduct this sensitivity analysis, we retrieved LST from the simulation data mentioned in Section 6.3.1 using equation 6.3 with error-added water vapor content and known LSE condition. The errors of the water vapor content for this analysis are -20%, -10%, 0%, 10%, 20%, respectively. The error of the LST retrieved by equation 6.3 from the simulation data using each error-added water vapor content data as a function of the error of water vapor content is shown in Figure 6.9.

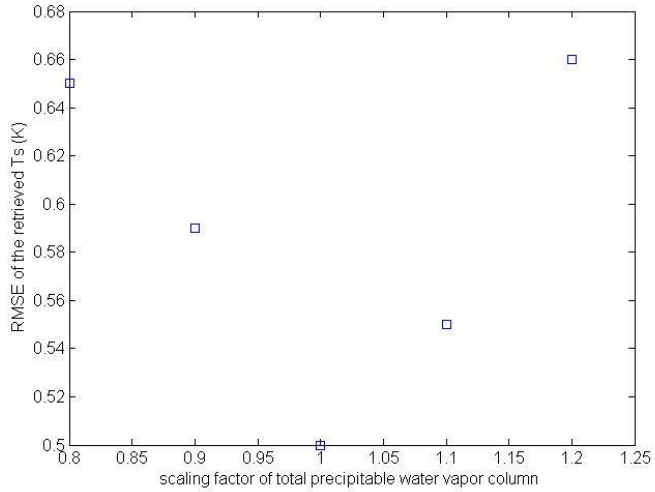

Figure 6.9 The error of the LST retrieved by equation 6.3 using error-added water vapor content data from simulation data as a function of the error of water vapor content

When the error of the total precipitable water vapor column changes from 0% to 10% and 20%, the RMSE of the retrieved LST increases approximately by 0.1 K and 0.2 K, respectively. The impact of error of water vapor content on the accuracy of the LST retrieved by equation 6.3 is not significant.

6.5 Accuracy evaluation

6.5.1 With simulation data

We evaluated the accuracy of the extended multi-channel method with the independent simulation data. The central wavenumbers of the channels and the coefficients ω_i determined in Section 6.3.2 were used to retrieve LST from the independent simulation data with known LSE condition and known water vapor content. The atmospheric profile data and the LST data for this independent simulation are mentioned in Section 5.4.1. The atmospheric profiles for the independent simulation were different from the atmospheric profiles for simulation in Section 6.3.1. The total precipitable water vapor column of the selected atmospheric profiles ranged from 0 g/cm2 to 5 g/cm2. The LSE data and the instrumental noise for the simulation were those mentioned in Section 6.3.1.

The errors of the LSTs retrieved using equation 6.3 for the independent simulation data were shown in Figure 6.10. The bias and the RMSE of the LST retrieved from the independent simulation data are -0.03 K and 0.54 K, respectively.

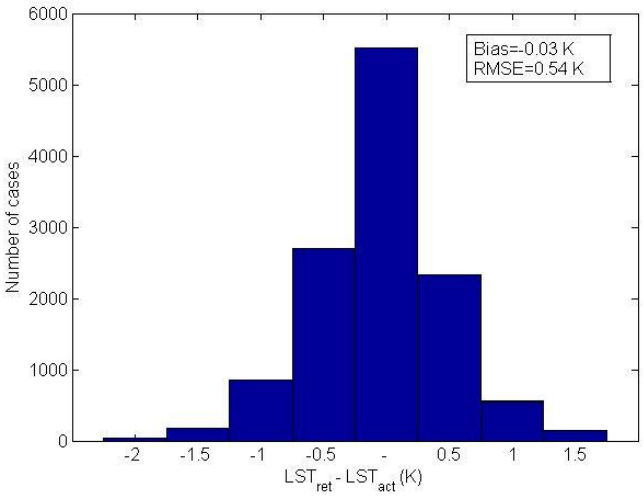

Figure 6.10 The errors of the LST retrieved using Equation 6.3 from the independent simulation data (LST_ret = the retrieved LST and LST_act = the true LST).

6.5.2 With satellite data

The simulation model itself has uncertainty; therefore, we applied the extended multi-channel method to Metop-A/IASI data measured on April, November 2012 over Australia with matched ESRL atmospheric profile data mentioned in Section 4.3.3, and evaluated its accuracy by comparing the retrieved LST with the Level 2 LST product from the METOP-A/IASI. The Australia area for collecting Metop-A/IASI data is introduced in Section 4.1. The land cover types in the Australia were mainly soil surfaces and vegetated surfaces.

The cloud information in the Metop-A/IASI LST product was used to determine the clear-sky pixels. The Metop-A/IASI pixels with cloud fraction of less than 2% were used for this evaluation. The criterion for matching the ERSL atmospheric profile data and the clear-sky Metop-A/IASI data was that the difference of time between the Metop-A/IASI data and the ERSL atmospheric profile data is less than 0.5 hr, and the Euclidean distance between the center of a IASI pixel and the field site of a ERSL atmospheric profile is less than 0.5 º. An error of ±10% was added to the total precipitable water vapor column data computed from the matched ERSL atmospheric profile data. In total, 17 matched cases were used for this evaluation with the satellite data.

The comparison of the LST retrieved by the extended multi-channel method from the IASI data with the Level 2 LST product from Metop-A/IASI is shown in Figure 6.11. In comparison with the Metop-A/IASI LST product, the RMSE of the retrieved LST is 2.1 K,

and the mean value of the difference between the two LST datasets is 0.26 K. On the whole, there is no large difference between the two LST datasets.

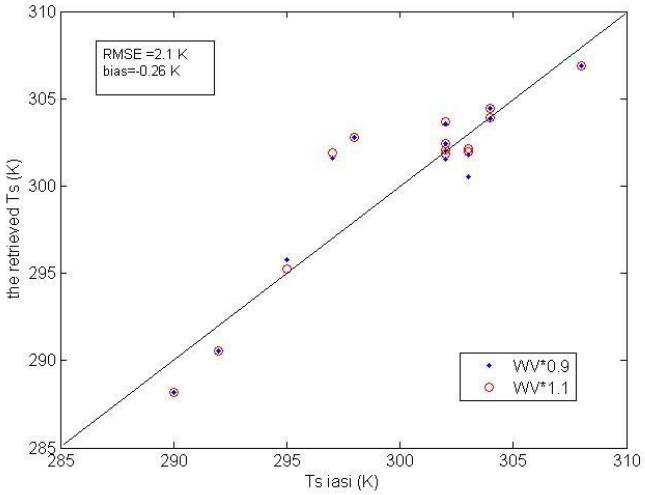

Figure 6.11 Comparison of the LST retrieved by the extended multi-channel method from matched Metop-A IASI data with Metop-A/IASI LST product over Australia in March and August 2012. (Ts iasi=the Metop-A/IASI LST product)

6.6 Summary and conclusions

With introduction of a linear function for expressing LSE spectra in the spectral interval of 815–950 cm^{-1}, we extended the multi-channel method to natural land surfaces using 10 hyperspectral TIR measurements centered in the spectral interval of 815–950 cm^{-1} with known LSE condition and known water vapor content. Then, we analyzed its sensitivities to LSE, to the error of water vapor content and to the instrumental noise using simulation data. Finally, we evaluated the accuracy of this multi-channel method using independent simulation data at nadir and satellite data near nadir. This work draws the following conclusions:

With known LSE condition and the atmospheric water vapor content data with error of 10%, LST can be retrieved by the extended multi-channel method from the simulation data with an RMSE of 0.60 K using hyperspectral TIR data at only 10 channels.

As the mean value of channel LSE in the spectral interval of 815–950 cm^{-1} decreases from the value of larger than 0.95 to the value of less than 0.95, the error of the LSTs retrieved by the extended multi-channel method from the simulation data with each LSE condition increases from 0.5 K to 0.8 K. In addition, the impact of the instrumental noise on the extended multi-channel method is approximately two times its magnitude.

With MODIS LSE product and NOAA/ESRL atmospheric profile, LST can be retrieved by the extended multi-channel method from the IASI/Metop-A data with a difference of 2.1 K on average in comparison with the LST product from the Metop-A/IASI.

The extended multi-channel method can be used for near-real-time retrieval of LST from hyperspectral TIR data and to provide the physical method to simultaneously retrieve atmospheric profiles, LST, and LSE with first-guess LST value in the future. The limitations of the multi-channel method are that it requires known LSE condition in the spectral interval of 815–950 cm^{-1} and known atmospheric water vapor content, and that it has not been extended for off-nadir measurements yet.

7 Unmixing component temperatures from high spatial resolution hyperspectral TIR data

7.1 Introduction

Component temperatures, component emissivities and component abundances in a mixed pixel are important parameters for various applications. Hyperspectral TIR data, containing large amount of information about composition of materials in mixed pixels, is an important source of information for retrieving component parameters.

The objective of this chapter is to develop a physics-based method to unmix component temperatures for heterogeneous surfaces with the large variation of component temperature from high spatial resolution hyperspectral TIR data.

7.2 Physics-based temperature unmixing method

The component temperatures are retrieved by a three-step procedure:

1) First the LST and LSE over a pure pixel are retrieved by the TES method developed by Gillespie et al. (1998). The identification of pure pixels is done by classifying a co-registered hyperspectral image acquired in the visible domain.

2) Assuming each material has a pure pixel in TIR image, the initial component temperatures and initial component abundances over mixed pixels are retrieved by the TRUST method using the LSTs and the LSEs retrieved over the pure pixels.

3) Component temperatures and components abundances over mixed pixels are simultaneously retrieved by the proposed physics-based TUM method using the retrieved initial values of the component parameters. The radiative transfer equations are differentiated around the initial component abundances over a mixed pixel. Then, component temperatures and component abundances are jointly estimated by a minimization of the reconstruction error of the mixed pixel BOA radiance.

The flowchart of the three-step procedure is shown in Figure 7.1.

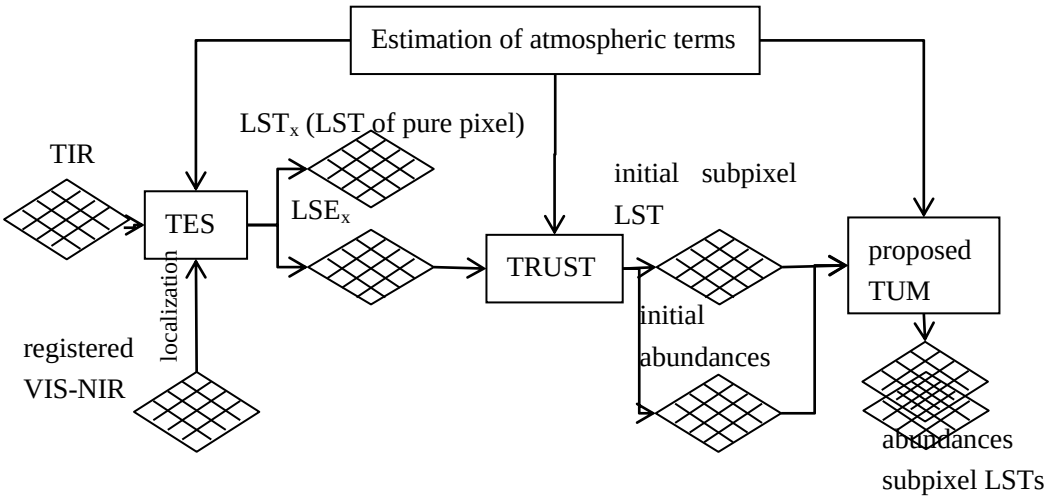

Figure 7.1 Flowchart of the three-step procedure for retrieving component temperatures over heterogeneous surfaces. The TES method is used to retrieve LSTs and LSEs over pure pixels. The TRUST method is to retrieve initial component temperatures and component abundances over mixed mixed pixels with large variation of component temperatures. The proposed TUM method is to refine the initial component temperatures and the initial component abundances over mixed pixels.

A. Selection of pure pixels

Pure pixels are selected by the classification of the co-registered hyperspectral image in the visible domain (Dimmeler et al. 2013). The method bases on the selection of homogeneous areas in the image. A larger area of pure pixels is selected and erosion is applied to select pure pixels far away from the border. Erosion is used to allow the co-registration error. The erosion with structure element of 3×3 pixels is used to ensure the selected pure pixels are reliable.

One of the shortcomings of using an image in the visible domain is that a couple materials can be recognized as diffident in the visible domain but similar in the thermal infrared domain. On the other hand, a couple of materials can be identified as similar in the visible domain but different in the thermal infrared domain. Another limitation of this classification method is that it requires a hyperspectral image in the visible domain.

B. Retrieval of LST and LSE over a pure pixel

The TES method retrieves LSE and LST over a pure pixel with known atmospheric terms and consists of three modules: the NEM, the SR method and the MMD. The NEM retrieves the initial values of LST and LSE. Assuming the maximum spectral LSE is equal to 1, this

module uses the maximum of the brightness temperature as the LST. The spectral emissivity is retrieved by inverting the radiative transfer equation with the estimated surface temperature and known atmospheric terms. The SR module estimates the shape of the spectral emissivity by calculating the ratio of the retrieved spectral emissivity to its mean value. The SR module is less sensitive to the initial value of surface temperature. The MMD module refines the minimum spectral emissivity by using an empirical relationship between the minimum spectral emissivity and the spectral contrast of emissivity. This empirical relation is expressed as

$$\varepsilon_{\min} = \alpha_1 + \alpha_2 (MMD)^{\alpha_3} \tag{7.1}$$

where α_1, α_2, α_3 are coefficients determined using emissivities of man-made materials, vegetations and soils from the ASTER database (Hulley et al. 2009a). The last two modules (the SR module, the MMD module) are carried out several times to get more accurate results.

The TES method is accurate, except for materials with low spectral contrast of emissivity such as vegetation, water, copper. The method has large error when the atmosphere is very wet.

The TES method is applied to selected pure pixels to separate temperature and emissivity. The mean parameters of are evaluated to give a statistical representative value for each type of material in the image.

C. Retrieval of component abundances over a mixed pixel

This method requires assumptions that the component temperatures are known, that each type of surface has pure pixels in the image and that the initial values of component abundances are acceptable. First, differential radiative transfer equations are calculated around the initial values of component abundances over a mixed pixel and are written as

$$\begin{pmatrix} \Delta R_g(\lambda_1) \\ \vdots \\ \Delta R_g(\lambda_{N_\lambda}) \end{pmatrix} = \begin{pmatrix} A_s(\lambda_1, S_1) & \vdots & A_s(\lambda_1, S_N) \\ & \vdots & \\ A_s(\lambda_{N_\lambda}, S_1) & \vdots & A_s(\lambda_{N_\lambda}, S_N) \end{pmatrix} \begin{pmatrix} \Delta S_1 \\ \vdots \\ \Delta S_N \end{pmatrix} \tag{7.2}$$

where $\Delta R_g = \{\sum(R_g(S_i,T_i) - R_g(S_{f,i}, T_{s,f,i})), i=<1,M>\}$; $S_{f,i}$ is the initial component abundance i composing the mixed pixel; $T_{s,f,i}$ is the initial component temperature i; $\Delta S_i = S_i - S_{f,i}$; λ_j is the central wavelength of channel j; N_λ is the number of channels; N is the number of materials composing the mixed pixel;

with

$$A_s(\lambda_j) = \varepsilon(\lambda_j) \cdot B(T_{s,i}, \lambda_j) + [1 - \varepsilon(\lambda_j)] \cdot R_{atm\downarrow}(\lambda_j).$$

With N_λ equations, $N \leq N_\lambda$ represents an overdetermined problem. In real hyperspectral

TIR satellite data, the $N<<N_\lambda$.

Then, a best linear unbiased estimator is used to retrieve component abundances over a mixed pixel. The best linear unbiased estimator is written as

$$\Delta S = (A_s^T \cdot C^{-1} \cdot A_s)^{-1} \cdot A_s{}^T \cdot C^{-1} \cdot \Delta R_g \quad (7.3)$$

where A_s^T is transpose of matrix $\mathbf{A}_s$.

In this step, the method for retrieving component abundances requires component temperatures are known which is usually difficult to obtain. In the next step of this three-step procedure for retrieving component temperature, component temperatures and component abundances are simultaneously retrieved by a proposed TUM method by a minimization of reconstruction error.

D. Simultaneously retrieval of component temperatures and component abundances on a mixed pixel

With initial parameters of components retrieved by the TRUST method and accurate atmospheric correction, component temperatures and component abundances are simultaneously retrieved by an improved physics-based TUM method. The reconstruction error introduced in our developed TUM method is expressed as

$$D(\vec{T}_s) = \sqrt{\frac{1}{N_\lambda}\sum_{\lambda}\left(\frac{R_s(\lambda) - R_{atm\uparrow}(\lambda)}{\tau(\lambda)} - R_g(\vec{S}, \vec{T}_s, \lambda)\right)^2} \quad (7.4)$$

where $\vec{T_s}$ is a vector of component temperatures in the mixed pixel; $\vec{S}$ is a vector of component abundances in the mixed pixel; N_λ is the number of used channels; λ_i is the central wavelength of channel i.

The improved physics-based method retrieves component temperatures and component abundances using two reconstruction errors. In first step, for the set of component emissivities and the initial component abundances determined by the TRUST method, with a series of possible component temperatures, a series of possible component abundances are estimated by equation 7.3. Component temperatures and component abundances are estimated by minimizing the reconstruction error $D(\vec{T_s})$. In the second step, to stabilize the solution of radiative transfer equations in the improved physics-based TUM method, a second cost function, namely $D_S(\vec{T_s})$, is introduced

$$D_S(\vec{T}_s) = \begin{cases} D(\vec{T}_s), D(\vec{T}_s) - D_T(\vec{S}) > \beta \\ D_T(\vec{S}), D(\vec{T}_s) - D_T(\vec{S}) \le \beta \end{cases} \quad (7.5)$$

where $D_T(\vec{S})$ is the cost function used by the TRUST method; β is the parameter balancing the

quality of the improved physics-based TUM method and the quality of the TRUST method. If β is too large, the initial component abundances and initial component temperatures are not improved; if β is too small, the simultaneously retrieval of component temperatures and component abundances is not stable. β is set to 0.000006 in this thesis.

7.3 Construction of simulation database for unmixing component temperatures

To evaluate the accuracy of the developed TUM method, we simulated large amount of hyperspectral TIR data over a flat surface scene composed of two materials using a typical TIGR atmospheric profile and the LSEs of urban materials from the literature (Cuberso-Custan, 2015). The two urban materials for simulation were grass and gravel with mean temperatures of 295 K and 315 K. The bottom temperature and the total precipitable water vapor content of the selected TIGR atmospheric profile were 298.12 K and 2.0 g/cm^2. The component abundance of grass varied from 70% to 30% by 2%. The LSE spectrums of urban materials had a wavelength interval of 8 - 12 μm. The characteristics of IASI were used to simulate the BOA radiance at nadir. The spectral interval of the simulate BOA radiance was 8 – 12 μm and its spectral sampling frequency was 0.25 cm^{-1}. The procedures for creating the flat surface scene are mentioned as follow and are illustrated in Figure 7.2.

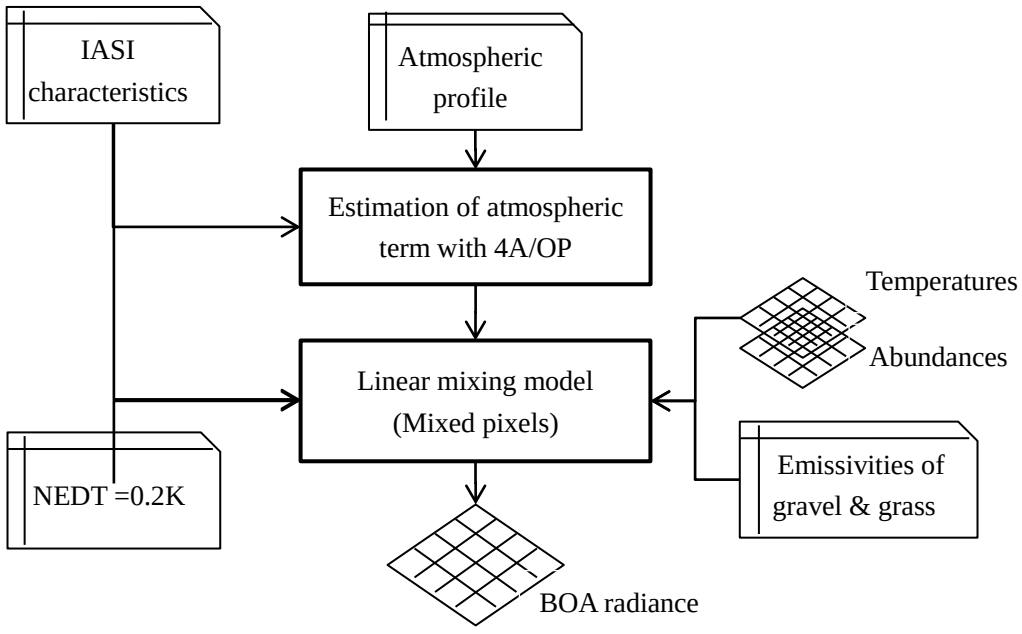

Figure 7.2 Flowchart of the method for creating simulation database for heterogeneous surfaces

(1) Atmospheric radiative terms were simulated using 4A/OP model with the selected

atmospheric profile data;

(2) Component temperature images of 6×8, which represent the temperatures of gravel or the temperatures of grass over the flat scene, were created by a 2D Matlab random number generator. The standard deviation of component temperatures for each material was set to 6 K. The spatial distribution of component temperature was random distribution over the whole scene. The component abundance image of gravel for simulation varied from 70% to 30%. The sum of component abundance of grass and component abundance of gravel in a mixed pixel is 100%. The component temperatures and component abundance images for simulation are shown in Figure 7.3 and Figure 7.4.

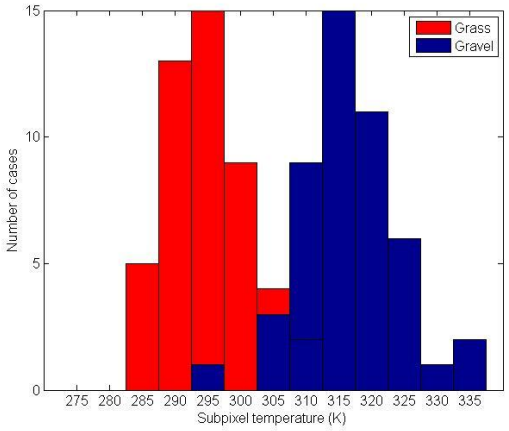

Figure 7.3 Histgrams of gravel component temperature data and grass component temperature data used to simulate mixed-pixel BOA radiance over heterogeneous surfaces. The grass component temperature data has a mean value of 295 K with standard deviation of 6 K. The gravel component temperature has a mean value of 315 K with a standard deviation of 6 K.

(3) The BOA radiance over a mixed pixel was created using linear mixing model with the simulated atmospheric radiative terms, the component temperature images, the component abundance images and the LSE spectrums. The LSE spectrums of grass and gravel are shown in Chapter 4.

(4) One noise equivalent temperature difference vector added to a mixed-pixel BOA radiance spectrum was a vector of 1×1667 created by the matlab random number generator with a mean value of 0 K and a standard deviation of 0.2 K. This instrumental noise was added to each mixed-pixel BOA radiance spectrum for 20 times.

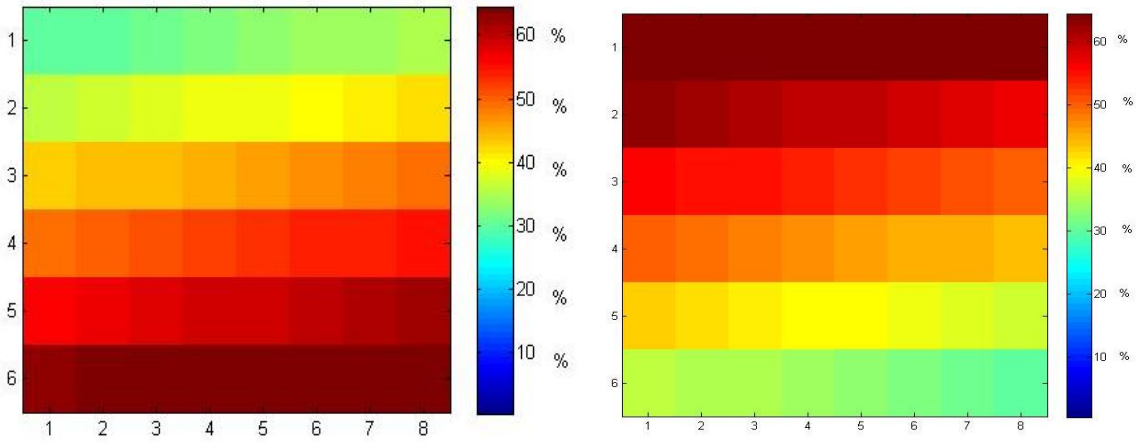

(a) (b)

Figure 7.4 Images of gravel component abundance (a) and grass component abundance (b) used to simulate mixed-pixel BOA radiance data over heterogeneous surfaces

7.4 Accuracy Evaluation

7.4.1 Methodology

The TRUST method is a physics-based TUM designed for hyperspectral TIR sensor with high spatial resolution. The TRUST method relies on a minimization of the reconstruction error of the mixed-pixel radiance to jointly retrieve component parameters. The rationale of TRUST is introduced in Chapter 3 of this thesis in detail.

It is impractical to evaluate the accuracy of the component temperatures retrieved by the developed physics-based TUM with the spatially and temporally collocated field-measured component temperatures. To carry out this evaluation, we resorted to synthetic method, which creates BOA radiance using linear mixing model and 4A/OP with simulation data as mentioned in Section 6.3.

The developed TUM method and the TRUST method were applied to the simulation data mentioned in Section 7.3. The accuracy of the component temperatures and component abundances retrieved from the simulation data by the developed TUM method were analyzed. Moreover, the performance of the developed TUM method was evaluated by using a comparison with the TRUST method. The procedures for applying the developed TUM method and the TRUST method to the simulation data are listed as follow.

(1) To reduce the impact of the error of atmospheric radiative terms on the developed TUM, only bands where atmospheric transmittance is relative larger were used by the developed TUM method and the TRUST method in this study. The criteria for selecting the channels

was that the transmittance at a channel for a typical atmosphere is larger than 0.8. The atmosphere used for selecting the channels was the TIGR profile selected for data simulation, which was mentioned in Section 7.3. The central wavenumbers of the determined bands are shown in Figure 7.5.

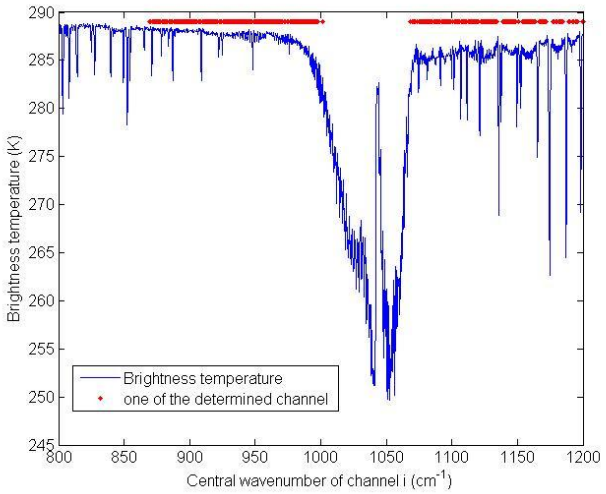

Figure 7.5 Illustration of the central wavenumbers of the determined channels with a typical spectrum of IASI brightness temperature at TOA

(2) The spectra of downwelling atmospheric radiance for the simulated data were estimated by 4A/OP with the atmospheric profile data mentioned in Section 7.3.

(3) With the known downwelling atmospheric radiance and the known emissivity spectra of grass, gravel and asphalt, the TRUST method determined the materials composing each mixed pixel and unmixed jointly component temperatures and component abundances from the mixed-pixel BOA radiance mentioned in Section 7.3. An error of +/-0.005 was added to each channel LSE for each material. The LSE errors are distributed homogeneously among the selected channels.

(4) With the known atmospheric radiative term and the error-added emissivities of grass, gravel, the developed TUM method unmixes simultaneously component temperatures and component abundances from the simulated BOA radiance mentioned in Section 7.3 using the coarse results of the TRUST method.

The root mean square error ($RMSE_T$) of the retrieved component temperatures and $RMSE_S$ of the retrieved component abundances were two indices introduced to express the performances of the developed TUM method and the TRUST method.

$$RMSE_T = \sqrt{\frac{1}{N_m \times 2}\sum_i \sum_j (T_{ret,i,j} - T_{true,i,j})^2}, i = \{1,2\}$$

$$RMSE_S = \sqrt{\frac{1}{N_m \times 2}\sum_i \sum_j (S_{ret,i,j} - S_{true,i,j})^2}, i = \{1,2\} \quad (7.6)$$

where i is the No. of a component (i = 1 represents the component of grass; i = 2 represents the component of gravel);

j is the No. of a mixed pixel;

$T_{ret,i,j}$ is the retrieved temperature of component i at mixed pixel j;

$T_{true,i,j}$ is the true temperature of component i at mixed pixel j;

$S_{ret,i,j}$ is the retrieved abundance of component i at mixed pixel j;

$S_{true,i,j}$ is the true abundance of component i at mixed pixel j;

N_m is the number of mixed pixel.

7.4.2 Results

The developed TUM method and the TRUST method were applied to the BOA radiance simulated in Section 7.3. The performances of the developed TUM method and the TRUST method are presented in Table 7.1. When standard deviation of component temperatures is 6 K, component temperatures and component abundances retrieved by TRUST method from the simulation data have a $RMSE_T$ of 4.0 K and a $RMSE_S$ of 2.9 %, while component temperatures and the component abundances retrieved by the developed TUM method are more accurate with a $RMSE_T$ of 3 K and a $RMSE_S$ of 2.2%.

Moreover, the spatial patterns of component abundances retrieved by the developed TUM method were analyzed. Images of component abundances retrieved by the developed TUM method from simulation data with large variation of component temperatures are shown in Figure 7.6. The spatial distributions of the retrieved component adundances are the same as those of the true component abundances on the whole. The component abundances retrieved by the developed TUM method can accurately represent the spatial patterns of component abundances.

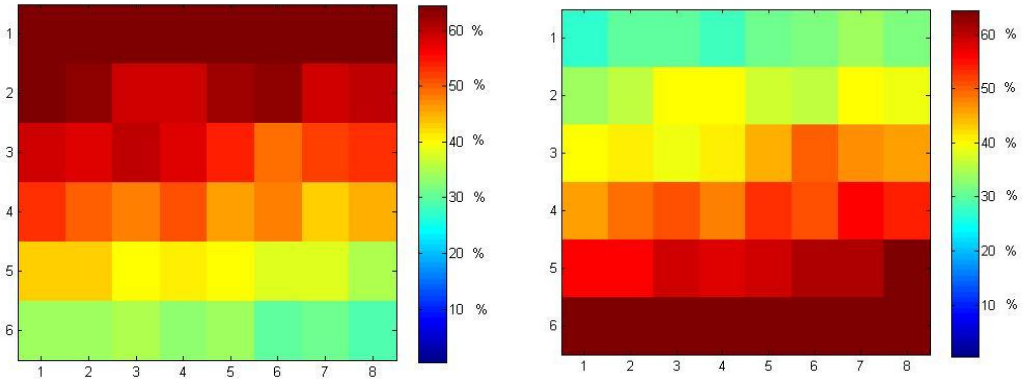

(a) (b)

Figure 7.6 Images of (a) gravel component abundance and (b) grass component abundance retrieved by the developed TUM method from simulation data with standard deviation of component temperatures of 6 K

Table 7.1 Performance of the developed TUM method and the TRUST method over heterogeneous surfaces with large variations of component temperatures

mixing	$RMSE_T$ (K)		$RMSE_S$ (%)	
	our TUM method	TRUST	our TUM method	TRUST
Material 1 & 2	3.0	4.0	2.2	2.9

7.5 Sensitivity analysis

7.5.1 Sensitivity to standard deviation of component temperatures

To analyze its sensitivity to standard deviation of component temperatures, three standard deviations of component temperatures, namely 3 K, 6 K and 9 K, were used to simulate BOA IASI radiance as mentioned in Section 7.3. Specifically, for each standard deviation of component temperatures, a simulation database was created as mentioned in Section 7.3. The grass component temperature data for each simulation database was created using the Matlab random number generator with the mean value of 295 K and the corresponding standard deviation. Meanwhile, the mean value of 315 K and the corresponding standard deviation were used to create gravel component temperature data for each simulation database. The atmospheric profile data, the emissivities of grass and gravel, the component abundance data and the instrumental noise for each simulation database were those mentioned in Section 7.3. The errors of component temperatures and component

abundances retrieved by developed TUM method from the BOA radiance in each simulation database were analyzed with standard deviation of component temperatures. The performance of the developed TUM method was compared to that of the TRUST method.

The variations of the performances of the developed TUM method and the TRUST method with standard deviation are shown in Figure 7.7. With standard deviation of component temperatures growing from 3 K to 9 K, the RMSE of the retrieved component temperatures for the developed TUM increases by 1.8 K while that for the TRUST method increases by 4.6 K. Both methods are sensitive to standard deviation of component temperatures. It's encouraging that the developed TUM method is less sensitive to the standard deviation of component temperatures than TRUST.

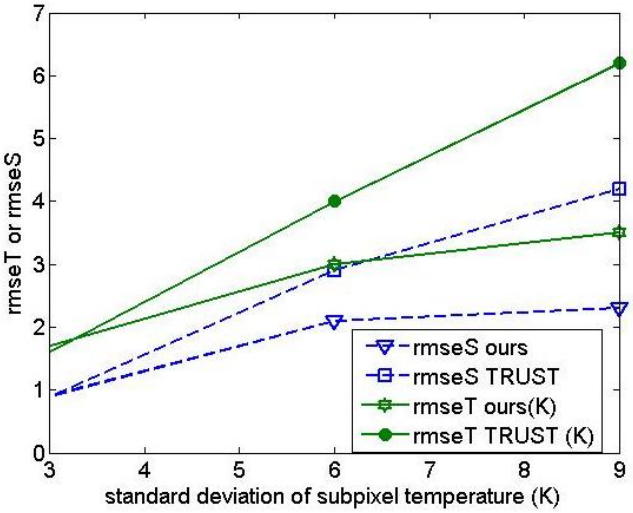

Figure 7.7 Variation of the performances of the developed TUM method and the TRUST method with the standard deviation of component temperatures

7.5.2 Sensitivity to the mean difference between the two component temperatures

To analyze the sensitivity of the developed TUM method to the mean difference between component temperatures, two values for the difference between component temperatures simulation, namely 5 K and 15 K were used to simulate mixed-pixel BOA radiance, while the standard deviation of component temperatures for each material composing mixed pixels was set to 3 K. Specifically, a simulation database was created for each mean difference between the component temperatures as mentioned in Section 7.3. The component temperature data for each simulation database was created by the Matlab random number generator with standard deviation of 3 K and the corresponding mean difference between component temperatures.

The mean grass component temperatures for the two simulation databases were 295 K, 295 K, and the mean gravel component temperature for the two simulation databases were 300 K, 310 K. The atmospheric profile data, the emissivities of grass and gravel, the component abundance data and the instrumental noise for each simulation database were those mentioned in Section 7.3. The developed TUM method and the TRUST method were applied to this simulated BOA radiance, the errors of component temperatures and component abundances retrieved by each method were analyzed with the mean difference between component temperatures.

The errors of component surface parameters retrieved by the developed TUM method and the TRUST method are expressed as a function of the difference between the component temperatures in Figure 7.8. When the difference between component temperatures changes from 15 K to 5 K and the standard deviation of component temperatures is set to 3 K, the RMSE of the retrieved component temperatures for the developed TUM method and that for the TRUST method increase by 0.2 K and 0.4 K, respectively, and the RMSEs of the retrieved component abundances for the two methods both increase slightly from 1.3% to 1.9%. The two TUM methods are not sensitive to the mean difference between component temperatures.

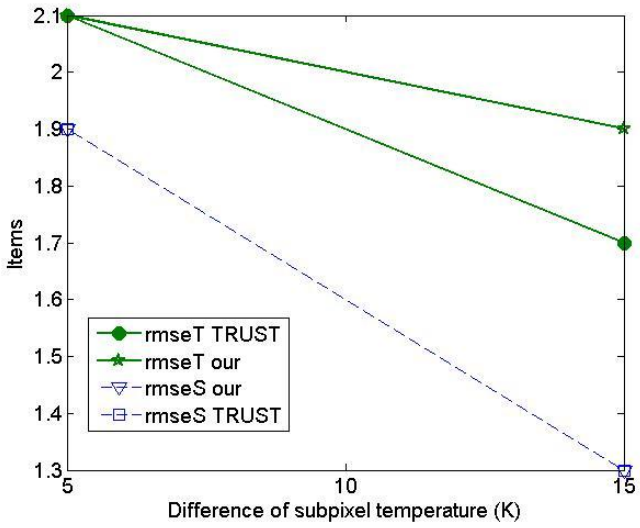

Figure 7.8 Variation of the performances of the developed TUM method and the TRUST method with the mean difference between component temperatures

7.5.3 Sensitivity to the mean difference between the two component emissivities

To analyze the sensitivity of the developed TUM method to the difference between the component emissivities, a set of three emissivities were created for simulation by a linear mixing between the asphalt and the gravel as follow: Gravel is the original gravel, Gravel 1 consists of 50% asphalt and 50% gravel, Asphalt is the original asphalt. The created set of emissivities for simulation was shown with wavenumber in Figure 7.9. In detail, two simulation databases were created as mentioned in Section 7.3 either by using Gravel and Asphalt as component materials with mean difference between component emissivities of 0.07 or by using Gravel 1 and Asphalt as component materials with mean difference between component emissivities of 0.03. For each simulation database, the asphalt component temperature data was created using mean temperature of 335 K with standard deviation of 9 K and the other component temperature data was created using mean temperature of 315 K and standard deviation of 9 K. The component abundances, the atmospheric profile data, the instrumental noise for each simulation database were those mentioned in Section 7.3. The developed TUM method and the TRUST method were applied to the two simulation database, and the variation of the error of each retrieved component surface parameter for each TUM method with the mean difference between component emissivties was analyzed.

The variation of the error of each retrieved surface parameters for each TUM method as a function of the difference between component emissivities is shown in Figure 6.10. When the mean difference between the component emissivities decreases from 0.07 to 0.035, the RMSE of the retrieved component temperatures for the developed TUM method and that for the TRUST method increase by about 2.2 K and 0.8 K respectively, and the RMSEs of the retrieved component abundances for both methods increase by about 4.5%. Both the performances of the two TUM methods degrade significantly when the difference between component emissivities decreases gradually.

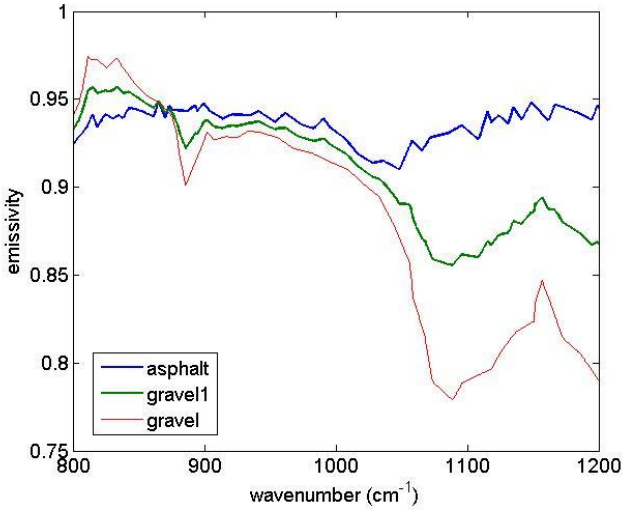

Figure 7.9 Emissivity spectrums used for analyzing the sensitivity of the developed TUM method to the difference between component emissivities

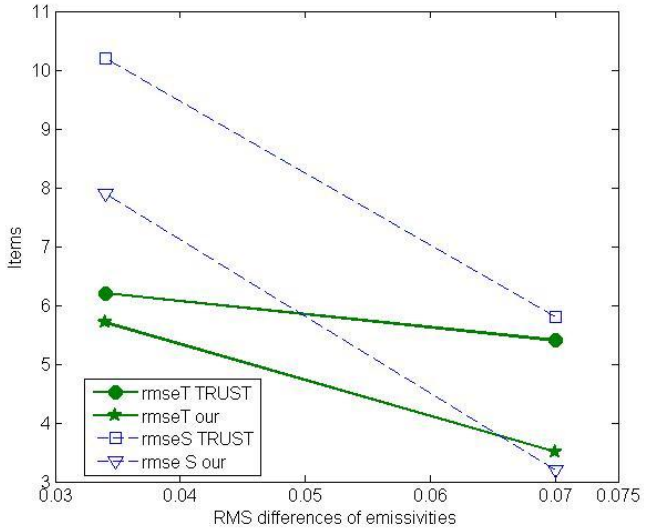

Figure 7.10 Variation of the performances of the developed TUM method and the TRUST method with the difference between component emissivities

7.6 Summary and conclusions

In this chapter, a physics-based TUM method was developed to simultaneously retrieve component temperatures and component abundances from hyperspectral TIR data over heterogeneous surfaces with large variation of component temperatures by using a nonlinearly solution of the radiative transfer equations and a minimization of the reconstruction error of the mixed-surface BOA radiance. The accuracy and the sensitivity of this developed TUM

method were also evaluated by comparing the results with that retrieved by the TRUST method using a flat surface scene simulation data. The conclusions we drew from this study are as follow:

When the standard deviation of component temperatures is 6 K, component temperatures retrieved by the developed TUM method from simulated hypersperspectral TIR data is more accurate than those retrieved by the TRUST method with a RMSE of 3 K.

When the difference between the component temperatures decreases from 15 K to 5 K and the standard deviation of component temperatures is set to 3 K, the component temperatures retrieved by the developed TUM method have an error growing from 1.9 K to 2.1 K and those retrieved by the TRUST method have an error growing from 1.7 K to 2.1 K. Both the methods are not sensitive to the difference between the component temperatures.

When standard deviation of component temperatures growing from 3 K to 9 K, the RMSE of the component temperatures retrieved by the developed TUM method increases by 1.8 K and that retrieved by the TRUST method increase by 4.6 K. The developed TUM method is less sensitive to the standard deviation of component temperatures than the TRUST method.

When the difference between the component emissivities decreases from 0.07 to 0.035, the component temperatures retrieved by the developed TUM method from the simulation data have an error increasing from 3.5 K to 5.7 K while those retrieved by the TRUST method have an error increasing from 5.5 K to 6.3 K. And the component abundances retrieved by each method from the simulation data have an error increasing by 4.5%. Both the methods are sensitive to the difference between component emissivities.

The shortcomings of the developed TUM method include: it requires images in the reflective domain to identify pure pixels; it requires that each mixed pixel contains only two components; it is not validated using satellite data; due to the high relativity among hyperspectral TIR channels which causes that the solution of radiative transfer equations not stable, the component temperature retrieved by the developed TUM method was not improved significantly. Extra constraints are required to stabilize the solution of rediative transfer equaitons to retrieve component temperatures from TIR data. In the future, we will validate the developed TUM method using satellite data and evaluate the accuracy of the developed TUM method for mixed pixels containing more than two components.

8 Conclusions and perspectives

LST is an important parameter in climate systems. LST can be retrieved by various methods from multispectral TIR data and hyperspectral TIR data. Hyperspectral TIR data with high spectral resolution contains large spectral information about the atmosphere and land surfaces, provide new way to develop methods for retrieving LST from space. Hyperspectral TIR data has damaged data due to failure of the instrument or other damage in the process of data transfer. The LST retrieval methods cannot be used for retrieving LST from hyperspectral TIR data containing damaged data at certain channels. Moreover, the LST retrieval methods retrieve a single LST for a mixed pixel, cannot be used to retrieve component temperatures which are important for various applications. Various temperature unmixing methods exist to retrieve component temperatures from TIR data. However these temperature unmixing methods are not suitable for retrieving component temperatures for heterogeneous surfaces with large variation of component temperatures from hyperspectral high spatial resolution TIR data. The objectives of the thesis includes:(1) to develop a method for retrieving LST from hyperspectral TIR data contain damaged data at certain channels; (2) to develop a TUM method for retrieving component temperatures for heterogeneous surfaces with large variation of component temperature from hyperspectral high spatial resolution TIR data.

To fulfill these objectives, this study firstly developed a multi-channel method for retrieving LST for high emissivity surfaces from hyperspectral TIR data by using stepwise regression method. The accuracy and sensitivity of the developed multi-channel method for high emissivity surfaces were analyzed using simulation data and Metop-A/IASI data. Then, the developed multi-channel method was adapted for retrieving LST for natural land surfaces by taking LSE into consideration. The sensitivities of the adapted multi-channel method to LSE and instrumental noise were analyzed with simulation data. Finally, a physics-based TUM method is developed by nonlinearly solving the radiative transfer equations and by a minimization of construction error of the mixed-surface BOA radiance with the first-guess values for component parameters. The sensitivities of the developed TUM method to the standard deviation of component temperatures, to the difference between the component temperatures, and to the difference between component emissivities, and the accuracy of component temperatures retrieved by the developed TUM method was analyzed using simulation data at nadir.

8.1 Conclusions

We firstly proposed a multi-channel LST retrieval method for hyperspectral TIR data by assuming LSE is unity. The accuracy of the developed multi-channel method is analyzed by comparing input LSTs and the retrieved LSTs using simulation data and by comparing LSTs retrieved by this method from Metop-A/IASI data and the SST product from Metop-A/AVHRR over Mediterranean Sea area. The sensitivities of the developed multi-channel method to instrumental noise and to spectral sampling frequency were analyzed by using simulation data.

The conclusions we drew from this study are as follow:

(1) LST of high emissivity surfaces can be accurately retrieved by the developed multi-channel method from the simulation data using only measurements at 10 channels with RMSE of 0.2 K. The performance of the developed multi-channel method is encouraging.

(2) LST of high emissivity surfaces can be accurately retrieved from satellite data. Taking Metop-A/AVHRR LST product as a reference, the RMSE of the LST retrieved from Metop-A/IASI data is 0.43 K.

(3) The coefficients in the developed multi-channel method are dependent on spectral sampling frequency. LST can be retrieved accurately by the developed multi-channel method for each spectral sampling frequency if the coefficients are refitted.

(4) The impact of instrumental noise on the developed multi-channel method is of the order of the magnitude of the instrumental noise. It is critical that developed multi-channel method is not significantly sensitive to instrumental noise.

Then, we adopted the developed multi-channel method for high emissivity surfaces to natural land surfaces by parameterizing LSE and water vapor content into the linear function used by the multi-channel method for high emissivity surfaces. Validation was carried out by comparing the input LST and the LST retrieved by the adopted multi-channel method over natural land surfaces using simulation data and by comparing LST retrieved by the adopted multi-channel method from the Metop-A/IASI data with the LST product from Metop-A/IASI over Australia. The LSE data and water vapor content data used for applying the adopted multi-channel method to satellite data were that from MODIS MOD11B1 LSE product and that from NOAA ESRL atmospheric profile database. The sensitivities of the adopted multi-channel method to instrumental noise, to LSE and to the error of water vapor content were analyzed using simulation data. The conclusions which we drew from the study in this chapter are listed as follow:

(1) When water vapor content error is 10% and LSE error is neglected, the LST can be retrieved by the adopted multi-channel method from simulated IASI data with a RMSE of 0.6 K using measurements at 10 channels and two channel LSEs. The adopted multi-channel method is promising.

(2) When NEDT increasing by 0.1 K and 0.2 K, the RMSE of LST retrieved from the simulated IASI data increases by 0.15 K and 0.3 K. The impact of instrumental noise on the adopted multichannel method is two times of the magnitude of instrumental noise.

(3) When the mean value of the used channel LSEs decreases from large than 0.95 to less than 0.95, the RMSE of the retrieved LST increases from 0.5 K to 0.8 K. The impact of LSE on the adopted multi-channel method is significant.

(4) With MODIS LSE product and using water vapor content data with an error of 20%, the difference between the LST retrieved by the adopted multi-channel method from the Metop-A IASI data and the LST product from Metop-A/IASI is about 2 K. There are no large difference between the LST retrieved by the adopted multi-channel method and LST product from Metop-A/IASI.

Finally, with LSTs and LSEs over pure pixels retrieved by the TES method and the initial component parameters retrieved by the TRUST method, we developed a physics-based TUM method to simultaneously retrieve component temperature and component emissivity from hyperspectral TIR data for heterogeneous surfaces with large variation of component temperatures by nonlinearly solving the radiative transfer equations and by a minimization of the reconstruction error of the mixed-pixel BOA radiance. The accuracy of the developed TUM method was validated by comparing the retrieved results with those of the TRUST method using simulation data at nadir. The sensitivities of the developed TUM method to the standard deviation of component temperatures, to the difference between component temperatures and to the difference between the component emissivities were analyzed. Main conclusions described in this chapter are listed as follows:

(1) When the error of component emissivities of each material is 0.0005 and standard deviation of component temperatures is 6 K, component temperatures can be retrieved by the developed TUM method from the simulation IASI data with a RMSE of 3 K. Component temperatures retrieved from the simulation data by the developed TUM method is more accurate than those retrieved by the TRUST method.

(2) When the standard deviation of component temperatures grows from 3 K to 9 K, the RMSE of the retrieved component temperatures for the developed TUM method increases by 1.8 K while that for the TRUST method increases by 4.6 K. The developed TUM method is

less sensitive to the standard deviation of component temperatures than the TRUST method.

(3) When the difference between component temperatures decreasing from 15 K to 5 K and the standard deviation of component temperatures is set to 3 K, the RMSE of the retrieved component temperatures for the developed TUM method and that for the TRUST method increase by 0.2 K and 0.4 K, respectively and the RMSE of the retrieved component abundances for each method increases from 1.3% to 1.9%. The two TUM methods are not sensitive to the difference between component temperatures.

(4) When the mean difference between the component emissivities decrease from 0.07 to 0.035, the RMSE of the retrieved component temperatures for the developed TUM method and that for the TRUST method increase by about 2.2 K and 0.8 K respectively, and the RMSEs of the retrieved component abundances for both methods increases by about 4.5%. The performances of both methods degrade significantly when the difference between component emissivities decreases gradually.

8.2 Perspectives

The adopted multi-channel method for retrieving LST for natural land surfaces requires accurate LSE and accurate atmospheric water vapor content which are difficult to obtain. It's needed to develop new methods for atmospheric correction of hyperspectral TIR data.

The adopted multi-channel method for retrieving LST for natural land surfaces is developed for measurements of hyperspectral TIR sensor at nadir in this study. We will extend this multi-channel method to off-nadir measurements in the future.

The developed TUM method requires extra constraint to stabilize the inversion of radiative transfer equations and has not been validated using satellite data yet. In the future, we will validate the developed TUM method using satellite data and develop new TUM method by incorporating new constraint to solve the radiative transfer equations for component temperatures.

The developed TUM method has not been validated over mixed pixels containing more than two components. We will evaluate the performance of the TUM method over complex mixed pixels containing three components in the future.

References

Adams, J.B., Smith, M.O., & Gillespie, A.R. (1989). Simple models for complex natural surfaces: A strategy for the hyperspectral era of remote sensing. In, *12th Canadian Symposium on Remote Sensing Geoscience and Remote Sensing Symposium* (pp. 16-21)

Aires, F., Chedin, A., Scott, N.A., & Rossow, W.B. (2002a). A regularized neural net approach for retrieval of atmospheric and surface temperatures with the IASI instrument. *Journal of Applied Meteorology and Climatology, 41*, 144-159

Aires, F., Rossow, W., Scott, N., & Chédin, A. (2002b). Remote sensing from the infrared atmospheric sounding interferometer instrument 2. Simultaneous retrieval of temperature, water vapor, and ozone atmospheric profiles. *Journal of Geophysical Research: Atmospheres, 107*, ACH 7-1–ACH 7-12

Aires, F., Rossow, W.B., Scott, N.A., & Chedin, A. (2002c). Remote sensing from the infrared atmospheric sounding interferometer instrument - 1. Compression, denoising, and first-guess retrieval algorithms. *Journal of Geophysical Research-Atmospheres, 107*, ACH 6-1–ACH 6-15

Archer, N.A.L., & Jones, H.G. (2006). Integrating hyperspectral imagery at different scales to estimate component surface temperatures. *International Journal of Remote Sensing, 27*, 2141-2159

Atitar, M., & Sobrino, J.A. (2009). A Split-window Algorithm for Estimating LST From Meteosat 9 Data: Test and Comparison With In Situ Data and MODIS LSTs. *IEEE Geoscience and Remote Sensing Letters, 6*, 122-126

Barducci, A., & Pippi, I. (1996). Temperature and emissivity retrieval from remotely sensed images using the "grey body emissivity" method. *IEEE Transactions on Geoscience and Remote Sensing, 34*, 681-695

Barducci, A., Guzzi, D., Marcoionni, P., & Pippi, I. (2004). A new algorithm for temperature and spectral emissivity retrieval over active fires in the TIR spectral range. *IEEE Transactions on Geoscience and Remote Sensing, 42*, 1521-1529

Becker, F., & Li, Z.L. (1990). Towards a local split window method over land surfaces. *International Journal of Remote Sensing, 11*, 369-393

Becker, F., & Li, Z.L. (1995). Surface temperature and emissivity at various scales: Definition, measurement and related problems. *Remote Sensing Reviews, 12*, 225-253

Blackwell, W.J. (2005). A neural-network technique for the retrieval of atmospheric temperature and moisture profiles from high spectral resolution sounding data. *Ieee Transactions on Geoscience and Remote Sensing, 43*, 2535-2546

Bloom, H.J. (2001). The Cross-track Infrared Sounder (CrIS): a sensor for operational

meteorological remote sensing. In, *IEEE 2001 International Geoscience and Remote Sensing Symposium, 2001,* (pp. 1341-1343)

Borel, C.C. (1997). Iterative retrieval of surface emissivity and temperature for a hyperspectral sensor. In: Los Alamos National Lab., NM (United States), https://www.osti.gov/scitech/servlets/purl/548853

Borel, C. (2008). Error analysis for a temperature and emissivity retrieval algorithm for hyperspectral imaging data. *International Journal of Remote Sensing, 29*, 5029-5045

Caselles, V., Coll, C., & Valor, E. (1997). Land surface emissivity and temperature determination in the whole HAPEX-Sahel area from AVHRR data. *International Journal of Remote Sensing, 18*, 1009-1027

Chalon, G., Cayla, F., & Diebel, D. (2001). IASI- An advanced sounder for operational meteorology. In, *IAF, International Astronautical Congress, 52 nd, Toulouse, France*

Chaumat, L., Standfuss, C., Tournier, B., Armante, R., & Scott, N.A. (2009). 4A/OP Reference Documentation: NOV-3049-NT-1178-v4.0 In: NOVELTIS,LMD/CNRS,CNES,http://4aop.noveltis.com/sites/4aop.noveltis.loc/files/NOV-3049-NT-1178v4.3.pdf

Chedin, A., Scott, N.A., & Berroir, A. (1982). A single-channel double-viewing angle method for sea-surface temperature determination from coincident MeteoSat and TIROS-N radiometric measurements. *Journal of Applied Meteorology, 21*, 613-618

Chedin, A., Scott, N.A., Wahiche, C., & Moulinier, P. (1985). The improved initialization inversion method - A high-resolution physical method for temperature retrievals from satellites of the TIROS-N series. *Journal of Applied Meteorology and Climatology, 24*, 128-143

Cheng, J., Liang, S., Wang, J., & Li, X. (2010). A stepwise refining algorithm of temperature and emissivity separation for hyperspectral thermal infrared data. *IEEE Transactions on Geoscience and Remote Sensing, 48*, 1588-1597

Chevallier, F., Cheruy, F., Scott, N., & Chedin, A. (1998). A neural network approach for a fast and accurate computation of a longwave radiative budget. *Journal of Applied Meteorology, 37*, 1385-1397

Chien, S., Silverman, D., Davies, A.G., & Mandl, D. (2009). Onboard Science Processing Concepts for the HyspIRI Mission. *IEEE Intelligent Systems, 24*, 12-19

Coll, C., & Caselles, V. (1997). A split-window algorithm for land surface temperature from advanced very high resolution radiometer data: Validation and algorithm comparison. *Journal of Geophysical Research:Atmospheres, 102*, 16697-16713

Coll, C., Caselles, V., Valor, E., Niclos, R., Sanchez, J.M., Galve, J.M., & Mira, M. (2007). Temperature and emissivity separation from ASTER data for low spectral contrast surfaces. *Remote Sensing of Environment, 110*, 162-175

Collins, E.F., Roberts, D.A., & Borel, C.C. (2001). Spectral mixture analysis of simulated thermal infrared spectrometry data: An initial temperature estimate bounded TESSMA search approach. *IEEE Transactions on Geoscience and Remote Sensing, 39*, 1435-1446

Cubero-Castan, M., Briottet, X., Shimoni, M., Achard, V., & Chanussot, J. (2012). Physic based aggregation model for the unmixing of temperature and optical properties in the infrared domain. In, *2012 4th Workshop on Hyperspectral Image and Signal Processing: Evolution in Remote Sensing (WHISPERS)* (pp. 1-4)

Cubero-Castan, M., Chanussot, J., Achard, V., Briottet, X., & Shimoni, M. (2015). A Physics-Based Unmixing Method to Estimate Subpixel Temperatures on Mixed Pixels. *IEEE Transactions on Geoscience and Remote Sensing, 53*, 1894-1906

Deng, C., & Wu, C. (2013). Examining the impacts of urban biophysical compositions on surface urban heat island: A spectral unmixing and thermal mixing approach. *Remote Sensing of Environment, 131*, 262-274

Dimmeler, A., Schilling, H., Shimoni, M., Bulatov, D., & Middelmann, W. (2013). Combined airborne sensors in urban environment. In, *SPIE Security+ Defence* (pp. 88970U-88970U-88979): International Society for Optics and Photonics

Dozier, J. (1981). A method for satellite identification of surface-temperature fields of subpixel resolution. *Remote Sensing of Environment, 11*, 221-229

Fontanilles, G., Briottet, X., Fabre, S., Lefebvre, S., & Vandenhaute, P.-F. (2010). Aggregation process of optical properties and temperature over heterogeneous surfaces in infrared domain. *Applied Optics, 49*, 4655-4669

Francois, C., Ottle, C., & Prevot, L. (1997). Analytical parameterization of canopy directional emissivity and directional radiance in the thermal infrared. Application on the retrieval of soil and foliage temperatures using two directional measurements. *International Journal of Remote Sensing, 18*, 2587-2621

Galve, J.A., Coll, C., Caselles, V., & Valor, E. (2008). An atmospheric radiosounding database for generating land surface temperature algorithms. *IEEE Transactions on Geoscience and Remote Sensing, 46*, 1547-1557

Garcia-Moreno, F.T., Fargant, G., Guerin, F., Israbian, C., Mathieu, J.-C., Michaud, J., Bardoux, A., Hagolle, O., & Lagouarde, J.-P. (2009). MISTIGRI instrumental concept for high-resolution thermal infrared imaging. In, *SPIE Optical Engineering+ Applications* (pp. 745307-745307-745312): International Society for Optics and Photonics

Gillespie, A., Rokugawa, S., Matsunaga, T., Cothern, J.S., Hook, S., & Kahle, A.B. (1998). A temperature and emissivity separation algorithm for Advanced Spaceborne Thermal Emission and Reflection Radiometer (ASTER) images. *IEEE Transactions on Geoscience and Remote Sensing, 36*, 1113-1126

Gillespie, A.R. (1986). Lithologic mapping of silicate rocks using TIMS. In, *The TIMS Data User's Workshop* (pp. 29-44). Pasadena: Jet Propulsion laboratory

Gillespie, A.R., Abbott, E.A., Gilson, L., Hulley, G., Jimenez-Munoz, J.-C., & Sobrino, J.A. Residual errors in ASTER temperature and emissivity standard products AST08 and AST05. *Remote Sensing of Environment, 115*, 3681-3694

Gillespie, A.R., Abbott, E.A., Gilson, L., Hulley, G., Jimenez-Munoz, J.C., & Sobrino, J.A. (2011). Residual errors in ASTER temperature and emissivity standard products AST08 and AST05. *Remote Sensing of Environment, 115*, 3681-3694

Gillespie, A.R., Rokugawa, S., Hook, S.J., Matsunaga, T., & Kahle, A.B. (1999). Temperature/emissivity separation algorithm theoretical basis document, version 2.4. *NASA/GSFC, Greenbelt, MD*, https://unit.aist.go.jp/igg/rs-rg/ASTERSciWeb_AIST/jp/documnts/pdf/2b0304.pdf

Goldberg, M.D., Qu, Y.N., McMillin, L.M., Wolf, W., Zhou, L.H., & Divakarla, M. (2003). AIRS near-real-time products and algorithms in support of operational numerical weather prediction. *IEEE Transactions on Geoscience and Remote Sensing, 41*, 379-389

Hecker, C., van der Meijde, M., & van der Meer, F.D. (2010). Thermal infrared spectroscopy on feldspars - Successes, limitations and their implications for remote sensing. *Earth-Science Reviews, 103*, 60-70

Hilton, F., Armante, R., August, T., Barnet, C., Bouchard, A., Camy-Peyret, C., Capelle, V., Clarisse, L., Clerbaux, C., Coheur, P.F., Collard, A., Crevoisier, C., Dufour, G., Edwards, D., Faijan, F., Fourrie, N., Gambacorta, A., Goldberg, M., Guidard, V., Hurtmans, D., Illingworth, S., Jacquinet-Husson, N., Kerzenmacher, T., Klaes, D., Lavanant, L., Masiello, G., Matricardi, M., McNally, A., Newman, S., Pavelin, E., Payan, S., Pequignot, E., Peyridieu, S., Phulpin, T., Remedios, J., Schlussel, P., Serio, C., Strow, L., Stubenrauch, C., Taylor, J., Tobin, D., Wolf, W., & Zhou, D. (2012). Hyperspectral Earth observation from IASI: Five years of accomplishments. *Bulletin of the American Meteorological Society, 93*, 347-370

Hook, S.J., Gabell, A.R., Green, A.A., & Kealy, P.S. (1992). A comparison of techniques for extracting emissivity information from thermal infrared data for geologic studies. *Remote Sensing of Environment, 42*, 123-135

Hulley, G.C., & Hook, S.J. (2009a). The North American ASTER Land Surface Emissivity Database (NAALSED) Version 2.0. *Remote Sensing of Environment, 113*, 1967-1975

Hulley, G.C., Hook, S.J., & Baldridge, A.M. (2009b). Validation of the North American ASTER Land Surface Emissivity Database (NAALSED) version 2.0 using pseudo-invariant sand dune sites. *Remote Sensing of Environment, 113*, 2224-2233

Hulley, G.C., & Hook, S.J. (2011). Generating Consistent Land Surface Temperature and Emissivity Products Between ASTER and MODIS Data for Earth Science Research.

IEEE Transactions on Geoscience and Remote Sensing, 49, 1304-1315

Ingram, P.M., & Muse, A.H. (2001). Sensitivity of iterative spectrally smooth temperature/emissivity separation to algorithmic assumptions and measurement noise. *IEEE Transactions on Geoscience and Remote Sensing, 39*, 2158-2167

Jacob, F., Schmugge, T., Olioso, A., French, A., Courault, D., Ogawa, K., Petitcolin, F., Chehbouni, G., Pinheiro, A., & Privette, J. (2008). Modeling and inversion in thermal infrared remote sensing over vegetated land surfaces. *Advances in Land Remote Sensing* (pp. 245-291): Springer

Jia, L., Li, Z.L., Menenti, M., Su, Z., Verhoef, W., & Wan, Z. (2003). A practical algorithm to infer soil and foliage component temperatures from bi-angular ATSR-2 data. *International Journal of Remote Sensing, 24*, 4739-4760

Jiang, G.M., & Li, Z.L. (2008). Split-window algorithm for land surface temperature estimation from MSG1-SEVIRI data. *International Journal of Remote Sensing, 29*, 6067-6074

Jiménez-Muñoz, J.C., & Sobrino, J.A. (2003). A generalized single-channel method for retrieving land surface temperature from remote sensing data. *Journal of Geophysical Research: Atmospheres, 108*, 4688

Jimenez-Munoz, J.C., Cristobal, J., Sobrino, J.A., Soria, G., Ninyerola, M., & Pons, X. (2009). Revision of the Single-Channel Algorithm for Land Surface Temperature Retrieval From Landsat Thermal-Infrared Data. *IEEE Transactions on Geoscience and Remote Sensing, 47*, 339-349

Kanani, K., Poutier, L., Nerry, F., & Stoll, M.-P. (2007). Directional effects consideration to improve out-doors emissivity retrieval in the 3-13 μm domain. *Optics Express, 15*, 12464-12482

Kerr, Y.H., Lagouarde, J.P., & Imbernon, J. (1992). Accurate land surface-temperature retrieval from AVHRR data with use of an improved split window algorithm. *Remote Sensing of Environment, 41*, 197-209

Lawrence, M.G. (2005). The Relationship between relative humidity and the dewpoint temperature in moist air: A simple conversion and applications. *Bulletin of the American Meteorological Society, 86*, 225-233

Le Borgne, P., Legendre, G., & Marsouin, A. (2007). Operational SST retrieval from MetOp/AVHRR. In, *Proc. 2007 EUMETSAT Conf., Amsterdam, the Netherlands*: Citeseer

Le Marshall, J., Jung, J., Derber, J., Chahine, M., Treadon, R., Lord, S.J., Goldberg, M., Wolf, W., Liu, H.C., Joiner, J., Woollen, J., Todling, R., van Delst, P., & Tahara, Y. (2006). Improving global analysis and forecasting with AIRS. *Bulletin of the American Meteorological Society, 87*, 891-894

Li, J., Li, J., Weisz, E., & Zhou, D.K. (2007). Physical retrieval of surface emissivity spectrum from hyperspectral infrared radiances. *Geophysical Research Letters, 34*, L16812

Li, J., Li, Z.L., Jin, X., Schmit, T.J., Zhou, L.H., & Goldberg, M.D. (2011). Land surface emissivity from high temporal resolution geostationary infrared imager radiances: Methodology and simulation studies. *Journal of Geophysical Research:Atmospheres, 116*, D01304

Li, X., Strahler, A.H., & Friedl, M.A. (1999). A conceptual model for effective directional emissivity from nonisothermal surfaces. *IEEE Transactions on Geoscience and Remote Sensing, 37*, 2508-2517

Li, Z.-L., Tang, B.-H., Wu, H., Ren, H., Yan, G., Wan, Z., Trigo, I.F., & Sobrino, J.A. (2013). Satellite-derived land surface temperature: Current status and perspectives. *Remote Sensing of Environment, 131*, 14-37

Ma, X.L., Wan, Z.M., Moeller, C.C., Menzel, W.P., & Gumley, L.E. (2002). Simultaneous retrieval of atmospheric profiles, land-surface temperature, and surface emissivity from Moderate-Resolution Imaging Spectroradiometer thermal infrared data: extension of a two-step physical algorithm. *Applied Optics, 41*, 909-924

Ma, X.L., Wan, Z.M., Moeller, C.C., Menzel, W.P., Gumley, L.E., & Zhang, Y.L. (2000). Retrieval of geophysical parameters from Moderate Resolution Imaging Spectroradiometer thermal infrared data: Evaluation of a two-step physical algorithm. *Applied Optics, 39*, 3537-3550

Mao, K., Shi, J., Tang, H., Li, Z.-L., Wang, X., & Chen, K.-S. (2008). A neural network technique for separating land surface emissivity and temperature from ASTER imagery. *IEEE Transactions on Geoscience and Remote Sensing, 46*, 200-208

Mas, J., & Flores, J. (2008). The application of artificial neural networks to the analysis of remotely sensed data. *International Journal of Remote Sensing, 29*, 617-663

Masiello, G., & Serio, C. (2013). Simultaneous physical retrieval of surface emissivity spectrum and atmospheric parameters from infrared atmospheric sounder interferometer spectral radiances. *Applied Optics, 52*, 2428-2446

Masiello, G., Serio, C., De Feis, I., Amoroso, M., Venafra, S., Trigo, I., & Watts, P. (2013). Kalman filter physical retrieval of surface emissivity and temperature from geostationary infrared radiances. *Atmospheric Measurement Techniques, 6*, 3613-3634

Matsunaga, T. (1994). A temperature-emissivity separation method using an empirical relationship between the mean, the maximum, and the minimum of the thermal infrared emissivity spectrum. *Journal of the Remote Sensing Society of Japan, 14*, 230-241

McCabe, M.F., Balick, L.K., Theiler, J., Gillespie, A.R., & Mushkin, A. (2008). Linear mixing in thermal infrared temperature retrieval. *International Journal of Remote Sensing, 29*,

5047-5061

McMillin, L.M. (1975). Estimation of sea surface temperatures from two infrared window measurements with different absorption. *Journal of Geophysical Research, 80*, 5113-5117

Menenti, M., Jia, L., & Li, Z.-L. (2008). Multi-angular thermal infrared observations of terrestrial vegetation. *Advances in Land Remote Sensing* (pp. 51-93): Springer

Menzel, W.P., Smith, W.L., & Stewart, T.R. (1983). IMPROVED CLOUD MOTION WIND VECTOR AND ALTITUDE ASSIGNMENT USING VAS. *Journal of Climate and Applied Meteorology, 22*, 377-384

Mushkin, A., Balick, L.K., & Gillespie, A.R. (2005). Extending surface temperature and emissivity retrieval to the mid-infrared (3-5 mu m) using the Multispectral Thermal Imager (MTI). *Remote Sensing of Environment, 98*, 141-151

OuYang, X., Wang, N., Wu, H., & Li, Z.-L. (2010). Errors analysis on temperature and emissivity determination from hyperspectral thermal infrared data. *Optics Express, 18*, 544-550

Paul, M., Aires, F., Prigent, C., Trigo, I.F., & Bernardo, F. (2012). An innovative physical scheme to retrieve simultaneously surface temperature and emissivities using high spectral infrared observations from IASI. *Journal of Geophysical Research:Atmospheres, 117*, D11302

Pequignot, E., Chedin, A., & Scott, N.A. (2008). Infrared continental surface emissivity spectra retrieved from AIRS hyperspectral sensor. *Journal of Applied Meteorology and Climatology, 47*, 1619-1633

Prata, A.J. (1993). Land-surface temperatures derived from the advanced very high-resolution radiometer and the along-track scanning radiometer .1. Theory. *Journal of Geophysical Research:Atmospheres, 98*, 16689-16702

Prata, A. (1994). Land surface temperature determination from satellites. Advances in space research, 14, 15-26

Qin, Z., Karnieli, A., & Berliner, P. (2001). A mono-window algorithm for retrieving land surface temperature from Landsat TM data and its application to the Israel-Egypt border region. *International Journal of Remote Sensing, 22*, 3719-3746

Renhorn, I., Achard, V., Axelsson, M., Benoist, K., Borghys, D., Briottet, X., Dekker, R., Dimmeler, A., Friman, O., & Kåsen, I. (2013). Hyperspectral reconnaissance in urban environment. In, *SPIE Defense, Security, and Sensing* (pp. 87040L-87040L-87014): International Society for Optics and Photonics

Rhee, J., Im, J., & Carbone, G.J. (2010). Monitoring agricultural drought for arid and humid regions using multi-sensor remote sensing data. *Remote Sensing of Environment, 114*, 2875-2887

Rodgers, C.D. (1976). Retrieval of atmospheric temperature and composition from remote measurements of thermal radiation. *Reviews of Geophysics, 14*, 609-624

Salisbury, J.W., Wald, A., & D'Aria, D.M. (1994). Thermal-infrared remote sensing and Kirchhoff's law: 1. Laboratory measurements. *Journal of Geophysical Research: Solid Earth, 99*, 11897-11911

Sawabe, Y., Matsunaga, T., Rokugawa, S., & Hoyano, A. (2003). Temperature and emissivity separation for multi-band radiometer and validation ASTER TES algorithm. *Journal of the Remote Sensing Society of Japan (Japan)*

Schaepman, M.E., Ustin, S.L., Plaza, A.J., Painter, T.H., Verrelst, J., & Liang, S. (2009). Earth system science related imaging spectroscopy—An assessment. *Remote Sensing of Environment, 113*, S123-S137

Schlussel, P., & Goldberg, M. (2002). Retrieval of atmospheric temperature and water vapour from IASI measurements in partly cloudy situations. *Advances in Space Research, 29*, 1703-1706

Simeoni, D., Astruc, P., Miras, D., Alis, C., Andreis, O., Scheidel, D., Degrelle, C., Nicol, P., Bailly, B., & Guiard, P. (2004). Design and development of IASI instrument. In, *Optical Science and Technology, the SPIE 49th Annual Meeting* (pp. 208-219): International Society for Optics and Photonics

Smith, W.L., & Frey, R. (1990). On cloud alititude determinations from high-resolution interferometer sounder (HIS) obeservations. *Journal of Applied Meteorology, 29*, 658-662

Sobrino, J.A., Li, Z.L., Stoll, M.P., & Becker, F. (1994). Improvements in the split-window technique for land-surface temperature determination. *IEEE Transactions on Geoscience and Remote Sensing, 32*, 243-253

Sobrino, J.A., Li, Z.L., Stoll, M.P., & Becker, F. (1996). Multi-channel and multi-angle algorithms for estimating sea and land surface temperature with ATSR data. *International Journal of Remote Sensing, 17*, 2089-2114

Sobrino, J., Jiménez-Muñoz, J., El-Kharraz, J., Gómez, M., Romaguera, M., & Soria, G. (2004a). Single-channel and two-channel methods for land surface temperature retrieval from DAIS data and its application to the Barrax site. *International Journal of Remote Sensing, 25*, 215-230

Sobrino, J.A., & Romaguera, M. (2004b). Land surface temperature retrieval from MSG1-SEVIRI data. *Remote Sensing of Environment, 92*, 247-254

Sobrino, J., Sòria, G., & Prata, A. (2004c). Surface temperature retrieval from Along Track Scanning Radiometer 2 data: Algorithms and validation. Journal of Geophysical Research: Atmospheres, 109, D11101

Sobrino, J.A., & Jiménez-Muñoz, J.C. (2005). Land surface temperature retrieval from

thermal infrared data: An assessment in the context of the Surface Processes and Ecosystem Changes Through Response Analysis (SPECTRA) mission. *Journal of Geophysical Research: Atmospheres, 110*, D16103

Sobrino, J.A., Jimenez-Munoz, J.C., Soria, G., Romaguera, M., Guanter, L., Moreno, J., Plaza, A., & Martincz, P. (2008). Land surface emissivity retrieval from different VNIR and TIR sensors. *IEEE Transactions on Geoscience and Remote Sensing, 46*, 316-327

Song, X., & Zhao, Y. (2007). Study on component temperatures inversion using satellite remotely sensed data. *International Journal of Remote Sensing, 28*, 2567-2579

Sun, D.L., & Pinker, R.T. (2003). Estimation of land surface temperature from a Geostationary Operational Environmental Satellite (GOES-8). *Journal Of Geophysical Research-Atmospheres, 108,* 4326

Sun, D., & Pinker, R.T. (2005). Implementation of GOES-based land surface temperature diurnal cycle to AVHRR. *International Journal of Remote Sensing, 26*, 3975-3984

Sun, D., & Pinker, R.T. (2007). Retrieval of surface temperature from the MSG-SEVIRI observations: Part I. Methodology. *International Journal of Remote Sensing, 28*, 5255-5272

Susskind, J., Barnet, C.D., & Blaisdell, J.M. (2003). Retrieval of atmospheric and surface parameters from AIRS/AMSU/HSB data in the presence of clouds. *Ieee Transactions on Geoscience and Remote Sensing, 41*, 390-409

Tang, B.H., Bi, Y.Y., Li, Z.L., & Xia, J. (2008). Generalized Split-Window algorithm for estimate of Land Surface Temperature from Chinese geostationary FengYun meteorological satellite (FY-2C) data. *Sensors, 8*, 933-951

Timmermans, J., Verhoef, W., van der Tol, C., & Su, Z. (2009). Retrieval of canopy component temperatures through Bayesian inversion of directional thermal measurements. *Hydrology and Earth System Sciences, 13*, 1249-1260

Tonooka, H. (2001). An atmospheric correction algorithm for thermal infrared multispectral data over land - A water-vapor scaling method. *IEEE Transactions on Geoscience and Remote Sensing, 39*, 682-692

Valor, E., & Caselles, V. (1996). Mapping land surface emissivity from NDVI: Application to European, African, and South American areas. *Remote Sensing of Environment, 57*, 167-184

Vaughan, R.G., Calvin, W.M., & Taranik, J.V. (2003). SEBASS hyperspectral thermal infrared data: surface emissivity measurement and mineral mapping. *Remote Sensing of Environment, 85*, 48-63

Wan, Z.M., & Dozier, J. (1996). A generalized split-window algorithm for retrieving land-surface temperature from space. *IEEE Transactions on Geoscience and Remote Sensing, 34*, 892-905

Wan, Z., & Li, Z.-L. (1997). A physics-based algorithm for retrieving land-surface emissivity and temperature from EOS/MODIS data. *IEEE Transactions on Geoscience and Remote Sensing, 35*, 980-996

Wan, Z. (1999). MODIS Land-Surface Temperature Algorithm Theoretical Basis Document. In. Greenbelt MD: NASA/GSFC, https://modis.gsfc.nasa.gov/data/atbd/atbd_mod11.pdf

Wan, Z., & Li, Z.L. (2008). Radiance-based validation of the V5 MODIS land-surface temperature product. *International Journal of Remote Sensing, 29*, 5373-5395

Wang, N., Tang, B.-H., Li, C., & Li, Z.-L. (2010). A generalized neural network for simultaneous retrieval of atmospheric profiles and surface temperature from hyperspectral thermal infrared data. In, *IEEE International Geoscience and Remote Sensing Symposium (IGARSS), 2010* (pp. 1055-1058)

Wang, N., Wu, H., Nerry, F., Li, C., & Li, Z.-L. (2011). Temperature and emissivity retrievals from hyperspectral thermal infrared data using linear spectral emissivity constraint. *IEEE Transactions on Geoscience and Remote Sensing, 49*, 1291-1303

Wang, N., Li, Z.-L., Tang, B.-H., Zeng, F., & Li, C. (2013a). Retrieval of atmospheric and land surface parameters from satellite-based thermal infrared hyperspectral data using a neural network technique. *International Journal of Remote Sensing, 34*, 3485-3502

Wang, N., Li, Z.L., Tang, B.H., Zeng, F.N.A., & Li, C.R. (2013b). Retrieval of atmospheric and land surface parameters from satellite-based thermal infrared hyperspectral data using a neural network technique. *International Journal of Remote Sensing, 34*, 3485-3502

Wang, X., OuYang, X., Li, Z.-L., Jiang, X., & Ma, L. (2009). An atmospheric correction method for remotely sensed hyperspectral thermal infrared data. In, *IEEE International Geoscience and Remote Sensing Symposium 2009, Vols 1-5* (pp. 1979-1982)

Watson, K. (1992). Two-temperature method for measuring emissivity. *Remote Sensing of Environment, 42*, 117-121

Weisz, E., Thapliyal, P., Guan, L., Huang, H.-L., Li, J., Borbas, E., & Baggett, K. (2007). International MODIS and AIRS processing package: AIRS products and applications. *Journal of Applied Remote Sensing, 1*, 013519-013519-013523

Zhan, W., Chen, Y., Zhou, J., & Li, J. (2011a). An algorithm for separating soil and vegetation temperatures with sensors featuring a single thermal channel. *IEEE Transactions on Geoscience and Remote Sensing, 49*, 1796-1809

Zhan, W.F., Chen, Y.H., Zhou, J., & Li, J. (2011b). An Algorithm for Separating Soil and Vegetation Temperatures With Sensors Featuring a Single Thermal Channel. *IEEE Transactions on Geoscience and Remote Sensing, 49*, 1796-1809

Zhang, R., Sun, X., Liu, J., Su, H., Tang, X., & Zhu, Z. (2003a). Determination of regional distribution of crop transpiration and soil water use efficiency using quantitative remote

sensing data through inversion. *Science in China Series D-Earth Sciences, 46*, 10-22

ZHANG, R., SUN, X., WAN, W., XU, J., ZHU, Z., & TIAN, J. (2005). An operational two-layer remote sensing model to estimate surface flux in regional scale: Physical background. *Science in China Series D-Earth Sciences, 48*, 225-225

Zhang, R., Tian, J., Su, H., Sun, X., Chen, S., & Xia, J. (2008). Two Improvements of an Operational Two-Layer Model for Terrestrial Surface Heat Flux Retrieval. *Sensors (Basel, Switzerland), 8*, 6165-6187

Zhang, R.H., Sun, X.M., Liu, J.Y., Su, H.B., Tang, X.Z., & Zhu, Z.L. (2003b). Determination of regional distribution of crop transpiration and soil water use efficiency using quantitative remote sensing data through inversion. *Science in China Series D-Earth Sciences*, *46*, 10-22

Zhou, D.K., Smith, W.L., Li, J., Howell, H.B., Cantwell, G.W., Larar, A.M., Knuteson, R.O., Tobin, D.C., Revercomb, H.E., & Mango, S.A. (2002). Thermodynamic product retrieval methodology and validation for NAST-I. *Applied Optics, 41*, 6957-6967

Zhou, D.K., Larar, A.M., Liu, X., Smith, W.L., Strow, L.L., Yang, P., Schluessel, P., & Calbet, X. (2011). Global Land Surface Emissivity Retrieved From Satellite Ultraspectral IR Measurements. *IEEE Transactions on Geoscience and Remote Sensing, 49*, 1277-1290

Zhou, L., Dickinson, R.E., Tian, Y., Jin, M., Ogawa, K., Yu, H., & Schmugge, T. (2003). A sensitivity study of climate and energy balance simulations with use of satellite-derived emissivity data over Northern Africa and the Arabian Peninsula. *Journal of Geophysical Research:Atmospheres, 108*, 4795